



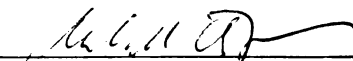


This is to certify that the  
dissertation entitled  
"Giant Dipole Resonance in Highly Excited Lead-208 Nuclei"

presented by  
Easwar Ramakrishnan

has been accepted towards fulfillment  
of the requirements for

Ph.D. degree in Physics

  
Major professor

Date May 2, 1995

**LIBRARY  
Michigan State  
University**

**PLACE IN RETURN BOX to remove this checkout from your record.  
TO AVOID FINES return on or before date due.**

<b>DATE DUE</b>	<b>DATE DUE</b>	<b>DATE DUE</b>
_____	_____	_____
_____	_____	_____
_____	_____	_____
_____	_____	_____
_____	_____	_____
_____	_____	_____
_____	_____	_____

## ABSTRACT

### GIANT DIPOLE RESONANCE IN HIGHLY EXCITED $^{208}\text{Pb}$ NUCLEI

By

Easwar Ramakrishnan

The giant dipole resonance (GDR) built on highly excited states of  $^{208}\text{Pb}$  was measured in order to study the evolution of the resonance with excitation energy. The nucleus was excited by inelastic scattering of 40 MeV/nucleon  $\alpha$  particles. High energy  $\gamma$  rays from the decay of the resonance built on excited states were measured in coincidence with the inelastically scattered projectile nuclei. Target excitation energies in the range of 40 to 110 MeV were chosen by gating on the energy loss of the scattered projectile. Inelastic scattering populates low angular momentum states in the target. The resonance properties were thus measured as a function of excitation energy with very little influence from angular momentum.

The analysis of the measured  $\gamma$ -ray spectra was performed within the standard statistical model. Resonance parameters were extracted by comparing the measured spectra to calculations performed with a modified version of the evaporation code CASCADE.

The width of the resonance was observed to increase systematically with increasing excitation energy from the ground state value of 4 MeV to  $\sim 8$  MeV at the highest measured energy. The measured widths were well reproduced by a model calculation of the resonance cross section that considered the adiabatic coupling of the collective excitation to the free energy surface of the nucleus at finite temperatures.

To my parents

## ACKNOWLEDGEMENTS

First and foremost of all, I would like to thank Michael Thoennessen for his guidance during my stay at the NSCL. I have greatly benefited from the encouragement and inspiration that he provided during the course of this work. His cheerful disposition combined with his willingness to help solve problems at all times made working with him to be a very enjoyable experience.

I thank professors Walter Benenson, Pawel Danielewicz, Carl Bromberg and Gerald Pollack for being on my guidance committee. I am also indebted to Prof. Julius Kovacs and Prof. Subendra Mahanti for their help during my first year of graduate study. I thank my collaborators Jim Beene, Mel Halbert, Robert Varner, Dan Stracener and Paul Mueller from Oak Ridge, and Lee Sobotka, Bob Charity, Demetrios Sarantites and James Dempsey from St. Louis. Erich Ormand deserves a special thanks for providing the theoretical calculations.

The staff at the NSCL were always very friendly and helpful. I wish to especially thank Dave Sanderson, and members of the operations group for their assistance during the experiments.

I greatly enjoyed working with members of our research group, Shigeru Yokoyama, Afshin Azhari, Bob Kryger, Thomas Baumann and Peter Thirolf. Afshin, Shigeru and Thomas made life at the NSCL to be quite an interesting experience. I also had the good fortune of interacting with John 'Ned' Kelley, Stefan Hannuschke, Wen Chen Hsi, Raman Pfaff, Tiina Suomijarvi, Robert Pak, Eugene Gualtieri, Mathias Steiner, Mike Fauerbach, Damian Handzy, Quibauo Pan, Brian Young, Larry Phair, Tong Li, Mike Lisa and many others. Many thanks to 'Ned' for keeping the humour going in our corner of the lab, and to Stefan for putting up with the interruptions in our office.

On a more personal note, I wish to thank my beloved wife Hema for her support and encouragement during the past two years of my student life. My dear friends Ramkumar and Iyer deserve special mention for making my stay in Michigan a memorable one. Prof. A. A. Rangwala, Prof. R. J. Kulkarni, and Dr. H. C. Pradhan of Bombay University were instrumental in my decision to pursue a doctoral degree. Finally, I wish to acknowledge my family and friends back home for their moral support and for helping me face many odds in my pursuit of a higher education.

# Contents

<b>LIST OF TABLES</b>	<b>viii</b>
<b>LIST OF FIGURES</b>	<b>ix</b>
<b>1 Introduction</b>	<b>1</b>
<b>2 Giant Dipole Resonance in Excited Nuclei</b>	<b>6</b>
2.1 Introduction . . . . .	6
2.2 Giant Dipole Resonance . . . . .	6
2.3 GDR Built on Excited States . . . . .	9
2.4 Statistical Modeling . . . . .	10
2.5 Evolution of the Resonance with Excitation . . . . .	12
2.6 Excitation by Inelastic Scattering . . . . .	18
2.6.1 The Inelastic Continuum . . . . .	18
2.6.2 Comparison to Fusion-Evaporation Reactions . . . . .	22
<b>3 Experimental Setup</b>	<b>27</b>
3.1 Introduction . . . . .	27
3.2 Detectors . . . . .	27
3.2.1 BaF <sub>2</sub> Detector Arrays . . . . .	28
3.2.2 Dwarf Ball/Wall CsI Array . . . . .	28
3.3 Electronics . . . . .	30
3.4 Data Acquisition . . . . .	36
<b>4 Data Analysis</b>	<b>37</b>
4.1 Introduction . . . . .	37
4.2 Particle Spectra . . . . .	37
4.2.1 Particle Identification . . . . .	37
4.2.2 Calibration of the DWARF Ball/Wall Array . . . . .	38



4.2.3	Resolution, Efficiency and Response . . . . .	41
4.3	Coincidence $\gamma$ -ray Spectra . . . . .	41
4.3.1	Energy Calibration . . . . .	42
4.3.2	Neutron Separation . . . . .	42
4.3.3	Region Sum for Improved Response . . . . .	43
4.3.4	Resolution, Efficiency and Response . . . . .	46
4.3.5	$\gamma$ -ray Spectra for Different Target Excitations . . . . .	46
4.3.6	Background Subtraction . . . . .	48
4.3.7	Absolute Normalization . . . . .	51
<b>5</b>	<b>Modifications to the Standard CASCADE Code</b>	<b>53</b>
5.1	Level Density Parametrization . . . . .	53
5.2	Input Population for Statistical Calculations . . . . .	62
<b>6</b>	<b>Results and Discussion</b>	<b>67</b>
6.1	Particle Spectra . . . . .	67
6.1.1	Singles $\alpha$ Spectra . . . . .	68
6.1.2	Coincidence $\alpha$ Spectra . . . . .	70
6.1.3	Knockout and Pickup-Decay Contributions . . . . .	74
6.2	Coincidence $\gamma$ -ray Spectra . . . . .	81
6.2.1	$\gamma$ -ray Spectra as a Function of Target Excitation . . . . .	81
6.2.2	Statistical Model Calculations with CASCADE . . . . .	83
6.3	Resonance Width . . . . .	98
6.4	Pre-equilibrium Emission . . . . .	104
<b>7</b>	<b>Summary and Conclusions</b>	<b>113</b>
	<b>LIST OF REFERENCES</b>	<b>116</b>

# List of Tables

6.1	DWARF WALL array angles . . . . .	67
6.2	DWARF BALL array angles . . . . .	68
6.3	Contribution to the $\gamma$ -ray spectrum from individual decay channels .	87
6.4	GDR parameters . . . . .	94
6.5	Calculation of nuclear temperature . . . . .	96

# List of Figures

2.1	Damping of the giant dipole resonance . . . . .	15
2.2	Free energy surfaces for <i>Pb</i> isotopes. . . . .	19
2.3	Angular momentum imparted to target in fusion reactions and inelastic scattering . . . . .	24
2.4	Comparison of angular momenta in the excitation plane . . . . .	25
3.1	Schematic diagram of the BaF <sub>2</sub> packs in the setup . . . . .	29
3.2	The DWARF WALL array as seen by the beam . . . . .	31
3.3	Block diagram of BaF <sub>2</sub> electronics . . . . .	32
4.1	Geometric transformation for particle identification in DWARF detectors	39
4.2	Particle identification plot from a DWARF WALL detector . . . . .	40
4.3	Energy versus time of flight plot from a forward angle BaF <sub>2</sub> detectors	44
4.4	Resolution of time of flight measurement in BaF <sub>2</sub> detectors . . . . .	45
4.5	Response of a BaF <sub>2</sub> detector to 15.11 MeV $\gamma$ rays . . . . .	47
4.6	Extraction of $\gamma$ -ray spectra for different target excitation energies . .	49
4.7	Comparison of $\gamma$ -ray contributions from real and random time gates .	50
4.8	Contribution from nuclear bremsstrahlung at high $\gamma$ -ray energies . . .	52
5.1	Level density parametrization employed in standard CASCADE code	55
5.2	Level density surface calculated using standard CASCADE code . . .	57
5.3	<i>da</i> parameter calculated using Residorf parametrization . . . . .	60
5.4	Level density surface calculated using Reisdorf parametrization . . . .	61
5.5	Obtaining input population for statistical calculations . . . . .	63
5.6	Calculation of angular momentum transfer . . . . .	64
5.7	Angular momentum transferred to target as a function of excitation energy . . . . .	65
5.8	Initial population of nuclei in neutron decay channels . . . . .	66
6.1	Singles $\alpha$ spectra from the WALL array . . . . .	69

6.2	Differential cross section data for elastic $\alpha$ scattering . . . . .	71
6.3	Absolute cross section for inelastic $\alpha$ scattering . . . . .	72
6.4	Coincidence $\alpha$ spectra from the WALL array . . . . .	73
6.5	Neutron emission probability compared to particle coincidence spectrum	75
6.6	$\alpha$ -proton coincidence events in the DWARF array . . . . .	77
6.7	Kinematics of free proton knockout events seen in the DWARF array	78
6.8	Pickup-decay and knockout contributions to the singles $\alpha$ spectrum .	80
6.9	Comparison of $\gamma$ -ray spectra from different detection angles . . . . .	82
6.10	Comparison of $\gamma$ -ray spectra from two different target excitation energy ranges . . . . .	84
6.11	Coincidence $\gamma$ -ray spectra for various target excitation energies . . . .	85
6.12	Contributions to the $\gamma$ -ray spectra from different decay channels . . .	86
6.13	Contributions to the calculated $\gamma$ -ray spectra from individual neutron channels . . . . .	88
6.14	Contributions to the $\gamma$ -ray spectrum from statistical and non-statistical processes . . . . .	90
6.15	Comparison of $\gamma$ -ray spectra and model calculations . . . . .	91
6.16	Comparison of $\gamma$ -ray spectra and calculations on a linear scale . . . .	93
6.17	Resonance width as a function of excitation energy . . . . .	95
6.18	Resonance width as a function of temperature . . . . .	97
6.19	Comparison of measured resonance width to adiabatic coupling calcu- lation . . . . .	101
6.20	Comparison of measured resonance width to collisional dynamics cal- culations . . . . .	103
6.21	Singles $\alpha$ spectra at low $\alpha$ energies . . . . .	105
6.22	Comparison of $\alpha$ singles spectrum with calculated $\alpha$ evaporation spec- trum . . . . .	106
6.23	$\alpha$ spectra in the BALL array . . . . .	108
6.24	High energy background in $\gamma$ -ray spectra compared to particle singles.	109
6.25	$\gamma$ -ray spectra in coincidence with low energy $\alpha$ particles . . . . .	110
6.26	Resonance width at large projectile energy losses . . . . .	112

# Chapter 1

## Introduction

The giant dipole resonance (GDR) is a collective excitation of the nucleus. In the macroscopic picture the resonance is described as a vibration of all protons versus all neutrons within the nucleus. The GDR built on the nuclear ground state has been studied over a wide mass range by means of cross section measurements employing  $(\gamma, n)$  reactions [Die88]. The measured resonance energies exhibit a dependence on the nuclear mass described empirically by the relation  $E_{GDR} = 77 \times A^{-1/3}$ . Since the nuclear radius is related to the mass number by  $R \propto A^{1/3}$ , the resonance energy scales as the inverse of the nuclear radius. The GDR thus couples strongly to the nuclear shape and is therefore sensitive to changes in the shape induced by excitation.

The existence of giant dipole resonance built on excited states of the nucleus was proposed in 1955 by David Brink [Bri55]. The first evidence for excited state GDR was observed in  $(p, \gamma)$  scattering studies performed on light nuclei [Sin65]. Excited state GDR was subsequently observed in heavy nuclei formed by fusion-evaporation reactions [New81]. Fusion reactions populate compound nuclei with high excitation energies and angular momenta. The GDR built on the excited states is measured by detecting the high energy  $\gamma$  rays that emerge from the decay of the resonance. These  $\gamma$  rays are emitted in competition with particle and fission modes of decay. The  $\gamma$  rays are emitted during the early stages of the decay and are therefore sensitive to the

nuclear properties of the excited states on which the resonance is built. Giant dipole resonance spectroscopy thus provides the means for the study of nuclear shapes at high excitation energies and angular momenta. This is an area of high current interest in nuclear structure physics.

Excited state GDR has been studied in nuclei over a wide mass range using fusion evaporation reactions [Sno86, Gar92]. In the  $A < 170$  mass range, the most systematic study of excited state GDR has been performed in *Sn* isotopes [Cha87, Gar86]. Excitation energies ranging up to 600 MeV have been studied, thus probing the limiting temperatures for the existence of the nucleus as an ensemble [Gar87, Suo94].

In deformed nuclei the GDR energy splits into two components corresponding to nuclear radii parallel and perpendicular to the principal symmetry axis. Measurement of the two energy components and the angular distribution of the emitted  $\gamma$  rays provides information on the extent and shape of the deformation. For instance, high energy  $\gamma$ -ray measurements in excited *Er* isotopes revealed prolate nuclear shapes similar to the ground state shapes at temperatures of  $\sim 1$  MeV and a spin range of  $0-25 \hbar$  [Gos85]. The study of excited state GDR was extended to heavier masses in the measurement of deformation in Pb isotopes [But90]. Large prolate deformations ( $\beta \sim 0.43$ ) that persisted to high excitation energies were observed in  $^{200}\text{Pb}$  nuclei.

Since the high energy  $\gamma$  rays are emitted from the early stages of formation of the excited nucleus, GDR spectroscopy provides information on the time scales involved in the de-excitation process. In the Thorium mass range, high energy  $\gamma$ -ray measurements have been performed to determine the time scale of the fission process in excited nuclei [Tho87, Pau94]. The high energy  $\gamma$ -ray spectrum from nuclei undergoing fission has contributions from the compound nuclear system and from the excited fission fragments. Since the dipole resonance energy in the fission fragments is well separated from the resonance energy in the compound system, it is possible to

analyse the  $\gamma$ -ray spectra in terms of pre- and post-fission contributions. The analysis revealed a strong hindrance in the fission process at high excitation energies.

The GDR as a clock has also been applied to the study of reaction dynamics in fusion-evaporation reactions forming *Yb* and *Sn* isotopes [Tho93, Tho94]. High energy  $\gamma$  rays from  $^{164}\text{Yb}$  nuclei formed by fusion reactions exhibited a dependence on the entrance channel. The spectra from an asymmetric entrance channels could be described within the standard statistical model whereas the spectra from a more symmetric entrance channel could not be described. This behaviour was observed earlier in the measurement of neutron multiplicities [Jan86, Ruc86]. The discrepancy in the  $\gamma$ -ray spectra have been explained in terms of a long formation time in the more symmetric fusion channel. Particle and  $\gamma$ -ray emission during the formation time lead to a different compound nuclear population in the symmetric entrance channel compared to the asymmetric channel, thus leading to differences in the measured  $\gamma$ -ray spectra. The  $\gamma$ -ray spectra could be described within the statistical model by treating the emission from the formation stage and from the compound nuclear stage separately.

Measurements of excited state GDR have thus provided valuable information on the properties and dynamics of nuclei at high temperatures. The measurements discussed so far have all been performed on compound nuclei populated in fusion evaporation reactions. Fusion reactions populate compound nuclei over a wide range of angular momenta due to large momentum transfers in the entrance channel. It is thus not possible to study the evolution of the nuclear shape as a function of excitation energy alone decoupled from spin effects. Theoretical understanding of the nuclear surface requires the possibility of experimentally studying nuclei populated in narrow cells of excitation energy and angular momenta [Gar92]. Furthermore, fusion reactions produce compound nuclei that are neutron deficient. It is therefore not

possible to apply fusion reactions to study shape changes in stable nuclei with a view to compare the properties with known ground state systematics.

An alternative to fusion reactions is to excite the nucleus by means of inelastic scattering with hadronic probes. Inelastic scattering has been an important tool in the study of structural properties of nuclei. For moderate projectile energy losses up to  $\sim 30$  MeV, structures observed in the inelastic particle spectra have been well understood in heavy nuclei in terms of giant resonance excitations of various multipolarities built on the nuclear ground state. For instance, inelastic excitation has provided information on the strength function of the giant monopole resonance in nuclei that leads to the estimation of nuclear compressibility [You76, Shl94]. Recently, particle and  $\gamma$ -ray measurements in coincidence with the scattered projectiles have been employed in the study of the decay properties of collective excitations in heavy nuclei [Wou88, Fra88, Bee89].

Recent measurements of heavy ion inelastic scattering have revealed structures in the inelastic continuum that have been interpreted in terms of multiphonon excitations [Fra88, Bee94]. The double dipole excitation of  $GDR \times GDR$  in  $^{208}\text{Pb}$  for instance occurs at an excitation energy of  $\sim 27$  MeV. The study of multiphonon excitations provides a unique way of understanding properties of collective states in nuclei. Precise measurements of the multiphonon energy states can lead to the estimation of anharmonicities in giant resonance excitations.

Beyond the collective excitations built on the nuclear ground state and the multiphonon excitations, the high energy continuum observed in inelastic scattering is not well understood [Tsa75]. The inelastic scattering process does not transfer high angular momenta to the target. Thus if the high energy continuum in the particle spectrum does correspond to high target excitation states, inelastic scattering provides the exciting possibility of studying the evolution of nuclear shapes as a function



of excitation energy with little influence from angular momentum. The giant dipole resonance built on the excited states could be studied by measuring high energy  $\gamma$  rays in coincidence with the scattered projectile.

In the present measurement, the GDR built on excited states of  $^{208}\text{Pb}$  are studied by exciting the nucleus with inelastic  $\alpha$  scattering.  $^{208}\text{Pb}$  has a doubly closed shell structure in the ground state and therefore exhibits a deep minimum in the potential. This minimum broadens rather rapidly beyond nuclear temperatures of  $\sim 1$  MeV due to the vanishing of shell effects. The GDR couples to the potential landscape and the resonance width increases with temperature, reflecting the broadening of the potential surface.

On the theoretical front, the evolution of the resonance with nuclear excitation has been described by different models. Adiabatic models that consider shape fluctuations in the nuclear surface to be a slow process compared to the damping of the GDR, argue that the measured resonance width is a superposition of the widths arising from the coupling of the resonance to all possible shape degrees of freedom [Bro92]. Dissipative models on the other hand treat the damping of the resonance in terms of two-body collisional dynamics that depend only on the nuclear temperature [Sme91]. These model calculations are in agreement with resonance width measurements from fusion reactions. The inelastic excitation process populates low angular momentum states. Thus the validity of these models at high excitation energies and low spins can be studied.

# Chapter 2

## Giant Dipole Resonance in Excited Nuclei

### 2.1 Introduction

The GDR built on highly excited states of the nucleus is studied by measuring the high energy  $\gamma$ -rays from the decay of the resonance. In the following sections the properties of GDR built on the ground state and excited states of the nucleus are discussed. The statistical model employed to analyse the data is reviewed. The process of target excitation by inelastic scattering is discussed and is compared with fusion-evaporation reactions.

### 2.2 Giant Dipole Resonance

The giant dipole resonance (GDR) is a collective mode of excitation of the nucleus. In a macroscopic picture, the GDR has been described by two different models. The Steinweld-Jensen (SJ) model describes the GDR as a dipole oscillation of the proton fluid against the neutron fluid inside a rigid spherical shell [Ste50]. The restoring force for the oscillation is the symmetry energy of the nucleus which is proportional to the term  $(N - Z)^2/A$ . This model yields an expression for the resonance energy

as a function of the mass number  $A$  given by

$$E_{GDR} \propto R^{-1} \propto A^{-1/3}. \quad (2.1)$$

Here the nuclear radius is related to the mass number by  $R = r_0 A^{1/3}$ , where  $r_0 = 1.2 \text{ fm}$ .

The second macroscopic model by Goldhaber and Teller (GT) describes the GDR as an oscillation of rigid interpenetrating neutron and proton spheres [Gol48]. The restoring force in this description arises from the surface symmetry energy. The mass dependence of this surface resonance is given by

$$E_{GDR} \propto \sqrt{\frac{R^2}{A}} \propto A^{-1/6}. \quad (2.2)$$

These two descriptions have been combined by Myers *et al.* in their droplet model [Mye77]. The resonance energy in the Myers model is given by

$$E_{GDR} = (1.13 \times 10^{-4} A^{2/3} + 7.34 \times 10^{-4} A^{1/3})^{-1/2}. \quad (2.3)$$

The ratio of the contributions from the GT mode to the SJ mode in this model is

$$\frac{GT}{SJ} = 6.49 \times A^{-1/3} \quad (2.4)$$

Thus the contribution from the SJ mode becomes more significant at heavier masses. The Myers description is in good agreement with the experimentally observed values of the resonance energy over a wide range of nuclear masses.

In the microscopic picture of the nucleus the GDR can be described as a superposition of one particle-one hole (1p-1h) configurations. This superposition is referred to as a collective particle-hole doorway resonance. The term doorway emphasizes the point that the excited nucleus passes from the entrance channel through the doorway state before the full complexity of the compound nuclear states could be generated

[Fes92]. The energy for this 1p-1h excitation in the independent-particle shell model should correspond to the relative spacing of the major shells which is  $1\hbar\omega = 41A^{-1/3}$ , since the E1 matrix elements for single particle excitation from one major shell to the next one are very strong. Repulsive interaction between the particle and hole states shifts this energy to the observed value of  $\sim 2\hbar\omega$  [Sno86]. The p-h doorway resonance mixes with other complicated configurations like the 2p-2h excitation, and these admixtures contribute spreading width to the resonance.

The GDR built on the ground state of stable nuclei have been extensively studied and documented [Die88]. The first observation of the ground state GDR was from photonuclear cross section measurements. The photo absorption cross section of the GDR may be expressed as a Lorentzian

$$\sigma_{abs}(E_\gamma) = \frac{4\pi e^2 \hbar}{Mc} \frac{NZ}{A} \frac{1}{\Gamma} \frac{E_\gamma^2 \Gamma^2}{(E_\gamma^2 - E_{GDR}^2)^2 + E_\gamma^2 \Gamma^2} \quad (2.5)$$

where  $E_{GDR}$  is the resonance energy,  $\Gamma$  is the resonance width and  $M$  is the nucleon mass.

Integrating the above expression over all  $E_\gamma$  yields for the total  $\gamma$  absorption cross section [Jac75]

$$\sigma_T = \int_0^\infty \sigma_{abs}(E_\gamma) dE_\gamma = \frac{2\pi^2 e^2 \hbar}{Mc} \frac{NZ}{A} = 60 \frac{NZ}{A} \text{ ( MeV mb)}. \quad (2.6)$$

This expression corresponds to a classical E1 sum rule, referred to as the Thomas-Reich-Kuhn sum rule.

As was described earlier the resonance energy  $E_{GDR}$  depends on the mass number of the nucleus. Typical values range from  $\sim 24$  MeV in  $^{16}\text{O}$  to  $\sim 14$  MeV in  $^{208}\text{Pb}$ . The resonance width  $\Gamma$  varies from  $\sim 4$  to 8 MeV. The most narrow widths have been observed in magic nuclei.

Since the resonance energy depends on the nuclear radius through the mass number  $A$ , a single component Lorentzian is appropriate only for spherical nuclei. In

deformed nuclei the GDR energy splits into different energy components along the principal axes of the nucleus.

The nuclear deformation can be expressed in terms of the mean radius  $R_0$  and the deformation parameters  $\beta$  and  $\gamma$  [Boh75]. The deviation in the nuclear radius along the three principal axes is given by

$$\delta R_\kappa = \sqrt{\frac{5}{4\pi}} \beta R_0 \cos\left(\gamma - \kappa \frac{2\pi}{3}\right) \quad (2.7)$$

where  $\kappa=1,2,3$  is the axial index. If the deformation is axially symmetric, there will be one principal axis  $R_{\parallel}$ , and two degenerate axes  $R_{\perp}$  parallel and perpendicular to the principal axis respectively. These axes are related to the deformation parameter  $\beta$  and the mean radius  $R_0$  by

$$R_{\parallel} = R_0 \left(1 + \sqrt{\frac{5}{4\pi}} \beta\right) \quad (2.8)$$

and

$$R_{\perp} = R_0 \left(1 - \frac{1}{2} \sqrt{\frac{5}{4\pi}} \beta\right). \quad (2.9)$$

## 2.3 GDR Built on Excited States

The existence of the GDR built on excited states of the nucleus was postulated as early as in 1955 by David Brink [Bri55]. Brink proposed that the energy dependence of the photo absorption cross section should be independent of the detailed structure of the initial state of the nucleus. Thus the lorentzian form of equation 2.5 should describe the correct photon energy dependence for all initial states. This weak-coupling hypothesis is referred to as the Brink hypothesis.

The evidence for the existence of the GDR built on excited states was first seen in detailed  $(p,\gamma)$  studies in light nuclei [Sin65] where GDR peaks displaced upward

in excitation energy were observed. The energy shift corresponded to the energy of low lying discrete states in the nucleus. The resonance energy for the GDR built on the excited states was thus the same as that for the GDR built on the ground state.

Due to the weak coupling hypothesis, in excited medium and heavy nuclei formed in nuclear reactions, one should observe an enhancement in the multiplicity of high energy  $\gamma$ -rays from the decay of the nucleus at an energy of  $E_\gamma = E_{GDR}$ . This enhancement was first observed in the study of  $\gamma$ -rays from the spontaneous decay of  $^{252}\text{Cf}$  [Die74] and later on in the high-energy  $\gamma$ -ray spectra from the decay of excited nuclei formed in heavy-ion fusion reactions [New81]. Since then the evolution of the GDR as a function of nuclear excitation and spin has been studied in nuclei over a wide mass range [Sno86, Gar92].

## 2.4 Statistical Modeling

The decay of the excited nucleus can be described by the statistical model with the fundamental assumption that all nuclear degrees of freedom are equilibrated prior to the decay [Sto85]. The channels for the decay of an excited nucleus are particle emission,  $\gamma$ -ray emission and fission. The emission of high-energy  $\gamma$ -rays from the decay of the GDR occurs in direct competition with the particle evaporation and fission channels. The branching ratio for  $\gamma$ -ray emission compared to particle emission at the GDR energy  $E_{GDR}$  is  $\approx 10^{-4}$  to  $10^{-5}$ .

In the analysis of the data, the statistical model calculations were performed with the evaporation code CASCADE [Pul77]. The main aspects of the statistical model are described below.

The decay of an excited equilibrated compound nucleus is independent of its formation. Thus, using the principle of detailed balance, the decay can be calculated

using absorption cross sections for the different channels.

For a nucleus with an initial excitation energy and spin  $(E_i, I_i)$ , the particle decay rate to the nucleus with final state  $(E_f, I_f)$  is given by

$$R_p dE_p = \frac{1}{2\pi\hbar} \frac{\rho_f(E_f, I_f)}{\rho_i(E_i, I_i)} T(E_p) dE_p, \quad (2.10)$$

where  $\rho_i$  and  $\rho_f$  are the level densities of the initial and final nuclei and  $T(E_p)$  is the transmission coefficient for the emitted particle. The transmission coefficient is obtained by summing over all possible angular momentum values that are consistent with the initial and final angular momenta of  $I_i$  and  $I_f$ .

The  $\gamma$  decay rate can be calculated in analogy to the particle decay rate. Applying Brink's hypothesis that every nuclear level has a GDR built on it, the width for E1  $\gamma$  decay from an initial state  $(E_i, I_i)$  to the final state  $(E_f, I_f)$  in the same nucleus is given by

$$\Gamma^\gamma(E_\gamma) = \frac{\rho(E_f, I_f)}{\rho(E_i, I_i)} \frac{\sigma_{abs}}{3} \frac{E_\gamma^2}{(\pi\hbar c)^2} dE_\gamma. \quad (2.11)$$

For a spherical nuclear shape, the  $\gamma$  absorption cross section can be substituted from equation 2.5. The  $\gamma$  decay rate is then given by

$$R_\gamma dE_\gamma = \frac{\Gamma^\gamma}{\hbar} = \frac{\rho(E_f, I_f)}{\rho(E_i, I_i)} \frac{1}{2\pi\hbar} f_{GDR}(E_\gamma) E_\gamma^3 dE_\gamma, \quad (2.12)$$

where

$$f_{GDR}(E_\gamma) = \frac{8e^2}{3\hbar M c^3} S_{GDR} \frac{NZ}{A} \frac{E_\gamma \Gamma}{(E_{GDR}^2 - E_\gamma^2)^2 + E_\gamma^2 \Gamma^2} \quad (2.13)$$

is the GDR strength function. The quantity  $S_{GDR}$  is the strength in terms of the classical E1 sum rule. Fusion reaction studies show that the GDR strength exhausts the energy weighted sum rule, corresponding to a value of  $S_{GDR} = 1$ . Equation 2.12 was derived only for E1 radiation and higher multiplicities such as the giant quadrupole resonance have not been considered. The strength function for other multiplicities could be included in the expression for  $\gamma$  decay width [Cha87]. Nevertheless, in the

energy range of interest, the quadrupole radiation strength in nuclei is a few orders of magnitude lower than the dipole strength, and has not been observed [Cha87].

The fission decay rate for the nucleus, derived using the liquid drop model [Boh39], is

$$R_{fss} = \frac{1}{2\pi\hbar\rho(E_i, I_i)} \int_0^{E_i - E_B(I_i)} \rho(E_i - E_B(I_i) - E_{kin}(I_i)) dE_{kin} \quad (2.14)$$

where  $E_{kin}$  is the kinetic energy of the nucleus at the saddle point and  $E_B(I_i)$  is defined as the sum of the angular momentum dependent fission barrier  $E_{FB}$  and the rotational energy. For the decay of excited  $^{208}\text{Pb}$  considered here, there is no appreciable contribution to the decay cross section from the fission process.

The level density  $\rho(E, I)$  of the nucleus is an important input to the statistical model calculation. A consistent level density description over the whole range of excitation energies and spin involved in the decay is necessary. This issue is addressed in detail in chapter 5.

## 2.5 Evolution of the Resonance with Excitation

The properties of nuclei at high excitation energy and spin have been studied by measurements of high energy  $\gamma$ -rays from the decay of the GDR built on these excited states. The time scale for the damping of the resonance is short enough for the  $\gamma$ -ray emission to compete with the other decay modes of the nucleus. The resonance shape of the GDR exhibits a well localized strength in the otherwise exponential continuum of  $\gamma$ -rays from the decay of the nucleus. Furthermore, the  $\gamma$  rays from the decay emerge unhindered by the surrounding nuclear medium. High energy  $\gamma$ -ray measurement thus provides a clean probe for the study of GDR built on excited states. Since the GDR couples strongly with other degrees of freedom such as the nuclear shape, the evolution of the GDR in the nucleus offers information about



nuclear properties at finite temperatures and angular momenta.

So far, the properties of the GDR in excited nuclei have been studied over a wide mass range by fusion reactions [Sno86, Gar92]. The most comprehensive measurements have been performed in  $Sn$  isotopes in the mass range of  $\sim 110$  [Gar86, Cha87, Gar87, Bra89].

The parameters that characterize the resonance are the resonance energy  $E_{GDR}$ , the resonance width  $\Gamma$  and the fraction  $S_{GDR}$  of the E1 sum rule strength. These quantities are extracted by treating them as free parameters in the statistical model calculation performed to fit the  $\gamma$ -ray spectra.

The resonance energy  $E_{GDR}$  extracted from excited nuclei over a wide mass range exhibits no appreciable deviation from the systematics of the corresponding ground state GDR. This implies that the main physical quantities responsible for the resonance, namely the symmetry energy and the volume energy, do not change appreciably with nuclear excitation.

For the GDR built on the ground state of nuclei, the resonance is seen to exhaust the full sum rule strength predicted by the classical Thomas-Reich-Kuhn equation. Fusion-evaporation measurements of the GDR built on excited states show that the sum rule strength is still fully exhausted for excitation energies up to  $\sim 100 - 200$  MeV. Early on it was expected that the study of GDR could lead to the determination of a limiting temperature for the existence of the nuclear ensemble. However, fusion measurements in the  $Sn$  region for excitation energies above  $\sim 300$  MeV have observed a saturation of the GDR strength [Bra89, Gar87]. These measurements suggest a limiting temperature for the existence of the GDR of  $T \approx 4.5$  MeV, which is lower than the limiting temperature of  $\sim 10$  MeV for the existence of the nucleus. Collective excitation is thus expected to disappear before the nucleus as an ensemble ceases to

exist.

Fusion measurements in excited nuclei exhibit a strong increase in the GDR width  $\Gamma$  with increasing excitation energy. For instance in  $Sn$  isotopes the width increases from the ground state value of  $\Gamma=5$  MeV to  $\sim 12$  MeV at an excitation energy of around 150 MeV. At excitation energies beyond  $\sim 200$  MeV, measurements exhibit a saturation of the resonance width [Bra89, Gar87]. High excitation energies in such fusion measurements implicitly correspond to high angular momentum states populated in the compound nucleus. The observed increase in width has been empirically linked to the excitation energy and angular momentum in many studies. For instance in  $Sn$  isotopes the width has been parameterized as  $\Gamma = 4.8 + 0.0026 E_{ex}^{1.6}$  for excitation energies below  $\sim 150$  MeV [Cha87].

To understand the increase in the resonance width with excitation, it is useful to invoke the microscopic description of the resonance. The width  $\Gamma$  of the GDR in the nucleus has two components

$$\Gamma = \Gamma^\dagger + \Gamma^\downarrow. \quad (2.15)$$

The quantity  $\Gamma^\dagger$  is the escape width of the resonance and it originates from the decay of the collective doorway state to residual nuclei with a one-hole configuration resulting from the emission of a proton or a neutron.

The quantity  $\Gamma^\downarrow$  is the spreading width that arises from the coupling of the coherent 1p-1h excitation to 2p-2h and other complicated particle-hole configurations. This process is illustrated in figure 2.1.

The 1p-1h doorway resonance corresponds to a single component in the energy spectrum. Coupling of the doorway state to 2p-2h configurations results in the fragmentation of the resonance strength. The coupling to compound nuclear np-nh states

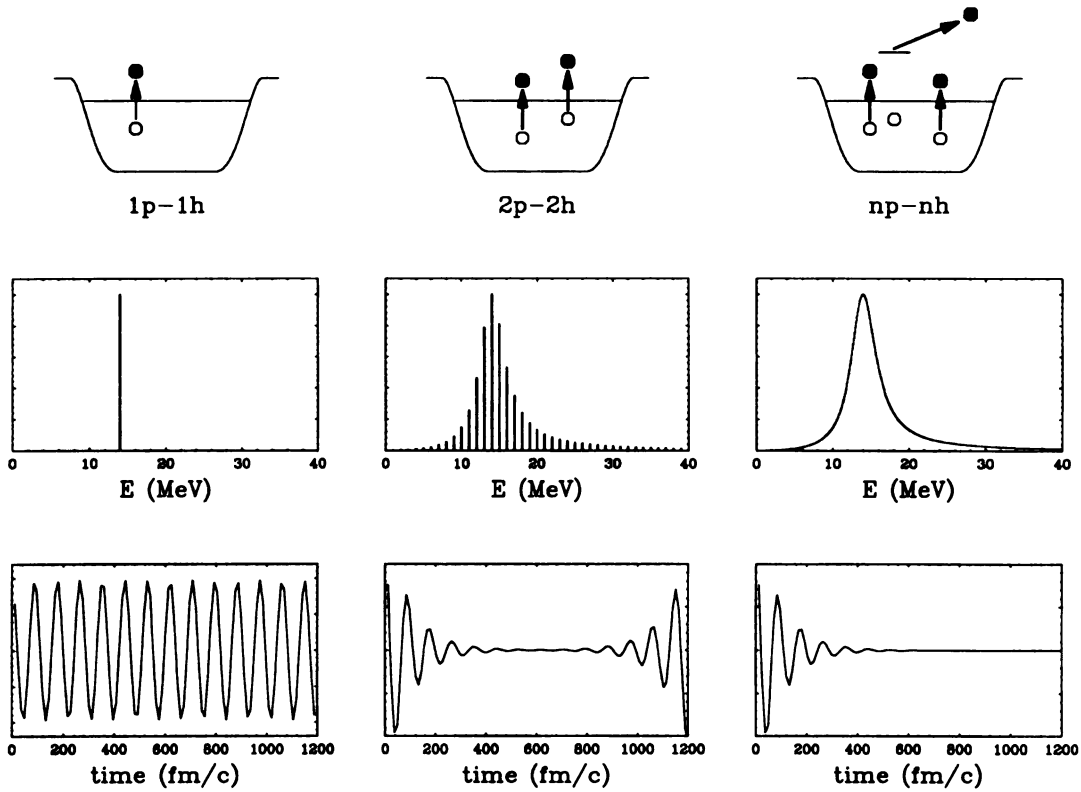


Figure 2.1: The damping of the GDR arises from its coupling to the compound nuclear states. Displayed here are the energy and time behaviour of resonance from three different stages. The first column displays the coherent 1p-1h doorway state that has a single energy component. Coupling of the 1p-1h states to the 2p-2h configurations results in the fragmentation of the resonance as shown in column 2. Finally, coupling to the complicated np-nh compound state configurations smoothes each fragmented component resulting in a spreading width in the energy which is responsible for the damping of the resonance. This is displayed in the third column.

smooths each fragmented component resulting in a spreading width for the resonance. This spreading process results in the damping of the giant dipole resonance in the nucleus. In heavy nuclei the major contribution ( $\sim 80\%$ ) to the resonance width arises from the spreading process [Ber83].

In an excited nucleus the escape width corresponding to direct particle emission is small, of the order of a few hundred keV [Sme91]. Thus the observed increase in resonance width with excitation energy should be due to an increase in the spreading width. The spreading width of the GDR arises from its coupling with other nuclear degrees of freedom such as nuclear shape. Shape fluctuations thus play an important role in the behaviour of the GDR in excited nuclei. In other words, the GDR exhibits a strong dependence on the temperature and angular momentum of the nucleus.

The free energy distribution of nuclei in the ground state exhibit deep minima that corresponds to the ground state shell configurations, especially in nuclei at and around closed shells. In an excited nucleus, even at moderate temperatures of  $T \geq 1$  MeV, the shell effects disappear and the free energy surface no longer exhibits deep minima. The surface broadens considerably and thermal fluctuations in the shape degree of freedom become important. The GDR couples to these shape fluctuations and the resonance properties convey information on the time scales of these shape variations [Goo88].

There are several models that incorporate the shape fluctuations in describing the resonance properties [Gar92]. The adiabatic model assumes that the time scale of shape fluctuations is long compared to the damping time of the GDR. In this model, the GDR strength measured in an experiment is a superposition of the strength distributions that correspond to vibrations built on all possible nuclear shapes, weighted by the probability of the nucleus for assuming that shape. The systematic increase in the resonance width seen in measurements are thus attributed to the resonance sam-

pling all possible deformations over a shallow free energy surface at high excitation energies and angular momenta.

In contrast to the adiabatic model, dynamical models take into account the relative time scales for shape fluctuation in the nucleus. In this picture the time spent by the nucleus in a given shape configuration decreases with increasing temperature. Thus the nucleus may not spend long enough time at a given point in the free energy surface for the dipole vibration to adjust its frequency to the corresponding nuclear shape. Thus the GDR never explores extreme shape transitions but only feels the average shape of the nucleus. This leads to a substantial reduction in the effect of shape fluctuations [Alh90, Orm90]. This effect, referred to as motional narrowing, has been offered as an explanation to the observed saturation in the GDR width at very high excitation in measurements performed on  $Sn$  isotopes.

The analysis of the evolution of the GDR in terms of shape fluctuations is complicated by the introduction of high angular momentum states in the compound nucleus. The increase in excitation energy of the nucleus is associated with an implicit increase in the angular momentum transferred from the entrance channel in fusion reactions.

It is thus highly desirable to perform experiments that selectively populate nuclei in narrow ranges of excitation energy and spin to provide detailed information on the nuclear surface for understanding shape fluctuations.

This work focuses on the study of nuclei at high excitation energies populated with very low angular momenta *via* the mechanism of inelastic scattering. The evolution of the GDR is studied as a function of excitation energy alone, with little influence from angular momentum effects. The measurements were performed on excited states of  $^{208}Pb$  nuclei. The ground state configuration of  $^{208}Pb$  exhibits a very deep minimum due to the existence of doubly closed shells. Figure 2.2 displays the free energy

surface for a few *Pb* isotopes calculated at different temperatures, assuming zero spin [Wer94]. The energy scale for the calculations have been translated such that the free energy is 0 MeV for zero deformation.

A deep minimum is observed in  $^{208}\text{Pb}$  at zero temperature due to the doubly closed shell configuration. The minimum is less prominent in the other neutron deficient isotopes. The figure shows that the deep minimum in  $^{208}\text{Pb}$  broadens rather rapidly with increasing temperature. The study of shape evolution of the GDR in this nucleus should thus provide interesting information on how the nuclear free energy surface evolves with temperature and how the giant dipole resonance couples with the nuclear surface.

## 2.6 Excitation by Inelastic Scattering

### 2.6.1 The Inelastic Continuum

Inelastic scattering has been an important tool in the study of the structural properties in nuclei. A wide variety of hadronic probes have been employed to study the scattering process. For instance, neutron and proton resonance scattering have been employed to reveal individual compound nuclear states in nuclei.

The absorption of neutrons and protons in the interior of the nucleus is a weak process. But the absorption is strong for composite hadronic probes like  $\alpha$ -particles and heavy ions. Composite probes do not penetrate much into the nuclear interior of the target. They are more sensitive to the surface properties of the nucleus and can therefore preferentially excite the vibrational modes of the nucleus [Fes92]. Inelastic scattering with composite probes can thus be employed to study collective excitations like the giant dipole resonance in nuclei. Furthermore, the angular momentum transferred to the target in the scattering process is low.

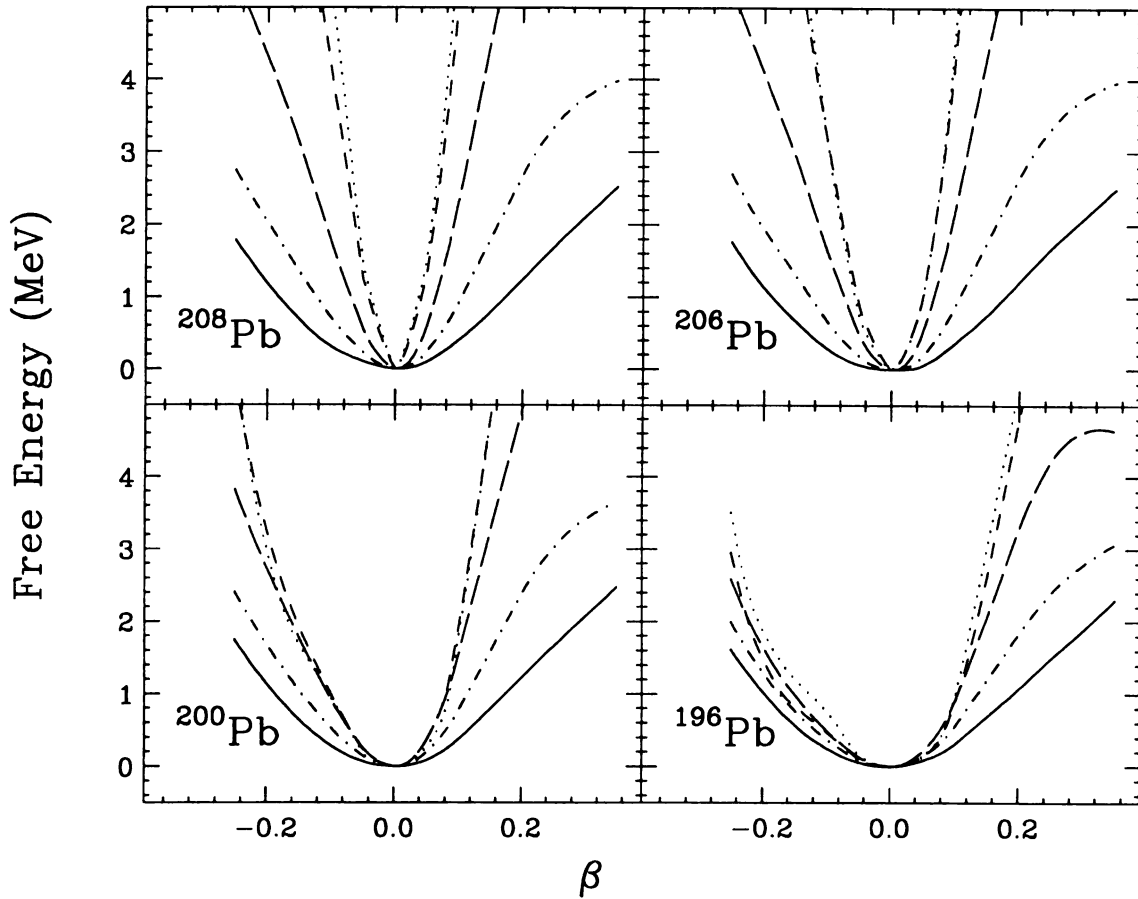


Figure 2.2: Free energy surfaces for isotopes of  $Pb$  at temperatures of 0 MeV (dots), 0.5 MeV (dashes), 1.0 MeV (long dashes), 1.5 MeV (dot-dashed) and 2.0 MeV (solid). The calculations were performed assuming zero angular momentum. The parameter  $\beta$  is a measure of the nuclear deformation. Negative values of  $\beta$  correspond to oblate deformation and positive values to prolate deformation. The energy scale for the different temperatures were translated so that the free energy is 0 MeV for zero deformation. The free energy in  $^{208}Pb$  exhibits a deep minimum at zero temperature due to the doubly closed shell structure. This minimum broadens with increasing temperature. The minimum is less prominent in the other isotopes.

Heavy ion inelastic scattering along with the coincidence measurement of particles and  $\gamma$ -rays has been applied in recent years to study the decay of giant resonances in nuclei [Bee89, Wou88]. For moderate excitation energies in the target up to  $\sim 20$  MeV the structures in the particle spectra have been well understood in inelastic scattering studies on heavy nuclei. These structures correspond to localized strengths of giant resonances, mostly the isovector giant dipole resonance (IVGDR) and isoscalar modes like the giant quadrupole (GQR) and the giant monopole (GMR) resonances.

Beyond the structures seen at the lower end of the excitation spectrum inelastic scattering studies exhibit a broad continuum in the particle spectrum that correspond to higher energy losses of the projectile. There is not much experimental information on the nature of target excitations that can contribute to this particle continuum. Theoretical calculations predict that this continuum may correspond to poorly localized distributions of higher multipolarities [Tsa75]. Recently particle and  $\gamma$ -ray coincidence measurements have been performed to search for structures in the continuum that correspond to localized multiphonon strength such as the two phonon  $GDR \times GDR$  excitation [Blu88, Fra88, Bee94]. The identification and characterization of the wide variety of collective modes of excitation that exist in the continuum region of the excitation spectrum is a major task in experimental nuclear structure physics.

A recent experiment employing the inelastic scattering of 84 MeV/A  $^{17}\text{O}$  on  $^{208}\text{Pb}$  searched for giant dipole resonance built on highly excited states of the target in the inelastic continuum [Tho91]. High energy  $\gamma$ -ray spectra measured in coincidence with the scattered projectile nuclei showed an enhancement in the  $\gamma$ -ray multiplicity in the giant dipole resonance energy region. Furthermore, the inelastic particle spectrum in coincidence with high energy  $\gamma$ -ray emission exhibited structures corresponding to the individual neutron decay channels of the excited nucleus. This observation



is evidence for equilibrated emission from the excited target. Statistical model calculations are thus applicable to the analysis of the excited states populated by the inelastic scattering process.

A main criterion in the selection of the inelastic probe is that there are no contributions to the  $\gamma$ -ray spectrum from projectile excitation. Projectiles with low nucleon binding energy are thus a good choice. The outgoing particle in the inelastic scattering process needs to be isotopically identified. Such measurements warrant the use of a high resolution spectrometer. In the absence of a large solid angle spectrometer to isotopically identify the scattered projectile, it becomes necessary to use discrete particle detector arrays employing silicon or organic scintillators. The choice of the projectile nuclei is then restricted to those that can be isotopically identified in the detector system.

In this work the giant dipole resonance excitations built on highly excited states of  $^{208}\text{Pb}$  were studied with inelastic scattering of 40 MeV/A  $\alpha$ -particles. There are no experimentally known bound excited states of the  $\alpha$ -particle. Contamination from projectile excitation is thus eliminated.

The giant dipole resonance excitation is an isovector mode and is therefore characterized by an isospin transition of  $\Delta T = 1$ . The  $\alpha$ -particle, being a  $Z = N$  nucleus, has an isospin value of  $T = 0$ . Exciting giant dipole resonance states by means of inelastic  $\alpha$  scattering is inhibited due to the isospin selection rules. Nevertheless, isospin is a good symmetry only in light nuclei [Sno86]. In excited heavy nuclei, the isospin mixing process results in the possibility of exciting isovector modes by means of a  $T = 0$  probe [Won90].

## 2.6.2 Comparison to Fusion-Evaporation Reactions

The GDR built on excited states in nuclei have been conventionally studied via fusion-evaporation reactions. For energies above the coulomb barrier the fusion cross section for such reactions is relatively large ( $\sim 1$  barn). The formed compound nuclear system equilibrates rapidly and the excitation energy is shared amongst all available degrees of freedom. Statistical model calculations are thus applicable to the study of such systems.

One drawback in using fusion-evaporation reactions for the study of collective excitation modes like the GDR is that the compound system is formed with large spins due to the angular momentum transfer from the incoming projectile. Furthermore, the range of angular momenta populated in the fusion process is rather large. Thus it becomes difficult to study the properties of collective excitations as a function of excitation energy alone, decoupled from spin effects.

Figure 2.3 compares calculated angular momenta populated in inelastic scattering and fusion reactions. The calculations are shown for two different excitation energies. The inelastic scattering calculation was performed for 40 MeV/nucleon  $\alpha$ -particles on  $^{208}\text{Pb}$ . The angular momentum transfer in the inelastic process is given by

$$I = b p_{tgt} \hbar \quad (2.16)$$

where the momentum transfer to the target,  $p_{tgt}$ , is the difference in the momenta of the projectile between the incoming and outgoing channels. The impact parameter  $b$  was varied between the sum of ‘matter half density’ radii of the nuclei and the ‘nuclear interaction radius’ [Wil80].

The fusion reaction calculation was done for a typical reaction of  $^{19}\text{F} + ^{181}\text{Ta}$  form-

ing  $^{200}\text{Pb}$ . The cross section for the fusion reaction is given by

$$\sigma_{fus} = \frac{\pi}{k^2} \sum_{I=0}^{\infty} (2I+1) T_I, \quad (2.17)$$

where the transmission coefficient  $T_I$  is parametrized in the sharp cut-off model in terms of the maximum angular momentum  $I_{max}$  and diffuseness  $\delta_I$ , and is given by

$$T_I = \left( 1 + \exp \left( \frac{I - I_{max}}{\delta_I} \right) \right)^{-1}. \quad (2.18)$$

It is clear from the figure that the angular momenta populated in the inelastic scattering process are much smaller, and are spread over a rather narrow range, compared to the population in the fusion channel.

In the inelastic scattering approach, the statistics of  $\gamma$  rays in coincidence with the scattered projectile is rather poor. Thus it is not possible to look at a very narrow range of target excitation energies. Rather, a 10 MeV wide bin in the excitation energy is chosen. Figure 2.4 compares the nuclear population in the excitation plane for the fusion and inelastic processes. The fusion process creates a compound nuclear population with a narrow spread in excitation energy, but with a large spread in angular momenta. The inelastic scattering process populates nuclei in a narrow cell in the excitation plane, over small ranges of excitation energy and angular momenta.

Fusion-evaporation reactions often produce nuclei that are neutron deficient. The  $N/Z$  ratio for the projectile and the target in the entrance channel are usually lower than the  $N/Z$  ratio of the stable isotope of the product nucleus formed. Thus it is not possible by means of fusion reactions to measure the collective properties in stable nuclei at high excitation energies and compare them with known ground state properties.

Another advantage of inelastic scattering is that different excitation energy ranges in the target can be studied by applying excitation energy cuts in the inelastic particle

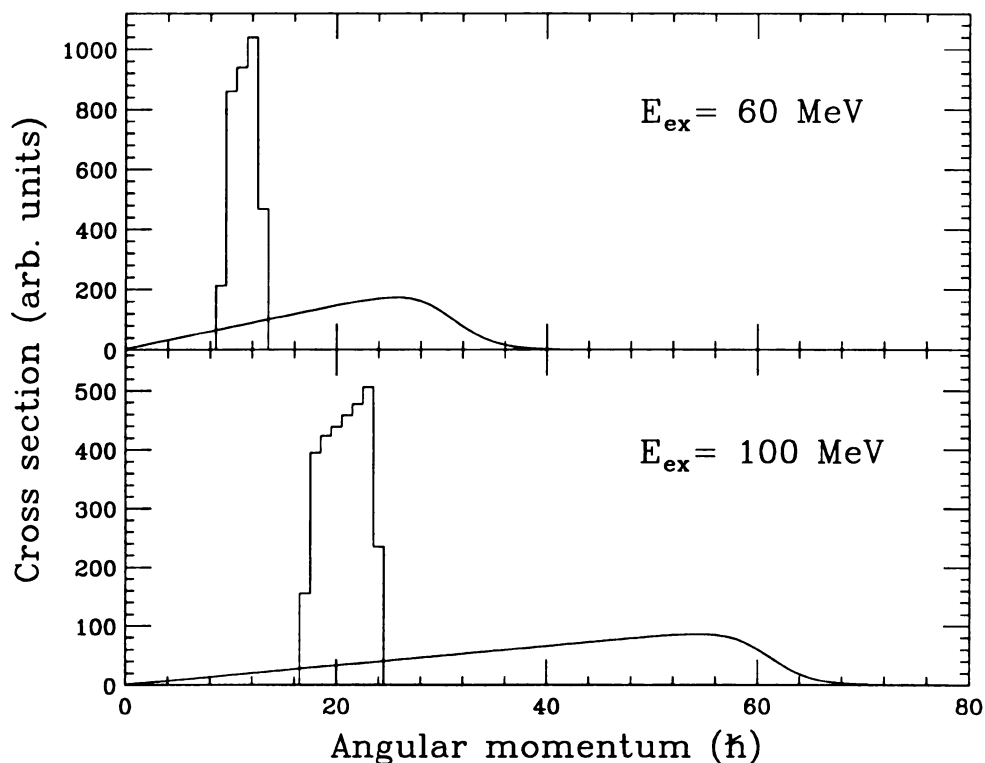


Figure 2.3: Comparison of angular momenta imparted to the target in fusion reactions versus inelastic scattering. The comparison is shown for two different excitation energies. The histograms are the angular momenta calculated for inelastic  $\alpha$  scattering on  $^{208}\text{Pb}$  at 40 MeV/nucleon. The solid lines are angular momentum transfers computed for a typical fusion reaction of  $^{19}\text{F} + ^{181}\text{Ta}$  forming  $^{200}\text{Pb}$ . The angular momentum populated in the inelastic scattering is low. In the fusion channel, the angular momentum is rather large and is spread over a broad range.

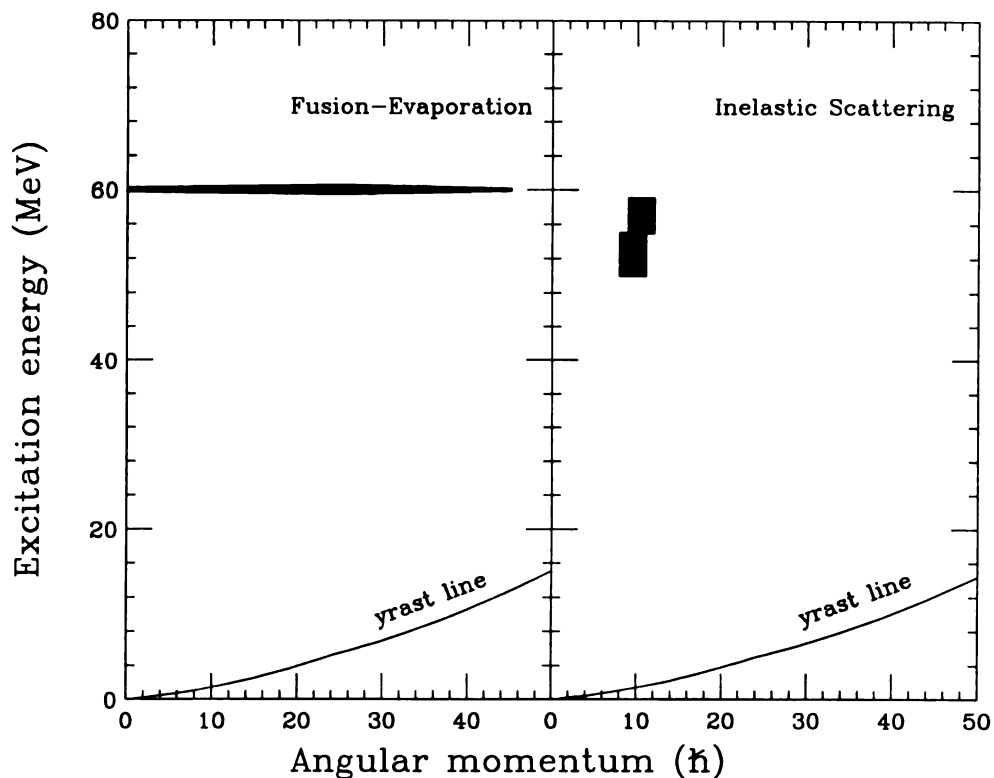


Figure 2.4: Distribution of excited nuclei populated in fusion reactions (left) and inelastic scattering (right) plotted on the excitation plane. The yrast line corresponds to the minimum excitation energy in the nucleus for a given angular momentum. The fusion population is shown for  $^{200}\text{Pb}$  nuclei at 60 MeV excitation energy. The angular momentum in the fusion channel is large and is spread over a broad range. In the inelastic scattering method, a range of excitation energies is selected in the analysis. The population shown here is for inelastic  $\alpha$  scattering at 40 MeV/nucleon on  $^{208}\text{Pb}$  forming excited target nuclei in the energy range of 50–59 MeV. Since the angular momenta populated are very low and the excitation energy bin is only 10 MeV wide, the population of excited nuclei is restricted to a rather narrow cell in the excitation plane.

spectrum. Thus the nuclear properties as a function of a wide range of excitation energies can be measured in a single experiment.

# Chapter 3

## Experimental Setup

### 3.1 Introduction

A  $3 \text{ mg/cm}^2$  thick isotopically enriched  $^{208}\text{Pb}$  target was bombarded by a  $40 \text{ MeV/nucleon}$   $\alpha$  beam from the K1200 Cyclotron. The target was mounted in the center of a scattering chamber that housed an array of particle detectors. High energy  $\gamma$ -rays from the decay of the excited target nucleus were measured in coincidence with inelastically scattered projectiles. The  $\gamma$ -ray detectors were arranged outside the scattering chamber. The residual beam was stopped in a shielded faraday cup and the beam current was monitored during the experiment. Typical beam currents were around  $3 \text{ pA}$ .

The following section describes the details of the detector systems used in the experiment.

### 3.2 Detectors

The  $\gamma$ -ray measurement required good energy resolution as well as good timing resolution to allow  $\gamma$ -neutron discrimination. Only moderate energy resolution was necessary for the particle detectors, however particle identification with isotopic resolution was essential.

### 3.2.1 BaF<sub>2</sub> Detector Arrays

The high energy  $\gamma$  rays were measured with BaF<sub>2</sub> scintillator detectors. These detectors have a very fast response which allows sub-nanosecond timing [Nov87]. This is necessary in discriminating  $\gamma$  rays from fast neutrons by time of flight. The setup consisted of 95 hexagonal BaF<sub>2</sub> crystals arranged in 5 packs of 19 detectors each. Four of these packs were from Oak Ridge National Laboratory (ORNL) and the fifth pack was from MSU. Figure 3.1 shows a schematic diagram of the BaF<sub>2</sub> packs in the experimental setup.

The ORNL detectors were each 20 cm in length with a face dimension corresponding to an inscribed circle of 6.5 cm diameter. The MSU detectors were 25 cm in length and the diameter of the inscribed circle was 6 cm. The five packs were placed around the target at a distance of  $\sim 40$  cm and were centered at laboratory angles of  $60^\circ(2)$ ,  $72^\circ(2)$  and  $112^\circ$ . The solid angle coverage was  $\sim 17\%$  of  $4\pi$ .

### 3.2.2 Dwarf Ball/Wall CsI Array

The inelastically scattered projectiles and other light charged reaction products were detected using the Washington University DWARF BALL and DWARF WALL  $4\pi$  CsI(Tl) array [Str90]. In the present experimental setup the DWARF WALL consisted of 35 CsI(Tl) plastic phoswich detectors, each 20 mm thick, arranged in four rings centered at laboratory angles of  $14.78^\circ$ ,  $22.39^\circ$ ,  $23.18^\circ$  and  $31.03^\circ$ . The angular coverage in the lab was from  $\sim 9^\circ$  to  $\sim 36^\circ$ . The detectors were at a distance of 13 cm from the target and the total solid angle covered was  $\sim 0.8$  ster. The scintillators were thick enough to stop the highest energy  $\alpha$  particles of 160 MeV corresponding to the initial beam energy. High energy  $Z = 1$  particles could not be stopped and they punched through.



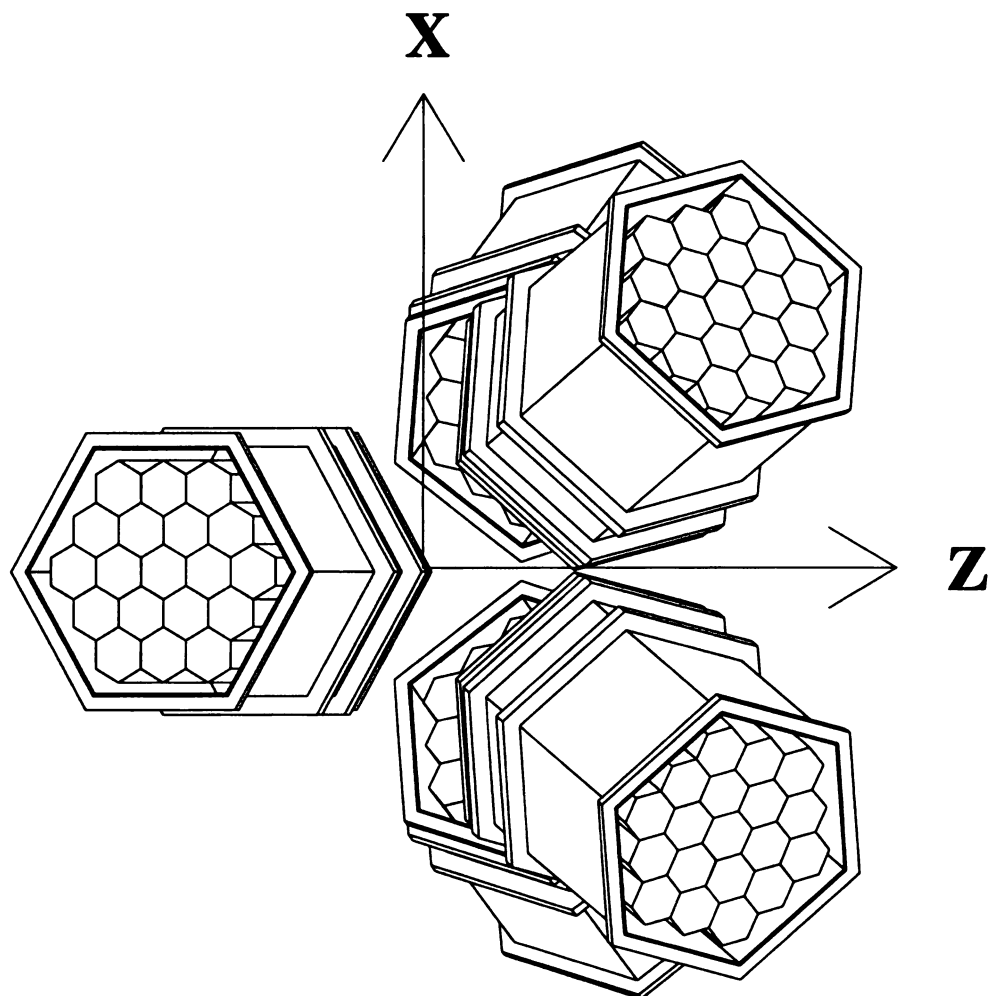


Figure 3.1: Schematic diagram showing the positioning of the BaF<sub>2</sub> packs in the experiment. The beam direction is along the Z axis. The DWARF scattering chamber was placed at the center of the co-ordinate system.

Figure 3.2 shows the beam's eye view of the DWARF WALL array. The numbers in the figure indicate the ring numbers that were assigned to the detectors.

In our setup the DWARF BALL consisted of 64 close packed CsI(Tl) detectors arranged in thirteen rings covering laboratory angles of  $\sim 36^\circ$  to  $\sim 160^\circ$ . The detectors were at a distance of 4 cm from the target. The thickness of the scintillator crystals varied from  $\sim 8$  mm at forward angles to  $\sim 4$  mm at the most backward angle. The WALL and the BALL arrays together covered a solid angle of  $\sim 95\%$  of  $4\pi$ .

### 3.3 Electronics

Figure 3.3 shows the schematic block diagram of the BaF<sub>2</sub> electronics used in the experiment. A schematic of the DWARF ARRAY electronics can be found in reference [Str90].

The ORNL detectors were equipped with photomultiplier tubes that provided two anode signals. The photomultiplier tubes for the MSU detectors provided only one anode signal which was split to provide two identical signals. For the analog path of the electronics, one copy of the PMT signal from each detector was fed to 'Delay and Splitter' boxes. These boxes grouped the 95 detectors into seven 'banks'. The signals were delayed by 500 ns and then split to provide two outputs. One output was fed to the 'E FERA' LECROY 4300B modules and the other output was fed to the ' $\Delta E$  FERA' LECROY 4300B modules. The pedestals for these modules were subtracted on-line. The light output from the BaF<sub>2</sub> crystal has two components: a fast component with a decay time of 0.6 ns at a wave length of 220 nm, and a slower component with a decay time of 620 ns at a wave length of 310 nm [Kno89]. The gate signal for the ' $\Delta E$  FERA' was set to a width of 50 ns, with a lead time of 15 ns. The integration was thus performed on the first 35 ns of the detector signal, yielding the

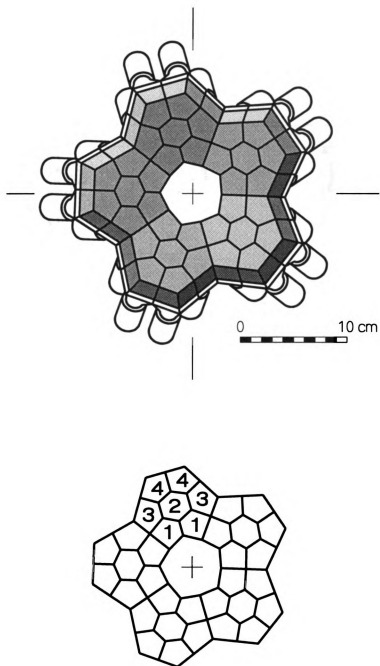


Figure 3.2: The DWARF WALL array as seen by the incoming beam. The top figure is a schematic view of the WALL array. The bottom figure shows the numbering scheme employed for the detectors. The rings were centered at laboratory angles of  $14.78^\circ$ ,  $22.39^\circ$ ,  $23.18^\circ$  and  $31.03^\circ$ .

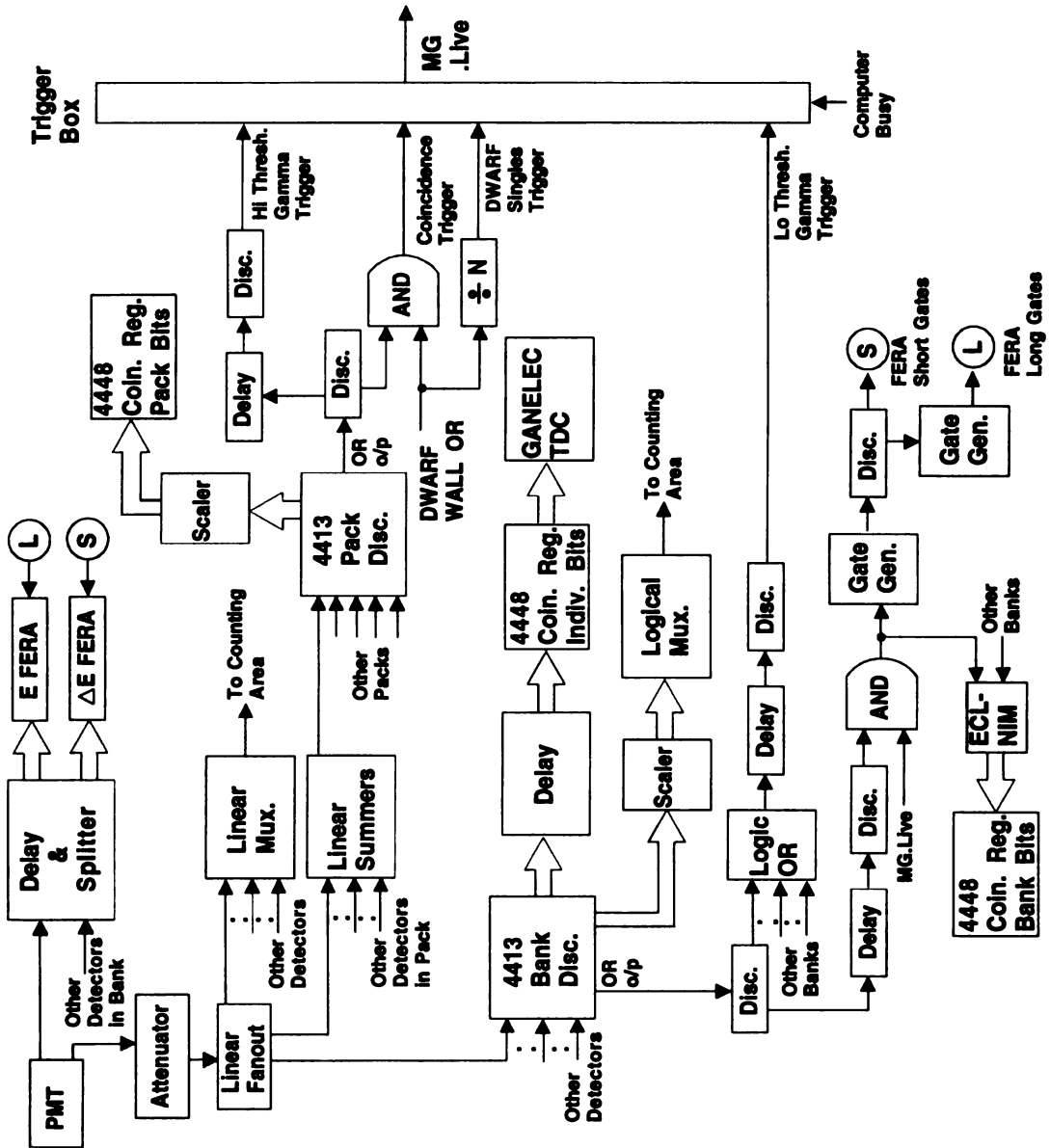


Figure 3.3: Block diagram of the electronics for the BaF<sub>2</sub> detector arrays.

energy in the fast component. The 'E FERA' modules integrated the entire signal over  $1.5 \mu\text{sec}$ , yielding the total energy deposited in the crystals.

The second copy of the PMT signals were used for the logic path of the electronics. These signals were first fed to attenuator modules that were used to gain match the fast light output of the different PMT signals. The output of the attenuators were fed to linear fanout modules which produced three copies. One copy of each signal was fed to a bank of linear multiplexer modules. The output from the multiplexer bank was patched through to the counting area. The multiplexers could be addressed through CAMAC commands thus allowing any one of the 95 linear signals to be monitored on the oscilloscope in the counting area during the experiment. The second set of outputs from the linear fanout modules were fed to linear summing amplifiers. The signals of the 19 detectors within each array were added in the summing modules. The summed outputs from the five groups were fed to a LECROY 4413 discriminator module. This module allowed setting thresholds on these individual 'pack sum' signals. The thresholds on all the packs was set at  $\sim 4 \text{ MeV}$ . The bus output of the 'pack sum' discriminator was daisy chained to a scaler module and to a LECROY 4448 coincidence register to record bit information on which array fired in an event. The 'pack sum' discriminator also provided a NIM output which was the OR of all the five array discriminators. This output served as the high threshold  $\gamma$  trigger which was required for a coincidence event.

The third and the last copy of the linear fanout modules were grouped in seven 'banks'. The signals in each 'bank' were fed to LECROY 4413 discriminator modules. These modules set the individual thresholds on all the 95 detectors. The thresholds were set at  $\sim 500 \text{ keV}$ . The bus outputs of these 'bank' discriminators were fed to CAMAC delay modules which delayed these logic signals by 250 nsec. The output of the delay modules were used as the stop signal for the TDC modules to record

event timing for each detector. The common start signal for the TDC came from a coincidence of the Cyclotron radiofrequency signal and the mastergate signal from the trigger box. The outputs of the delay modules were also daisy chained to LECROY 4448 coincidence register modules to record bit information on which detectors fired in an event. A second set of bus outputs from the 'bank' discriminators were fed to scaler units and to a bank of logic multiplexers. The output of the multiplexer bank was patched to the counting area. It was thus possible to monitor the logic signals from all detectors during the experiment. The OR outputs from each 'bank' discriminator were fed to a logic OR module to create a logic signal when any one of the 95 detectors had a signal pulse that crossed the individual thresholds. The output of this OR module thus formed the low threshold  $\gamma$  trigger. This trigger was used mainly for calibration purposes. The gate signals for setting the integration times for the FERA units for each 'bank' were derived from the OR output of the discriminator for that 'bank'. The 'bank' discriminator OR outputs were first fed to coincidence units that allowed the gates to be vetoed when the computer was busy. Gates for the FERA units were thus produced only when the computer was ready for processing the event.

The BaF<sub>2</sub> detectors were gain matched in energy by adjusting the high voltage inputs to the PMT's so that the calibration peaks lined up in the same data channel for  $\gamma$ -rays of the same energy. This energy gain matching was performed with data acquired from the radio-active sources. It was also necessary to gain match the fast component of the light output from the detectors so that common trigger thresholds applied to the signals in the logic path of the electronics have a uniform effect. This was achieved as follows. After gain matching the detectors for the total energy, cosmic data was acquired for all detectors by setting the common trigger threshold at an arbitrary value. The threshold cutoff point in the  $\Delta E$  channel was recorded for

all detectors. These cutoff points were used to decide the settings for the attenuator modules in the logic path thus yielding matched signal amplitudes.

For the DWARF electronics, the signal from the PMT of each detector was split to provide three copies. The light output from the CsI(Tl) crystal has two components. The first component has a decay time of 0.3–1.0  $\mu\text{s}$  depending on the particle type, and the second component has a decay time of 7  $\mu\text{s}$  independent of the particle [Kno89]. Two copies of the PMT signal were fed to two different set of FERA modules, one for the ‘Slow’ integration and the other for the ‘Tail’ integration. For the ‘Slow’ FERA’s the gate was set to integrate over a time period of  $\sim 340$  ns, leaving out the first  $\sim 35$  ns of the signal. The gate for the ‘Tail’ FERA’s were set to start 1.5  $\mu\text{s}$  after the start of the signal pulse and the integration time was 1.5  $\mu\text{s}$ . In the logic path, the signals from the 35 DWARF WALL detectors were fed to logic ‘OR’ units to form a ‘DWARF WALL OR’ trigger. This trigger was used to form the coincidence with the high threshold  $\gamma$  trigger yielding the ‘Coincidence Trigger’ for the experiment. A copy of the ‘DWARF WALL OR’ trigger was scaled down by a factor of 64 and was used as a ‘DWARF Singles’ trigger to record singles data from the DWARF array. The individual detector event times for the DWARF array were recorded using ‘Time to FERA’ converter modules. These modules were operated in a common start mode. The stops came from the individual detectors, and the start signal was derived from the coincidence of the ‘DWARF WALL OR’ and the high threshold  $\gamma$  trigger. Information on which DWARF detectors were present in an event was recorded using LECROY 4448 bit register modules.

During the experiment, the active triggers were the ‘Coincidence Trigger’ and the ‘DWARF Singles’ trigger. The energy and time information for the DWARF BALL/WALL detectors that fired in an event were recorded for both the ‘DWARF Singles’ trigger and the ‘Coincidence Trigger’. The energy and time information for

the BaF<sub>2</sub> detectors that fired were recorded for events in which the ‘Coincidence Trigger’ was present. Furthermore, for each event the time of the mastergate signal relative to the Cyclotron radio-frequency signal was recorded as well.

### **3.4 Data Acquisition**

The NSCL acquisition system was used to set up the CAMAC electronics for the experiment. All the electronics was set up inside the vault. To monitor detector performance, the analog and logic signals from the two detector systems were multiplexed and patched through to the counting area. The BaF<sub>2</sub> electronics and the DWARF Array electronics were integrated in one CAMAC branch and were controlled by a front end code that was written specifically for the experiment. For each event the front end code identified the detectors that were present in the event from bit registers. The code then read the modules associated with those detectors and wrote them to the data stream together with a number that was assigned to each detector. Event type was also recorded. The data stream was routed to a taping process, and was also monitored by an on-line data analysis program.



# Chapter 4

## Data Analysis

### 4.1 Introduction

The off-line analysis of the data was performed with a modified version of the NSCL data analysis program SARA. The modifications were necessary because of the different data structure created by the customized front end code used in the experiment.

Initially the data was scanned and particle identification (PID) histograms were created for both the DWARF detectors and BaF<sub>2</sub> detectors. Gates were drawn on these PID plots to identify different isotopes in the DWARF detectors, and  $\gamma$  and neutron events in the BaF<sub>2</sub> detectors. All the data sets were then scanned with the PID gate conditions and a filtered output was created. For each event, only those detectors that had clean particle identification were written out. Subsequent analysis of the data were performed using these filtered data tapes.

### 4.2 Particle Spectra

#### 4.2.1 Particle Identification

Particle identification in the DWARF detectors was obtained from the ‘Slow’ and ‘Tail’ energies recorded for each event. A two dimensional plot of the ‘Tail’ versus the

‘Slow’ parameters was not sufficient to clearly identify the  $\alpha$  events from  ${}^3\text{He}$  and to distinguish between  $p$ ,  $d$  and  $t$  events in the detectors. In order to draw unambiguous gates for particle identification, the DWARF parameters were transformed as follows.

First, a two dimensional plot of the measured ‘Tail’ versus ‘Slow’ parameters was created for each detector. Boundary lines were drawn on these plots to include the data range of interest. For each data point within the boundaries, a new ‘Tail’ parameter was computed as shown in figure 4.1. Two dimensional plots of the new ‘Tail’ parameter versus the recorded ‘Slow’ parameter were then created. Particle identification gates were drawn on these transformed plots. Figure 4.2 shows the ‘Tail’ versus ‘Slow’ plots before and after the transformation.

#### **4.2.2 Calibration of the DWARF Ball/Wall Array**

The WALL array was calibrated by  $\alpha$  beams of various energies. The primary  $\alpha$  beam from the cyclotron was degraded using aluminum absorbers of various thicknesses in the A1200 beam analysis device [She92]. The degraded beams were also subject to momentum cuts of  $\sim 1\%$  in the A1200. The beams were then tuned to the vault and  $\alpha$  singles data was recorded for all the WALL detectors. Beam energies of 21.6, 27.19, 31.72 and 36.07 MeV/nucleon were used for the calibration. The calibration data was scanned back, the elastic peaks were corrected for FERA pedestals and a second order fit was employed to yield calibration curves for each detector.

Since down scaled particle singles in the DWARF detectors were recorded during the experiment it was possible to monitor gain shifts in the WALL detectors by monitoring the peak position of the elastically scattered  $\alpha$ -particles. Gain shifts in the WALL array were thus corrected for in the analysis.

Since the grazing angle for the  $\alpha$  scattering at the calibration energies was small

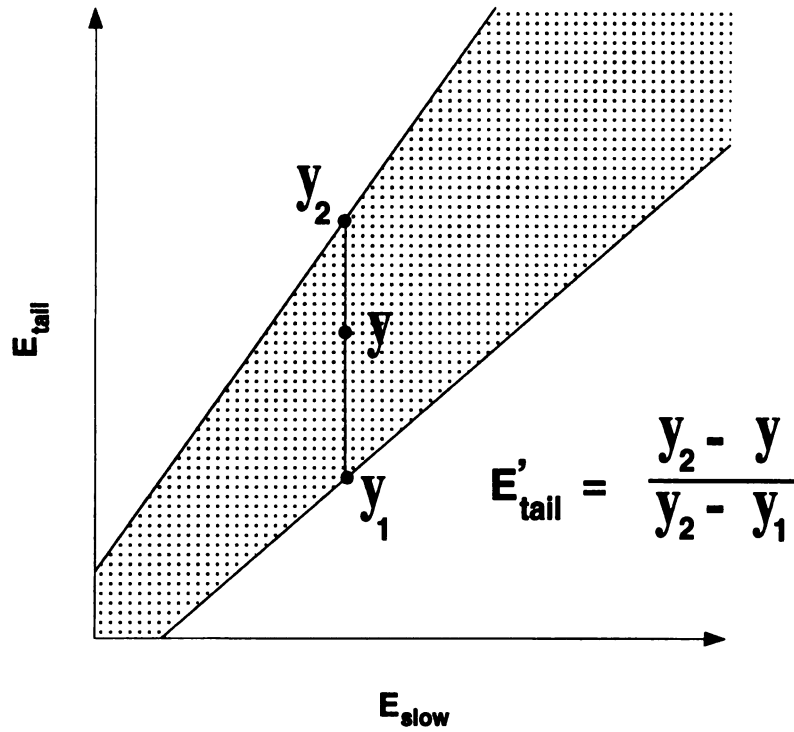


Figure 4.1: Geometric transformation employed to obtain particle identification in DWARF array detectors. For each detector a two dimensional plot of the measured  $E_{tail}$  energy versus the  $E_{slow}$  energy were plotted. Two boundary lines were drawn on the plots as shown in figure. For each measured point, a new  $E_{tail}$  parameter was computed. Two dimensional plots of the new  $E_{tail}$  parameter versus the  $E_{slow}$  parameter were created to obtain better particle identification.

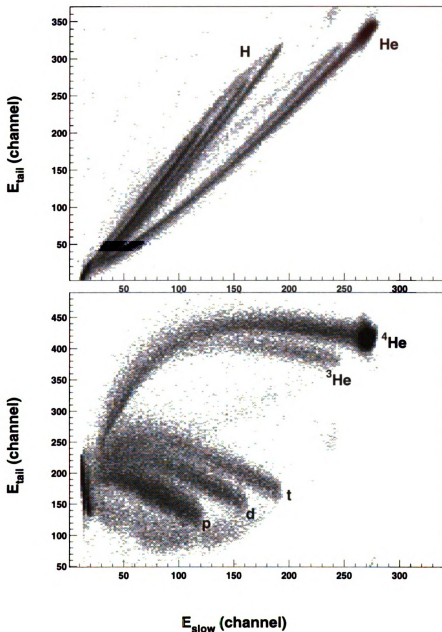


Figure 4.2: Two dimensional plots of the tail parameter versus the slow parameter from a typical DWARF WALL detector. The top panel shows the plot before the geometric transformation explained in text was applied. The bottom panel shows the plot after the geometric transformation. The improvement in particle identification is clearly seen.

( $\sim 15^\circ$  at the lowest energy), it was not possible to observe elastic peaks in detectors beyond the WALL array. The BALL array was thus not calibrated during the experiments. In the offline analysis, scanning the singles data from the BALL array yielded information on proton punch through points. From the thickness of the CsI crystals and the punch through points, it was possible to obtain a rough calibration for protons in the BALL array. This calibration was used to look at kinematics of  $\alpha$ -proton coincidence events to yield information on background processes like knockout and pickup-decay.

### **4.2.3 Resolution, Efficiency and Response**

The resolution of a typical CsI detector in the WALL array was 3.2% for  $\alpha$ -particles at 160 MeV. This resolution was sufficient because the  $\alpha$  spectra from the WALL array were binned in broad intervals of 10 MeV to obtain the coincidence  $\gamma$ -ray spectra. The geometric efficiency of the WALL array was  $\sim 6\%$  of  $4\pi$ . The count rates in the WALL array detectors were maintained at around 3000 counts/second or less in order to avoid degradation in the response due to pile up.

## **4.3 Coincidence $\gamma$ -ray Spectra**

The energies and times measured by the BaF<sub>2</sub> detectors were recorded for coincidence events where a particle was detected in the WALL array and the high threshold  $\gamma$  trigger was present. The  $\gamma$ -ray energies of interest ranged from a few MeV up to  $\sim 30$  MeV. The following subsections discuss various aspects of the analysis of the  $\gamma$ -ray spectra.

### 4.3.1 Energy Calibration

The low energy range of the  $\gamma$ -ray spectra was calibrated with radio-active sources. Known  $\gamma$ -ray transitions from  $^{207}\text{Bi}$ (569.65 keV, 1063.64 keV),  $^{228}\text{Th}$ (2614.5 keV) and a Plutonium-Beryllium source (3928 keV, 4439 keV) were used for calibration energies in the range of  $\sim 500$  keV to  $\sim 4.5$  MeV.

The GDR energy for the target studied is peaked around 13 MeV. Thus it was important to obtain a calibration point in this mid energy range. Inelastic  $\alpha$  scattering on a thick  $^{12}\text{C}$  target excited the 15.11 MeV level in carbon and the subsequent  $\gamma$ -ray decay of this state was detected.

An additional calibration point around 40 MeV was obtained from the measurement of cosmic muons in the detectors. Data was collected with all detector packs in the horizontal position. The interaction of the cosmic muons in the detectors was simulated using the monte carlo code GEANT [Bru86]. The detector geometry was put in explicitly in the simulation and the peak energy for the cosmic interaction was obtained.

Pedestal subtraction for the  $\text{BaF}_2$  FERA's was done on line. The calibration data were binned in 100 keV bins and a second order fit was employed to yield calibration curves for each detector.

### 4.3.2 Neutron Separation

A major source of contamination to the  $\gamma$ -ray spectrum can come from fast neutrons. The  $\text{BaF}_2$  arrays were placed as close as  $\sim 40$  cm from the target. With a 40 MeV/nucleon beam, neutrons with energies close to the beam energy per nucleon take  $\sim 5$  ns to reach the detectors. A  $\gamma$ -ray takes 1.33 ns to traverse the same distance. Hence it is important that one obtains good timing discrimination between  $\gamma$ -ray and

neutron events in the detectors. BaF<sub>2</sub> detectors have an inherent time resolution of less than a nanosecond. This coupled with a sub-nanosecond beam timing resulted in obtaining good n- $\gamma$  separation. In the analysis,  $\gamma$  ray events were distinguished from neutrons from a two dimensional plot of the energy deposited in the detector versus the time of flight. The time of flight was measured relative to the cyclotron radio-frequency signal. Figure 4.3 shows this two dimensional spectrum from one of the forward angle detectors. The  $\gamma$ -ray and neutron groups are well separated.

Figure 4.4 shows the projection of the energy versus time of flight plot on the time axis from two different BaF<sub>2</sub> detectors. The detectors were placed at laboratory angles of 60° and 112°. The projection was done for events with energy above the high energy trigger threshold of  $\sim 4$  MeV. The  $\gamma$ -ray peak is sharp in both detectors and has a full width at half maximum of  $\sim 1$  ns.

### 4.3.3 Region Sum for Improved Response

To obtain the  $\gamma$ -ray spectrum for each detector pack, a region summing technique was employed. The detector with the largest  $\gamma$ -ray energy was identified for each event. Then the energies deposited in the nearest neighbour detectors were added yielding a region sum. At the high  $\gamma$ -ray energies measured, the predominant mechanism of interaction in the detectors is by production of electron-positron pairs [Kno89]. Due to the limited size of an individual detector, one often encounters a loss in the measured energy due to the escape of one or both of the 511 keV photons from the annihilation of the positron. It is then most probable that the escaped photon is detected in a nearest neighbour detector. Thus it is only necessary to add back the energies from the nearest neighbours and not from all the detectors in the pack. In contrast to adding all the energy within one pack, this reduces the chance of pileup.

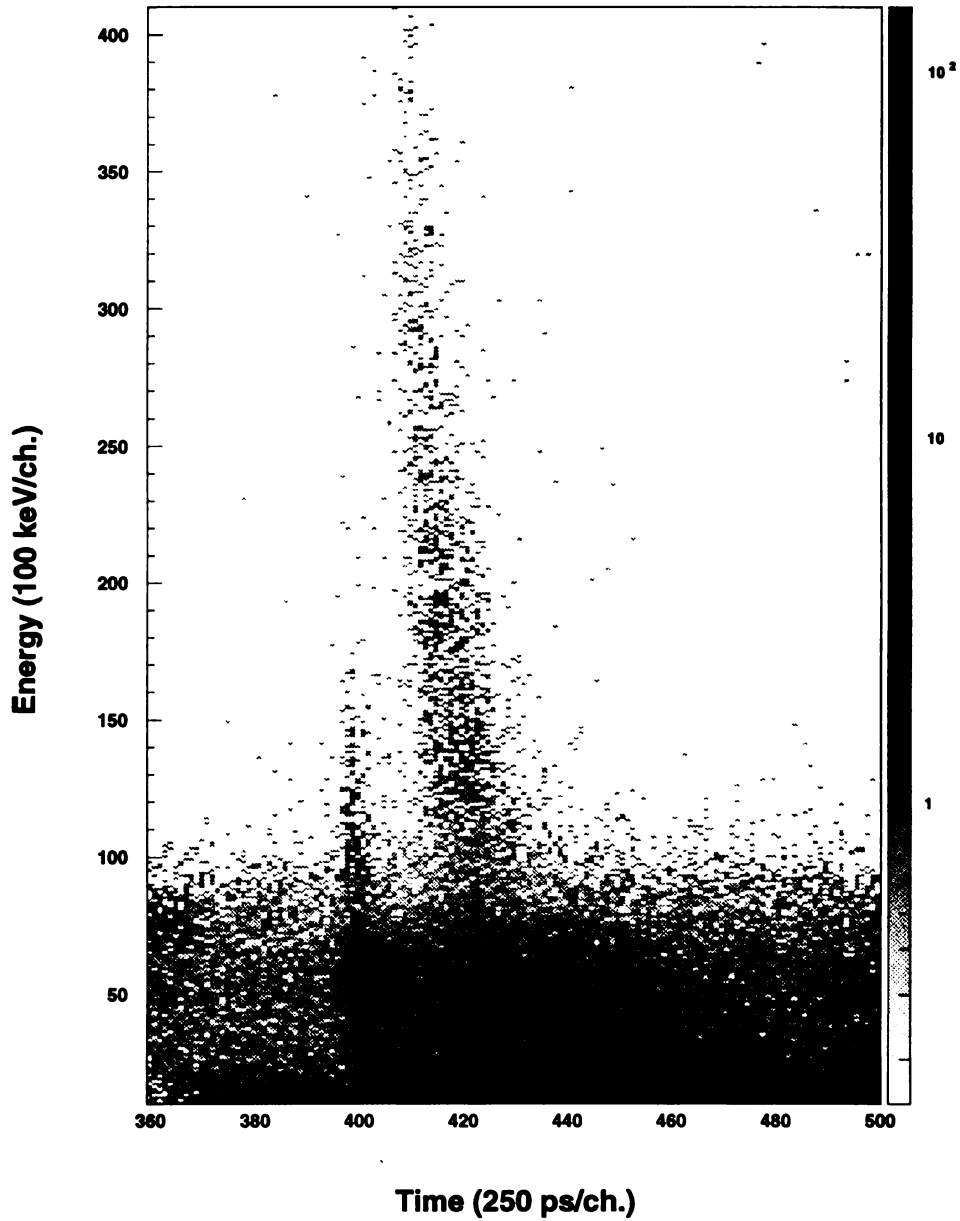


**Figure 4.3:** A two dimensional plot of the measured energy versus time of flight in a  $\text{BaF}_2$  detector at a forward angle of  $60^\circ$ . The time of flight was measured relative to the cyclotron RF signal. The group with the lower value of time of flight is from  $\gamma$  rays and the broader group to the right is from neutrons. The two groups are well separated leading to unambiguous determination of event type in the  $\text{BaF}_2$  detectors.



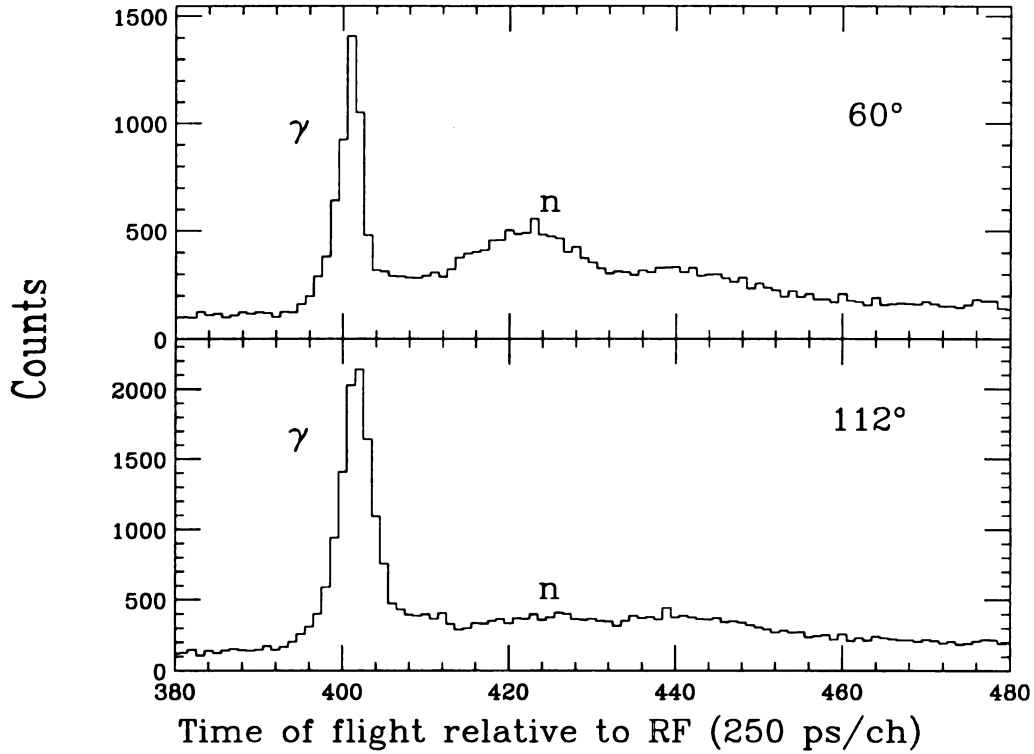


**Figure 4.4:** Time of flight in  $\text{BaF}_2$  detectors measured relative to the cyclotron radio frequency signal. The top panel is the time spectrum from a detector placed at an angle of  $60^\circ$  in laboratory and the bottom panel is the time spectrum from a detector at  $112^\circ$ . The neutron peak is more prominent in the forward angle detector. The  $\gamma$ -ray peak is sharp and is well separated from the neutrons in both cases. The full width at half maximum of the  $\gamma$ -ray peak is  $\sim 1$  nanosecond.

### 4.3.4 Resolution, Efficiency and Response

The resolution in a typical BaF<sub>2</sub> detectors for a 2.61 MeV  $\gamma$  ray from a <sup>228</sup>Th source was  $\sim 6.4\%$ . The detector efficiency and response to  $\gamma$  rays of energies in the range of interest were obtained by simulations using the monte carlo code GEANT [Bru86].

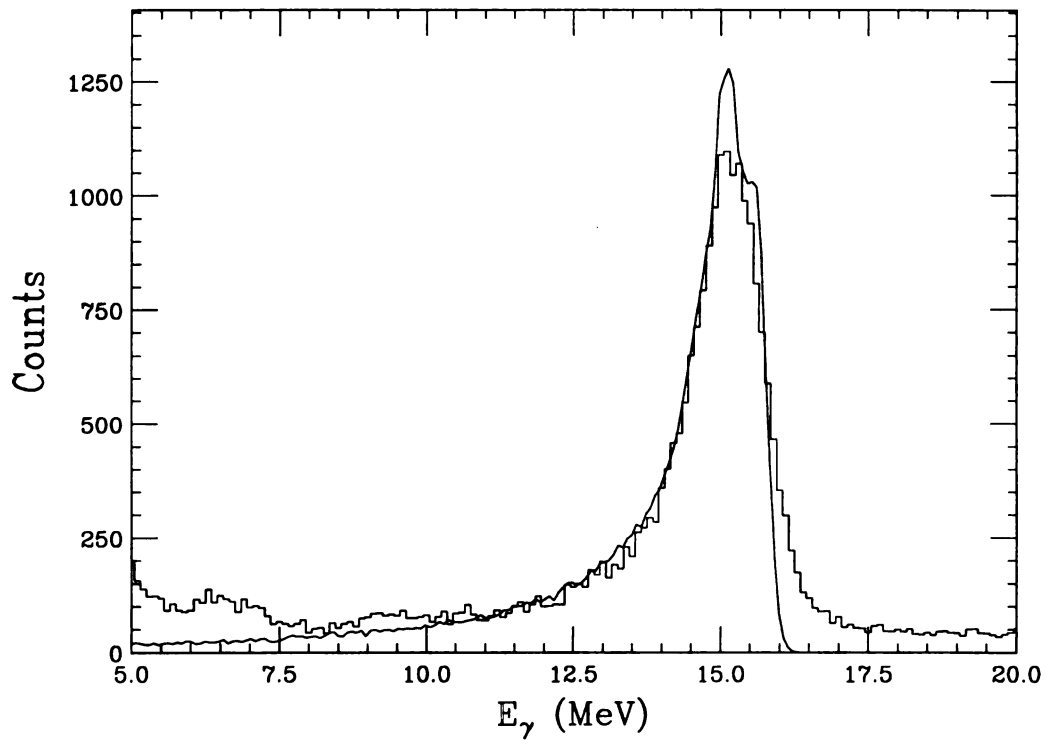
The simulations included the geometry of the pack consisting of 19 detectors. The response function for the pack for  $\gamma$  rays from 100 keV to 25 MeV were calculated in 100 keV steps. The data from the simulations were compiled in a 250x250 matrix. It is rather difficult to uniquely unfold the response of the detector from the measured  $\gamma$ -ray spectrum. Instead, the results of the model calculations were folded with the response matrix before comparing them with the measured spectra. The intrinsic efficiency of the detectors was included in the response matrix. The intrinsic efficiency of the detector pack geometry was  $\sim 60\%$  at 15 MeV.

Figure 4.5 compares the  $\gamma$ -ray spectrum seen in a single BaF<sub>2</sub> detector to the simulation performed with GEANT. The histogram in the figure is the energy spectrum measured from the decay of the 15.11 MeV state in <sup>12</sup>C excited by inelastic  $\alpha$  scattering. The solid line is the simulation in which the geometry of the single detector and the trigger threshold were included.

In the experimental setup the five detector packs were each placed at a distance of  $\sim 40$  cm from the target. The geometric efficiency of the packs was thus  $\sim 17\%$  of  $4\pi$ .

### 4.3.5 $\gamma$ -ray Spectra for Different Target Excitations

In order to obtain coincidence  $\gamma$ -ray spectra as a function of target excitation energy, the data was scanned and a two dimensional histogram of the  $\gamma$ -ray energy versus the  $\alpha$  energy for coincidence events was created. The  $\alpha$ -particle energies were grouped



**Figure 4.5:** The response a BaF<sub>2</sub> detector to 15.11 MeV  $\gamma$ -rays. The histogram is the energy spectrum seen in a single BaF<sub>2</sub> detector from the decay of the 15.11 MeV state in <sup>12</sup>C excited by inelastic  $\alpha$  scattering. The solid line is the response calculated using the monte carlo code GEANT. The simulation took into account the crystal geometry, the efficiency and the trigger threshold.

in bins of 10 MeV each by applying gates on the two dimensional histograms. For each  $\alpha$  energy bin, the corresponding  $\gamma$ -ray spectrum was projected from the two dimensional plot.

The top panel of Figure 4.6 shows the two dimensional plot for coincidence events with a prompt time gate on the  $\gamma$ -ray detectors. The bottom panel shows the projection on the  $\gamma$ -ray energy axis for an  $\alpha$  energy cut of 91 MeV to 100 MeV. Since the beam energy was 160 MeV this  $\alpha$  energy cut corresponds to a target excitation range of 60–69 MeV.

### 4.3.6 Background Subtraction

Random subtraction for the data was performed as follows. The data was scanned twice, once with the condition that the  $\gamma$ -ray event fell within the prompt time gate and then with the condition that the event fell in the random time gate. The  $\gamma$ -ray spectra were extracted as a function of the target excitation energy for both scans. The random time gated data was then subtracted from the prompt time gated data to yield the final random corrected  $\gamma$ -ray spectra for the different excitation cuts. Figure 4.7 shows the comparison of  $\gamma$ -ray spectra from the real and random time cuts for a typical target excitation range of 50–59 MeV.

The peak position for the interaction of cosmic muons in the detectors was around 40 MeV. No significant counts were seen in the  $\gamma$ -ray spectra in this energy region.

At the higher energy end of the  $\gamma$ -ray spectrum there could be contributions from nuclear bremsstrahlung. The bremsstrahlung process produces a  $\gamma$ -ray spectrum of the form  $\exp(-E_\gamma/E_0)$ . The slope parameter  $E_0$  is dependent on the beam energy. From systematics of bremsstrahlung  $\gamma$ -ray spectra studied at various beam energies, the slope parameter  $E_0$  for the current beam energy of 40 MeV/nucleon is  $\sim 14$  MeV

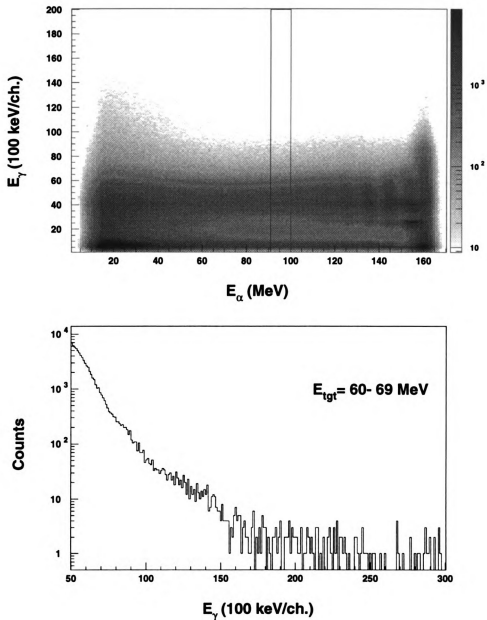


Figure 4.6: Top panel shows a two dimensional plot of the total  $\gamma$ -ray energy in the BaF<sub>2</sub> detectors versus the  $\alpha$  energy in the WALL array, for coincidence events with the prompt time gate. The bottom panel shows the projection of the two-dimensional plot on the  $\gamma$ -ray energy axis for an  $\alpha$  energy range of 91–100 MeV. The corresponding target excitation is 60–69 MeV.

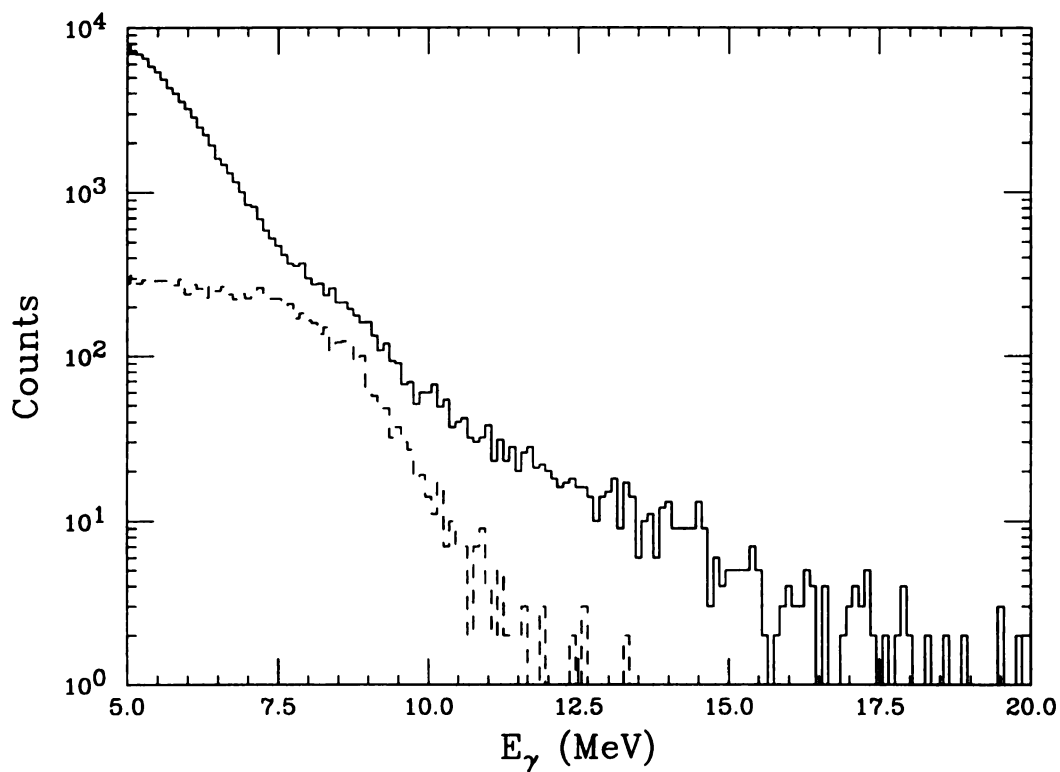


Figure 4.7: Comparison of  $\gamma$ -ray contributions from real (solid) and random (dashed) time gates. The spectra show here are for a target excitation energy range of 50–59 MeV. The random contribution was subtracted from the spectrum for the real time gate to yield random corrected spectra for the different target excitation energy cuts.

[Nif90]. Figure 4.8 shows the measured  $\gamma$ -ray spectrum for a target excitation range of 70–79 MeV. A bremsstrahlung spectrum calculation with a slope parameter of 14 MeV is shown as a solid line. The calculation was normalized to the data points in the range of 20–30 MeV. This normalization range was applied to spectra from all excitation energy ranges. Rather than subtracting the contribution of bremsstrahlung from the measured spectra they were added to the statistical model calculations.

### 4.3.7 Absolute Normalization

The initial population for the statistical model calculations were derived from the particle singles spectra. For each 10 MeV wide target excitation cut the singles counts in all the WALL detectors for the corresponding  $\alpha$  energy range were extracted. The number of  $\alpha$  singles events in each 1 MeV bin from this range was spread over a range of angular momenta. The angular momentum range was computed taking into account the energy loss of the outgoing  $\alpha$ -particle.

The  $\gamma$ -ray spectra from statistical calculations performed with the input populations derived from the singles cross section should match the measured  $\gamma$ -ray spectra. Any excess measured yield is then due to background processes like pickup-decay and nucleon knockout. The contribution from these processes can at best be estimated since not all detection angles were covered and since neutrons were not detected in the DWARF array.

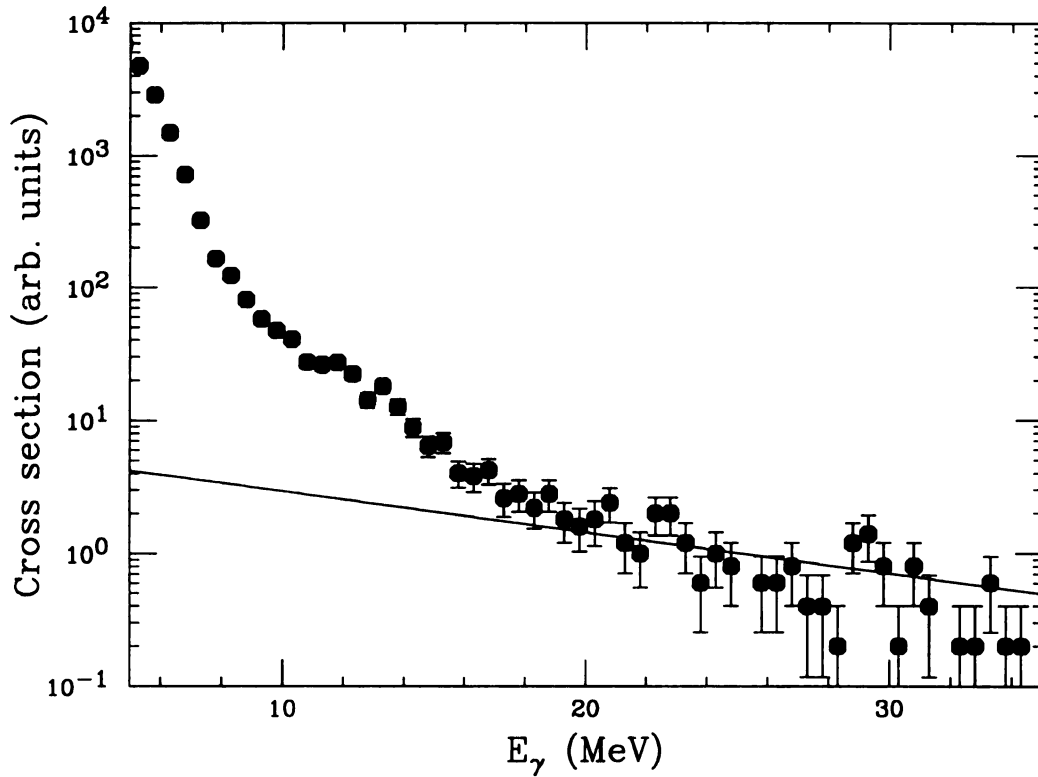


Figure 4.8: The  $\gamma$ -ray spectrum for a typical target excitation energy range of 70–79 MeV is shown as filled circles. The nuclear bremsstrahlung contribution was assumed to have an exponential form with a slope parameter of 14 MeV as explained in text. The solid line in the figure shows this exponential form normalized to the data in the energy range of 20–30 MeV.



# Chapter 5

## Modifications to the Standard CASCADE Code

### 5.1 Level Density Parametrization

The nucleus, being a many body system, can experience many different configurations even for small amounts of excitation energy. The level density in nuclei thus increases rapidly with excitation energy. Statistical model calculations are therefore appropriate and necessary to study the decay of excited nuclei [Sto85].

For low excitation energies information on nuclear level densities is available from experimentally measured energy levels and from neutron resonance data. These measured level densities near the nuclear ground state show extreme sensitivity to properties like pairing, vicinity to closed shell and nuclear deformation. At higher excitation energies there is hardly any direct experimental knowledge of level densities in nuclei. Effects like pairing and shell closure are expected to vanish with increasing excitation. A liquid drop description of the nucleus becomes appropriate as excitation energy increases. The validity of a statistical model thus depends on how well the known level densities at lower excitation energies are described and how good the extrapolation to regions of high excitation and angular momentum are.

The statistical model calculations in the analysis were performed with the code

CASCADE. The modifications made to the standard version of the code are described here.

The level density parametrization in the standard version was modified to correctly describe the level densities in nuclei near closed shells. The input section of the code was modified to accept a population distribution spread over a range of target excitation energy and angular momenta.

In the statistical model code CASCADE the level density as a function of excitation energy  $E$  and angular momentum  $I$  is given by

$$\rho(E, I) = \frac{2I + 1}{12\theta^{3/2}} \sqrt{a} \frac{\exp(2\sqrt{aU})}{(U + T)^2}, \quad (5.1)$$

where

$$U = E - \Delta - I(I + 1)/\theta' = aT^2 - T, \quad (5.2)$$

$$\theta' = \theta(1 + \delta I^2 + \delta' I^4), \quad (5.3)$$

and

$$\theta = 2J_{rigid}/\hbar^2. \quad (5.4)$$

Here,  $E$  and  $I$  are the excitation energy and angular momentum of the nucleus, and  $T$  is the nuclear temperature. The quantity  $U$  is the effective excitation energy of the nucleus which is obtained by subtracting the rotational energy from  $E$ .  $J_{rigid}$  is the rigid-body moment of inertia and  $\theta'$  is the moment of inertia of a deformable rotating liquid drop with deformation coefficients  $\delta$  and  $\delta'$ . The parameters  $a$  and  $\Delta$  are fixed for the individual nuclei.

For low excitation energies below a cutoff value, CASCADE derives these parameters from a fit to the values from Dilg *et al.* [Dil73]. Figure 5.1 shows the level density parameter  $a$  as a function of mass number over a wide range of nuclear masses. The open circles in the figure are from Dilg *et al.* who performed an empirical fit to the

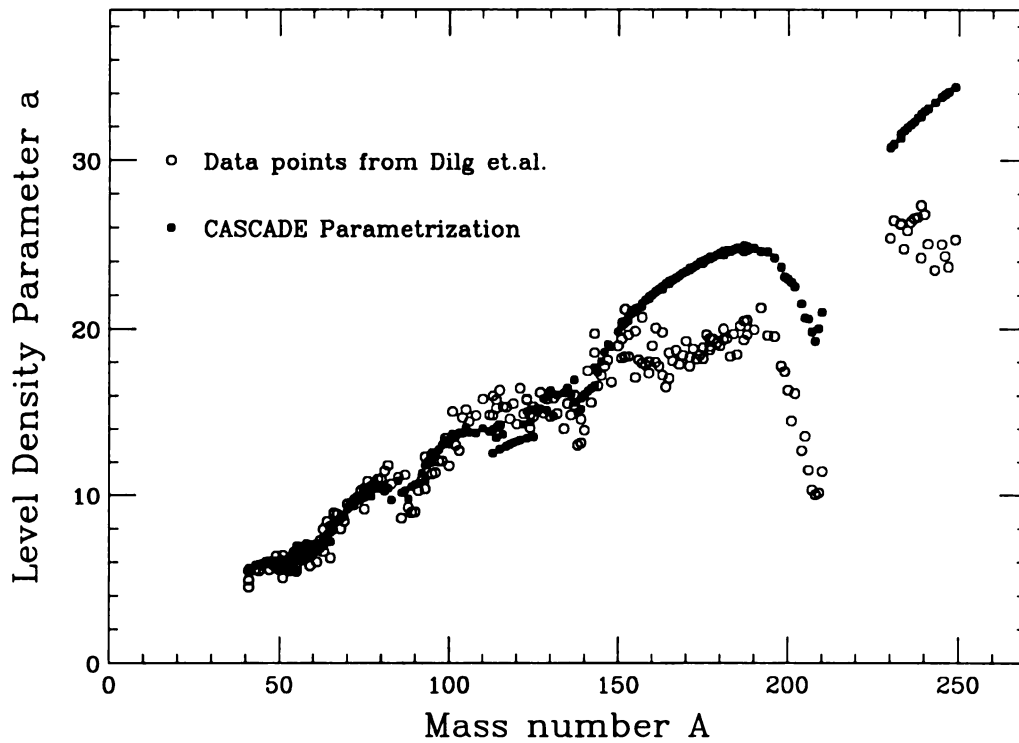


Figure 5.1: Level density parameter  $a$  as a function of mass number  $A$  at low excitation energies. The open circles are data from Dilg *et al.* and the closed diamonds are a parametrized fit to these points used in standard CASCADE calculations. The discrepancies near closed shells, particularly near  $A = 208$ , is clearly seen.

low energy level and neutron resonance data from nuclei over a wide mass range. The filled diamonds are a result of the parameterization used in the standard CASCADE code. It is obvious that though the CASCADE parameterization reproduces the general trend in the level density parameter over the mass range, the values are very different for mass numbers near the doubly magic nucleus  $^{208}\text{Pb}$ . This is not surprising since the CASCADE code was written initially for the lower mass region.

At excitation energies above a cutoff value specified in the input file, the CASCADE code uses a liquid drop description of the nucleus. The parameters  $a$  and  $\Delta$  are assumed to have a smooth mass dependence. The level density parameter in the liquid drop model is given by

$$a = A/da, \quad (5.5)$$

where  $A$  is the mass number and  $da$  is a fixed value over all mass ranges.

The parameter  $\Delta$  is assumed to be the difference between the experimental and liquid drop binding energies of the nucleus, without taking into account pairing or shell effects.

The level density parameter for intermediate energies that fall between the two cutoff values is obtained by interpolation. This approach could lead to a level density description which is not smooth over the range of excitation energies considered. Figure 5.2 shows a typical plot of the level density in  $^{208}\text{Pb}$  nucleus as a function of excitation energy and angular momentum calculated using the standard CASCADE level density parametrization. The lower and upper cutoff energies were 20 MeV and 30 MeV respectively. The non-uniformity in the level density is clearly seen.

To achieve a smooth description of the level density parameters over the entire range of excitation energies involved, another semi-empirical level density formula developed independently by Reisdorf, Schmidt *et al.* and Kataria *et al.* was imple-

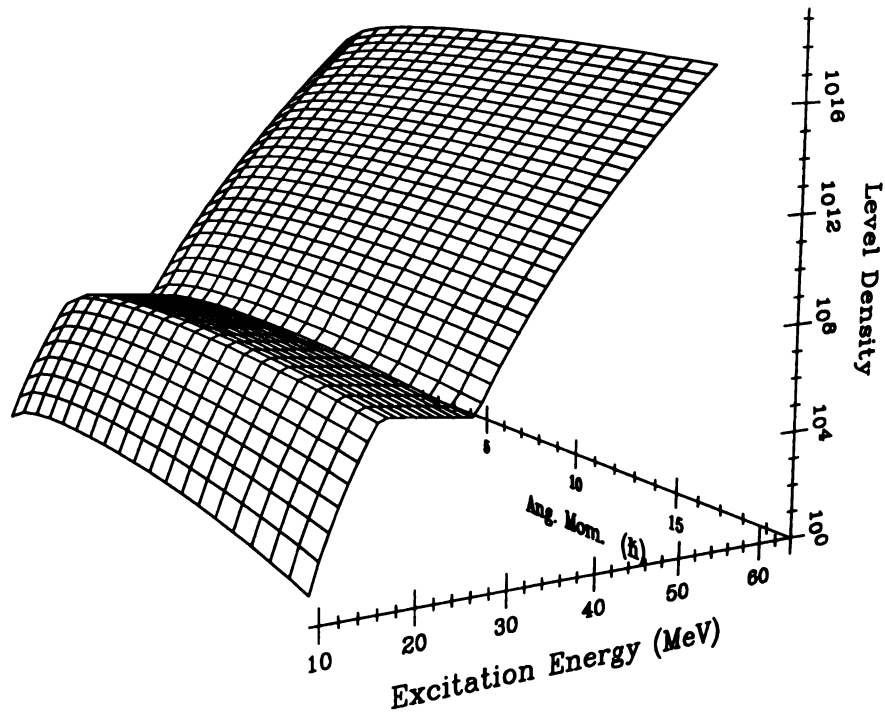


**Figure 5.2:** Level density surface in  $^{208}\text{Pb}$  calculated as a function of excitation energy and angular momentum using standard CASCADE parametrization. The interpolation region, as explained in text, was 20–30 MeV. The discontinuity in the surface is apparent.

mented [Kat78, Rei81, Sch82, Kic87]. In this description the level density parameter  $a$  depends on the ground-state shell correction energy  $\delta U$  and the excitation energy of the nucleus. For a given excitation energy  $E$  and angular momentum  $I$  and for both parities, the level density formula is given by

$$\rho(E, I) = \frac{2I + 1}{12\theta^{3/2}} \sqrt{a} \frac{\exp(2\sqrt{aU})}{U^2}, \quad (5.6)$$

where the effective excitation energy  $U$  is

$$U = E - I(I + 1)/\theta' + \delta P, \quad (5.7)$$

and

$$\theta = 2J_{rigid}/\hbar^2. \quad (5.8)$$

The energy dependence of parameter  $a$  is define by

$$aU = \tilde{a} [E - I(I + 1)/\theta + \delta U + \delta P] - \tilde{a} \delta U \exp(-\gamma U). \quad (5.9)$$

Using the expression for  $U$  from equation 5.7, the above equation becomes

$$a = \tilde{a} \left[ 1 + \frac{\delta U}{U} (1 - \exp(-\gamma U)) \right]. \quad (5.10)$$

The quantity  $\tilde{a}$  is defined as

$$\tilde{a} = A/da'. \quad (5.11)$$

where the value of  $da'$  is fixed so as to reproduce the known level densities in  $^{208}\text{Pb}$  at low excitation energies.

The quantity  $\delta P$  is the pairing correction for the ground state masses. An odd-mass reference system is used, which is consistent with the Myer's droplet model for mass calculation in the CASCADE code.

Thus,  $\delta P$  is given by

$$\delta P = -p A^{1/2} \text{ for even-even nuclei,} \quad (5.12)$$

$$\begin{aligned}
&= +p A^{1/2} \text{ for odd-odd nuclei,} \\
&= 0 \text{ for odd-mass nuclei.}
\end{aligned}$$

where  $A$  is the nuclear mass.

At higher excitation energies the shell and pairing effects are cancelled by the term  $\delta U + \delta P$  in equation 5.9. This is similar to the  $-\Delta$  term in the Pühlhofer description used in standard CASCADE. The dependence of the level density parameter on shell effects is introduced by the additional energy backshift term  $[\tilde{a} \delta U \exp(-\gamma U)]$  in equation 5.9. This term decreases exponentially with excitation energy  $U$ , thus yielding a smooth description of the level density over the entire range under consideration. The quantities  $\gamma$  and  $p$  were varied to obtain the best fit to the measured  $\gamma$ -ray spectra. The parametrization was also checked by comparing the calculated level densities with known values in nuclei near the closed shell.

Figure 5.3 shows the parameter  $da = A/a$  as a function of excitation energy for nuclei from  $^{208}\text{Pb}$  to  $^{198}\text{Pb}$  calculated using the Reisdorf parametrization. The effect of shell closure at low excitations is evident near  $^{208}\text{Pb}$ . At higher excitations, the parameter  $da$  approaches the liquid drop value of  $\sim 9$  which is consistent with systematics for nuclei in this mass range. The overall normalization for the damping was fixed by choosing the value of  $da$  to be 20.76 at the excitation energy of  $U=1$  MeV for  $^{208}\text{Pb}$  [Dil73].

Figure 5.4 shows the level density in  $^{208}\text{Pb}$  as a function of excitation and spin, calculated with the new parameterization. The level density surface is smooth over the entire excitation energy. Thus this description was used for the analysis.

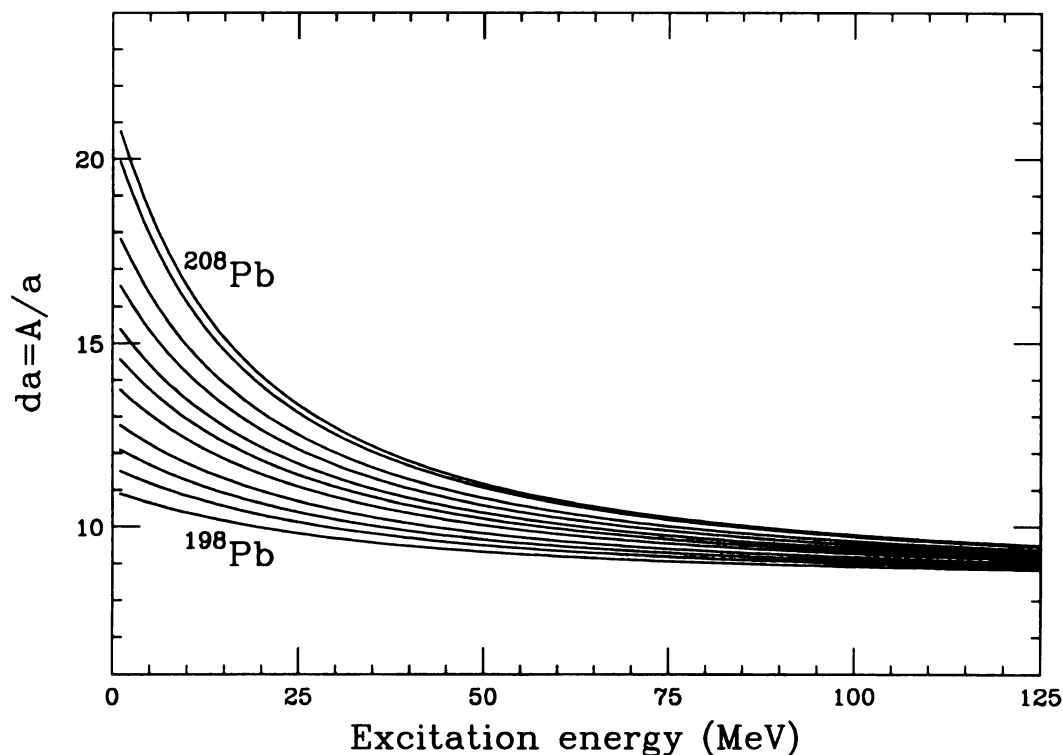


Figure 5.3:  $da$  parameter as a function of excitation energy calculated using Reisdorf parametrization for isotopes of  $Pb$  from  $^{208}\text{Pb}$  to  $^{198}\text{Pb}$ . The parameter varies smoothly as a function of excitation energy for all the nuclei. The influence of shell effects near the closed shell of  $^{208}\text{Pb}$  is clearly seen. The shell effects damp out as excitation energy increases. Also the shell effects vanish for nuclei farther away from the closed shell. The value of the  $da$  parameter converges to  $\sim 9$  at high excitation energies and in nuclei away from the closed shell. This value is consistent with systematics for nuclei in this mass range.



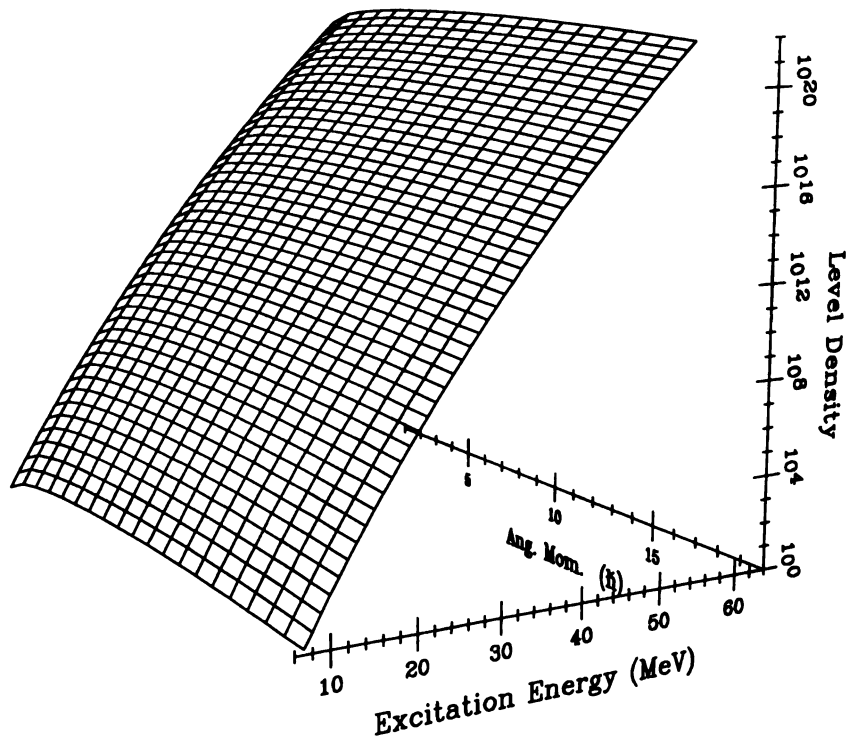


Figure 5.4: Level density as a function of excitation energy and angular momentum calculated using Reisdorf parametrization. The level density surface is smooth over the entire range of excitation and spin.

## 5.2 Input Population for Statistical Calculations

The input section of CASCADE was modified to incorporate the initial population distribution of the compound nuclei.

The population files were derived from the particle singles spectra. The singles spectra from the four rings of the WALL array were first summed together and then divided into '10 MeV wide' bins corresponding to target excitation energy ranges of 40-49 MeV, 50-59 MeV, 60-69 MeV and so on as shown in figure 5.5.

In a given bin the number of nuclei for each MeV step was taken and distributed uniformly over an angular momentum range. The upper limit of the angular momentum was calculated using the sum of the 'matter half density radii' of the target and projectile nuclei as the impact parameter. The lower limit was computed using the 'nuclear interaction radius' as the impact parameter. The interaction radius is defined as [Wil80]

$$R_{int} = C_T + C_P + 4.49 - \frac{C_T + C_P}{6.35} \quad (5.13)$$

where  $C_T$  and  $C_P$  are the 'matter half density radii' of the target and the projectile nuclei in  $fm$ . For the scattering of  $\alpha$ -particles on  $^{208}\text{Pb}$ , the sum of the 'matter half density radii' is 11.25 fm and the nuclear interaction radius is 8.03 fm. Figure 5.6 shows the geometric calculation of the momentum transferred to the target for specific values of projectile energy loss and impact parameter. Since the exact process of angular momentum transfer in the inelastic scattering is not known, the incoming and outgoing impact parameters were approximated to be equal independent of the scattering angle. The angular momentum transferred to the target is then the difference between the angular momenta in the incoming and outgoing channels. A dependence on the scattering angle should result in a decrease in the momentum transfer with increasing scattering angle. The momentum transfer calculated here is thus an upper

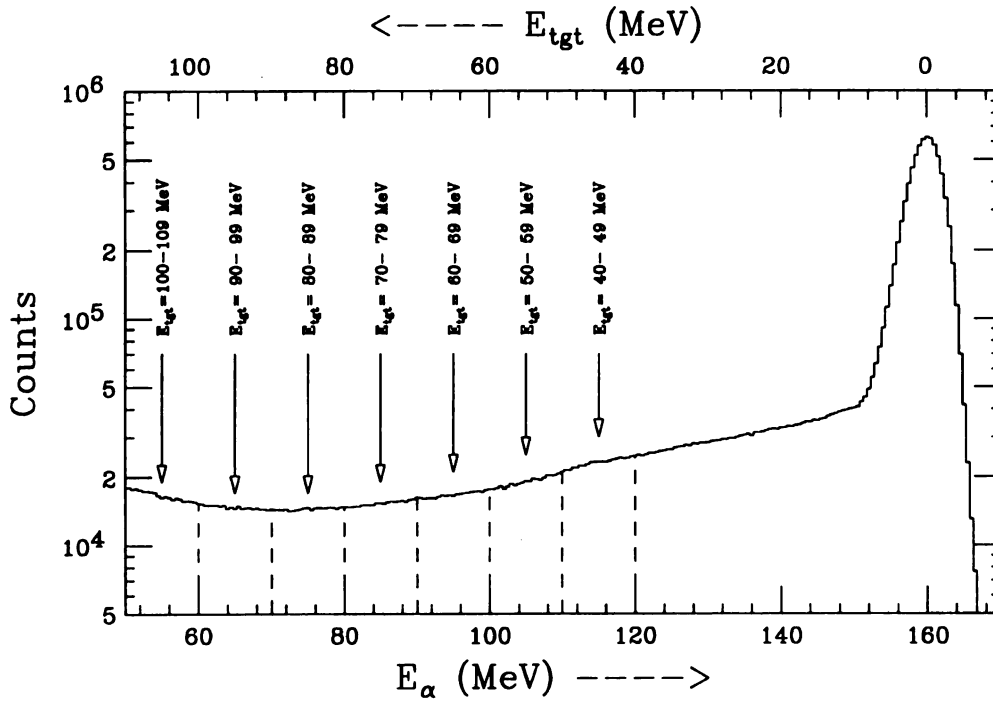
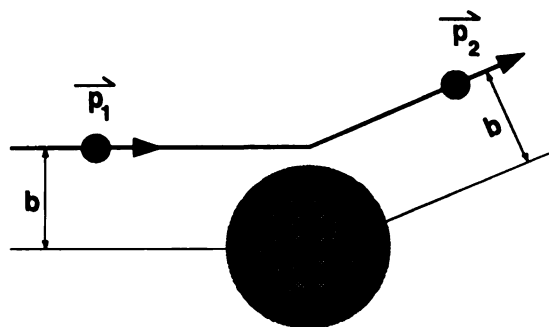


Figure 5.5: The singles spectrum from the WALL array was divided in '10 MeV wide' bins. Shown here is the singles spectrum from ring 1. The dashed lines show the boundaries of the  $\alpha$  energies for different target excitation bins. The corresponding target excitation energy values are also shown.



**Momentum transferred to target**

$$\mathbf{p} = \left| \vec{p}_1 \right| - \left| \vec{p}_2 \right|$$

Figure 5.6: Calculation for angular momentum transferred to the target for a specific projectile energy loss and specific impact parameter. The impact parameter was varied between a lower and upper limit as explained in text.

limit.

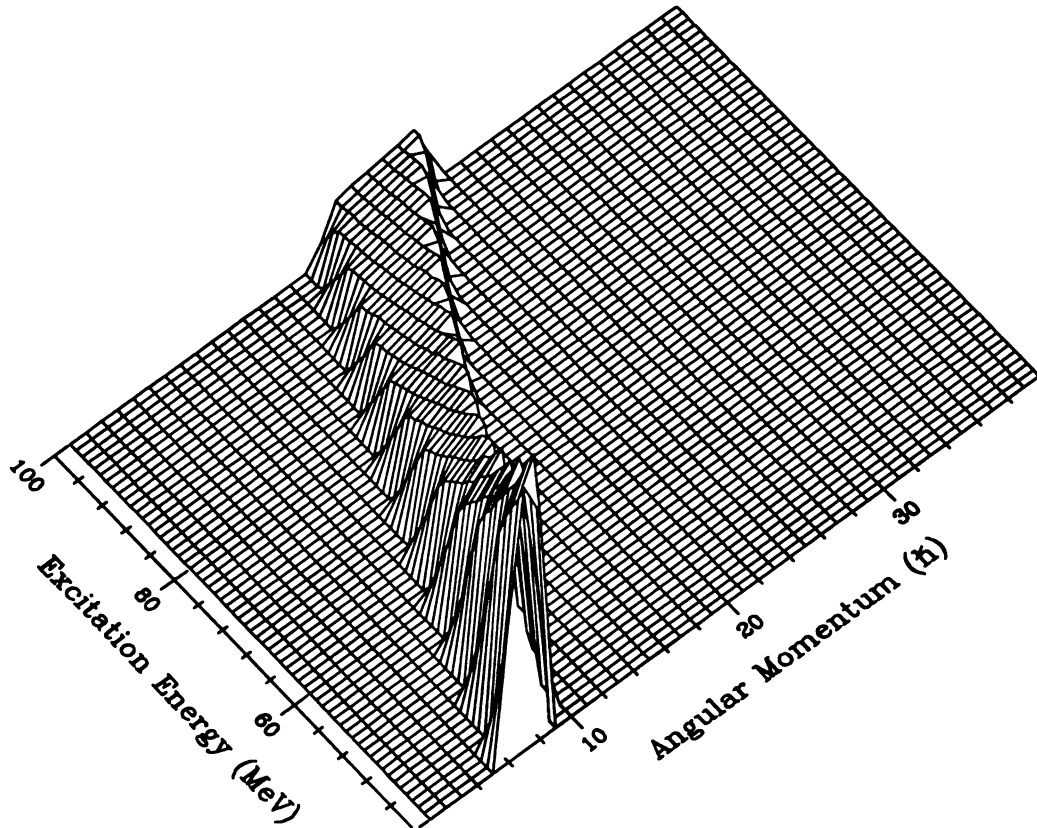
The angular momentum of the target for a momentum transfer  $p$  and impact parameter  $b$  is

$$L = \frac{1}{197} b p \hbar \quad (5.14)$$

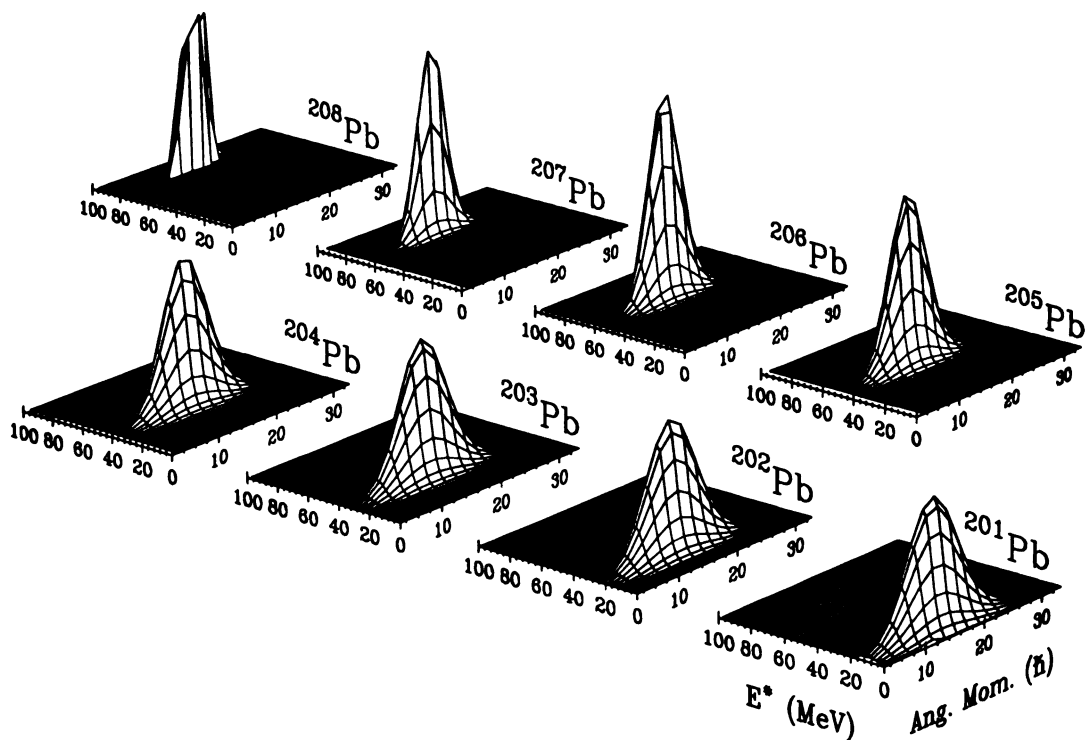
Here,  $p$  is in units of 'MeV/c' and  $b$  is in units of 'fm'.

Figure 5.7 shows the distribution of the calculated angular momentum transfer to the target for excitation energies of 40 to 100 MeV.

Figure 5.8 displays the input population of  $^{208}\text{Pb}$  nuclei for excitation energies in the range of 80-89 MeV spread over the calculated range of angular momenta, and the subsequent populations generated by CASCADE for nuclei in the neutron decay channels.



**Figure 5.7:** Angular momentum transferred to the target in the inelastic scattering process as a function of excitation energy in the target. Details of the calculation are explained in text. The angular momentum transferred is low and does not increase appreciably with increasing excitation energy in the target.



**Figure 5.8:** Initial population of nuclei in neutron decay channels calculated by CASCADE. The starting population in  $^{208}\text{Pb}$  is derived from the singles cross section as explained in text and is fed as input to the code. The subsequent nuclei are populated following neutron evaporation. The populations shown here are for an excitation energy of 80–89 MeV in  $^{208}\text{Pb}$ .

# Chapter 6

## Results and Discussion

### 6.1 Particle Spectra

In this section the singles and coincidence particle spectra are presented. The DWARF array detectors were organized in rings centered at various laboratory angles. To simplify the discussions the rings from the WALL and the BALL array have been numbered. Tables 6.1 and 6.2 list the numbering scheme and the angular information for the rings. Detectors that exhibited non-linearities and large gain shifts were not included in the analysis. The tables reflect the actual number of detectors from which the data sets presented here are derived.

Ring no.	No. of dets.	Lab. angle	Total solid angle
1	6	14.78°	0.1398 sr
2	8	22.39°	0.1848 sr
3	5	23.18°	0.1290 sr
4	10	31.03°	0.2200 sr

**Table 6.1:** Table showing ring numbers, angles and solid angle coverage for the DWARF WALL array.

Ring no.	No. of dets.	Lab. angle
5	5	41.59°
6	8	49.51°
7	5	63.43°
8	5	67.93°
9	9	77.52°
10	5	87.30°
11	4	92.70°
12	5	102.48°
13	5	112.07°
14	5	116.57°
15	5	130.49°
16	5	138.41°
17	4	155.58°

Table 6.2: Table showing ring numbers and angles for detectors in the DWARF BALL array.

### 6.1.1 Singles $\alpha$ Spectra

The  $\alpha$  singles spectra from the four rings of the wall array are displayed in figure 6.1. The elastic scattering peak is seen prominently at the beam energy of 160 MeV at all four angles. At energies below the elastic peak there is a broad continuum from inelastic processes. This continuum decreases rather slowly with decreasing  $\alpha$  energy. At the lower energy end of the  $\alpha$  spectra the cross section increases with decreasing  $\alpha$  energy. This feature is discussed in section 6.4.

At an  $\alpha$  energy of  $\sim 148$  MeV an enhancement is seen in the singles spectra. The corresponding target excitation energy is  $\sim 12$  MeV. This feature is more prominent in the outer rings due to the reduced elastics cross section. The enhancement corresponds to the ground state GQR and GMR excitations in  $^{208}\text{Pb}$  with resonance energies of 10.9 and 13.9 MeV respectively [Ber80]. Since the  $\alpha$ -particle has a  $T=0$  ground state, the GDR built on the ground state of the target is not excited in the scattering process.



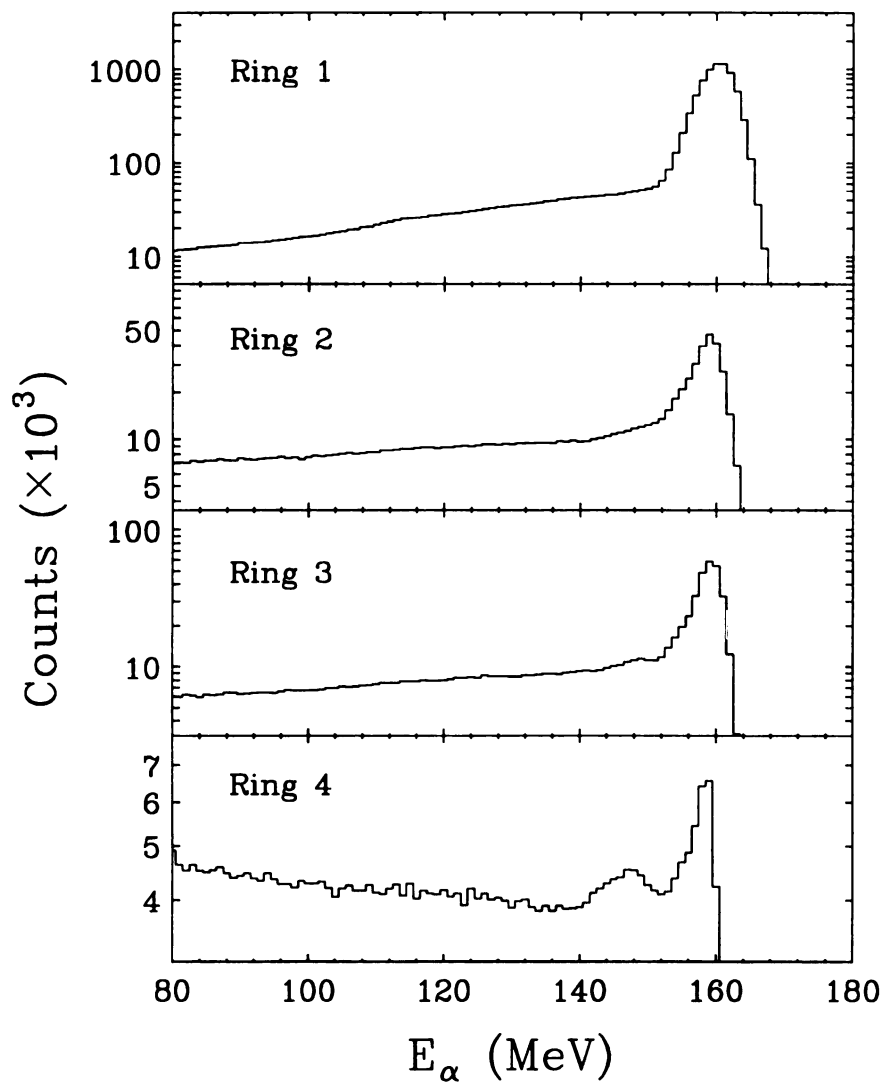


Figure 6.1:  $\alpha$  singles spectra from the four rings of the WALL array.

The absolute cross section for the inelastic scattering was estimated from the elastic scattering cross section. The calculation was performed for ring 1 of the WALL array. First, the area under the elastic scattering peak was estimated from the singles spectrum. This area was compared to the absolute elastics cross section data from scattering measurements of 166 MeV  $\alpha$ -particles on a  $^{208}\text{Pb}$  target [Las82].

The elastics cross section in units of ‘millibarn (mb)’ for ring 1 of the WALL array is thus given by

$$\sigma(\text{Ring 1}) = \frac{2\pi \int_{\theta_1}^{\theta_2} \left( \frac{d\sigma}{d\Omega} \right) \sin \theta d\theta}{2\pi \int_{\theta_1}^{\theta_2} \sin \theta d\theta} \Omega(\text{Ring 1}), \quad (6.1)$$

The integral in the numerator was evaluated numerically after obtaining an exponential fit to the elastic scattering cross section data from [Las82] shown in figure 6.2. Angles between  $9^\circ$  and  $20^\circ$  were integrated, corresponding to the angular coverage of ring 1.  $\Omega(\text{Ring1})$  is the total solid angle covered by detectors of Ring1. The singles spectrum was scaled by the factor

$$S = \frac{\sigma(\text{Ring1})}{N_{\text{elastics}}} \quad (6.2)$$

to yield absolute cross section in units of ‘mb/MeV’.

Here  $N_{\text{elastics}}$  is the total counts under the elastic scattering peak of the singles spectrum from ring 1.

Figure 6.3 shows the absolute cross section derived as explained above. The cross section is comparable to inelastic  $\alpha$  scattering measurements made at similar angles and beam energies on  $^{208}\text{Pb}$  targets [Ber80].

## 6.1.2 Coincidence $\alpha$ Spectra

The coincidence  $\alpha$  spectra were obtained with the condition that a  $\gamma$ -ray of energy greater than  $\sim 4$  MeV was observed in coincidence with the  $\alpha$ -particle. The spectra from the four rings of the WALL array are displayed in figure 6.4.

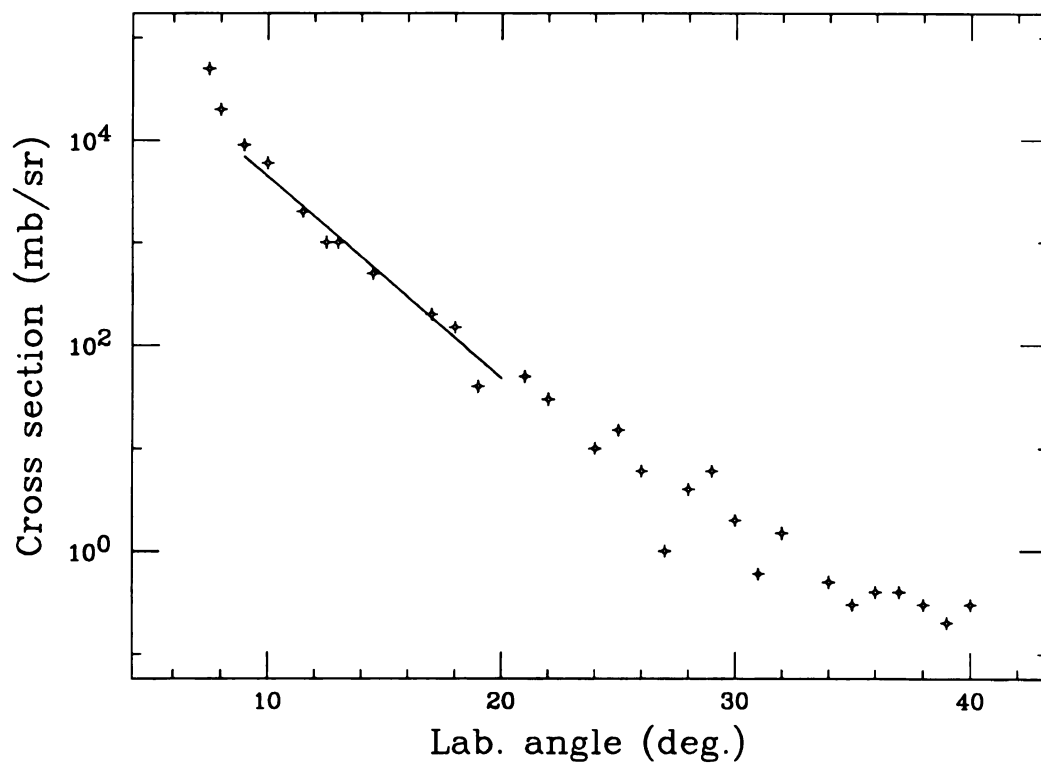


Figure 6.2: Differential cross section for elastic  $\alpha$  scattering on  $^{208}\text{Pb}$  from [Las82] and fit to the data in the angular range covered by ring 1 of the WALL array. This data was used to estimate the cross section for inelastic scattering.

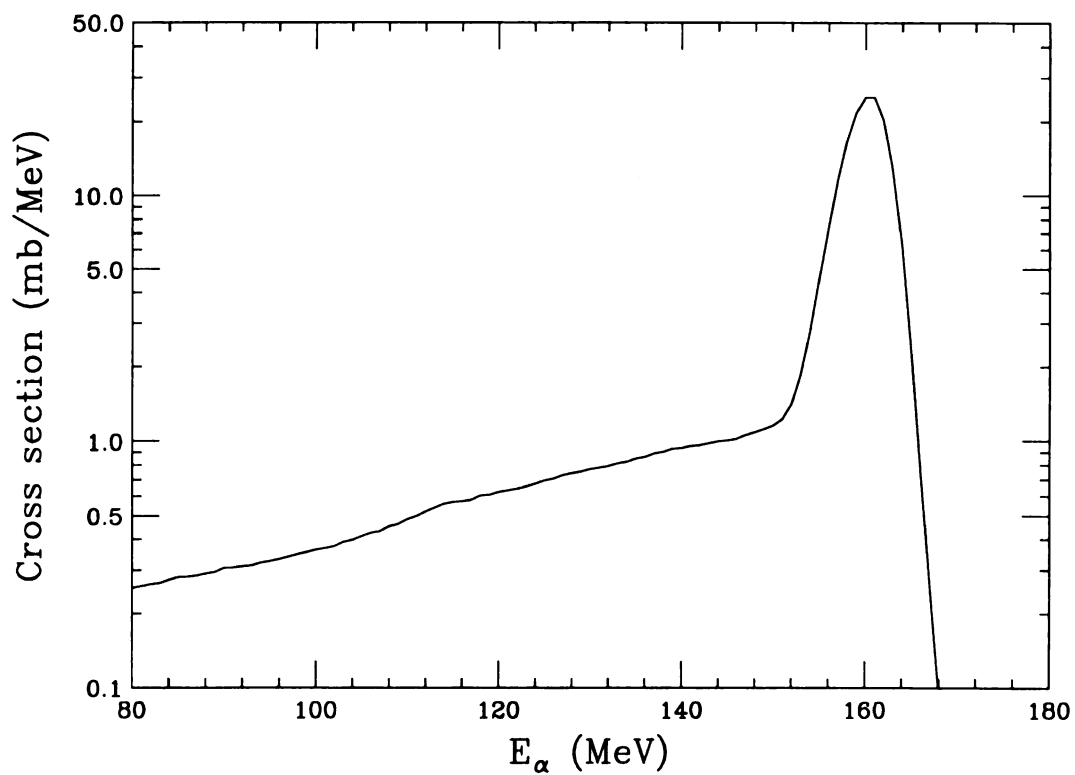


Figure 6.3: Absolute cross section for inelastic scattering of  $\alpha$  on  $^{208}\text{Pb}$ . The cross section was estimated for ring 1 of the WALL array which covers laboratory angles of  $9^\circ$  to  $20^\circ$ .

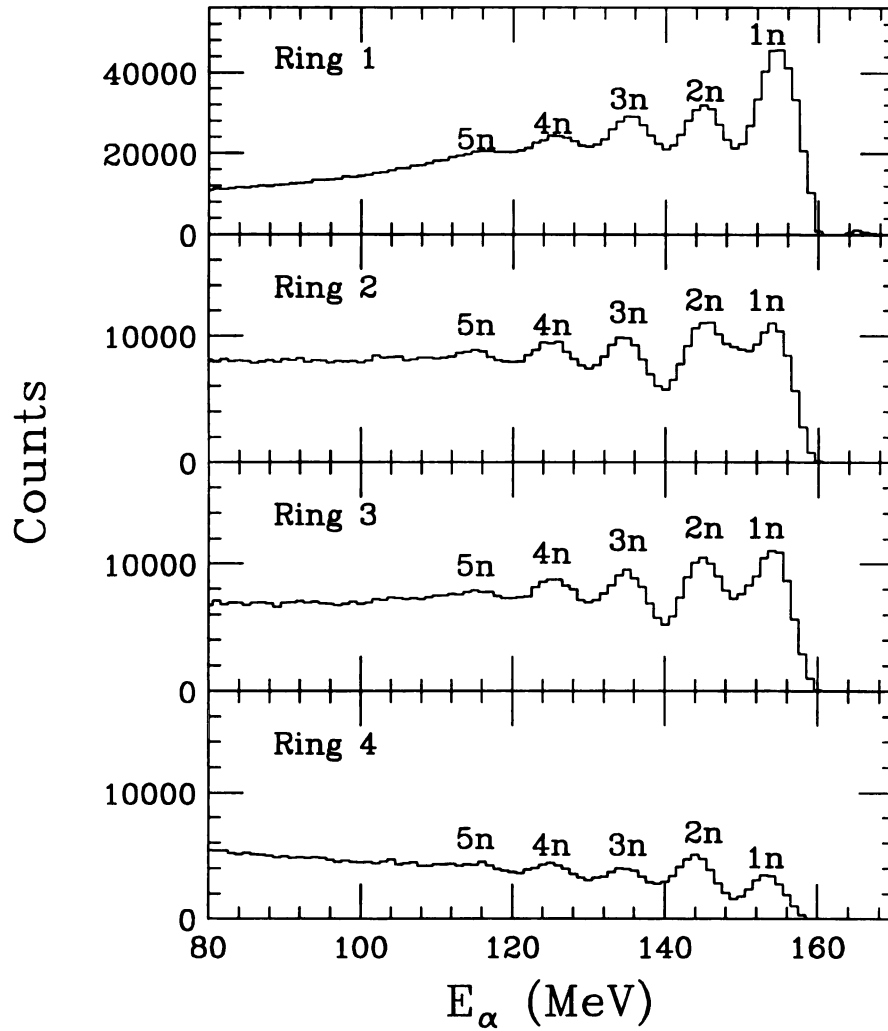


Figure 6.4:  $\alpha$  spectra in the four rings of the WALL array for coincidence events with  $\gamma$ -rays of energy greater than  $\sim 4$  MeV. The structures seen in the coincidence spectra are evidence for equilibrated emission from an excited target nucleus.

The spectra exhibit structures up to  $\alpha$  energies of  $\sim 110$  MeV. These structures arise due to the successive opening of neutron evaporation channels in the decay of the excited target nucleus. When a new neutron channel is available for decay, the probability of  $\gamma$ -ray emission is reduced and therefore the  $\gamma$ -ray multiplicity is reduced. Since the  $\alpha$  spectrum is measured in coincidence with the  $\gamma$  rays, the  $\alpha$ -particle multiplicity also goes down. The structures seen in the coincidence  $\alpha$  spectra are thus strong evidence for equilibrated emission from an excited target nucleus. At higher target excitation energies the increase in the cross section for neutron emission above the individual evaporation thresholds becomes less and less steep and the structures therefore do not show prominently. These structures in the particle spectra have been previously observed in the inelastic excitation measurement of  $^{208}\text{Pb}$  with  $^{17}\text{O}$  projectiles [Tho91].

The probabilities for neutron emission can be computed as a function of target excitation energy. The top panel in figure 6.5 displays this probability calculated using the CASCADE code. The influence of individual neutron evaporation thresholds is clearly seen. The bottom panel of the figure displays the ratio of the coincidence  $\alpha$  spectrum to the single  $\alpha$  spectrum from ring 1 of the WALL array. The dashed lines mark the excitation energies corresponding to the onset of new evaporation channels. The peak positions in the ratio spectrum are in good agreement with the threshold energies for the  $3n$ ,  $4n$  and  $5n$  neutron evaporation channels.

### 6.1.3 Knockout and Pickup-Decay Contributions

Contributions to the particle spectrum other than inelastic scattering could arise from knockout and pickup-decay processes. In knockout processes, the incoming projectile knocks out a proton or a neutron from the target. Pickup-decay processes occur when the incoming  $\alpha$ -particle picks up a proton or a neutron from the target forming  $^5\text{Li}$  or

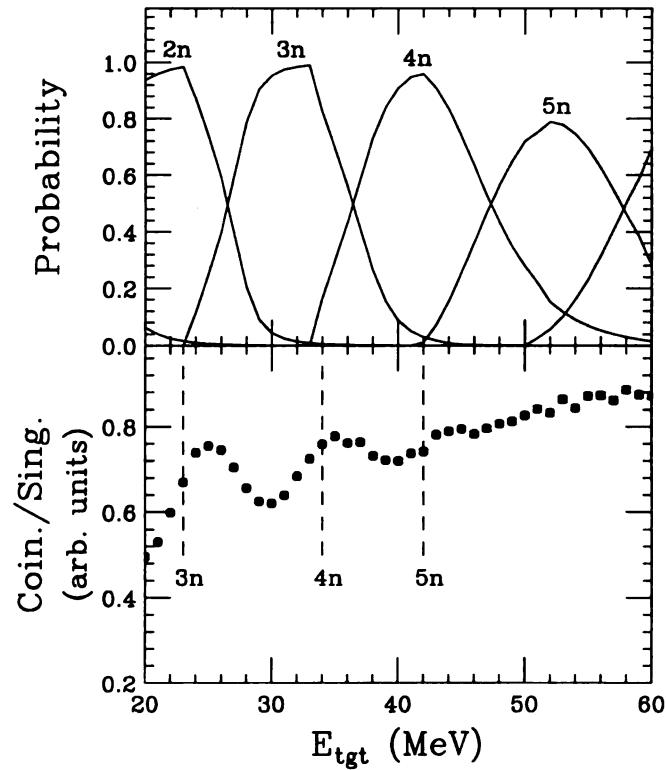


**Figure 6.5:** The neutron emission probability as a function of target excitation energy is compared to the particle coincidence spectrum. The top panel displays the probability for neutron emission computed using the CASCADE code. The probability distribution exhibits the influence of individual neutron evaporation channels. The bottom panel displays the ratio of coincidence to singles  $\alpha$  spectra from ring 1 of the WALL array. The dashed lines mark the energies corresponding to the onset of various neutron evaporation channels.

${}^5\text{He}$ , respectively. The nucleus formed then decays back to a proton or a neutron and the  $\alpha$ -particle. These processes are included in the measured  $\alpha$  singles spectra and thus contribute to the measured cross section. It is therefore important to analyse these processes and to estimate their contribution to the cross section.

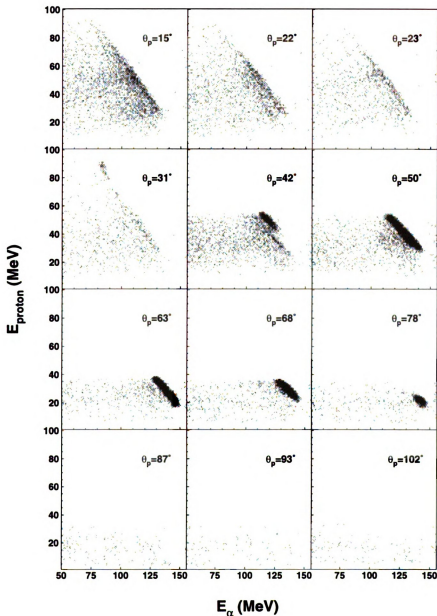
Since neutral particles were not detected in the DWARF array, pickup-decay and knockout processes were studied by analysing events in which an  $\alpha$ -particle and a proton were detected in coincidence. Figure 6.6 displays two dimensional spectra of proton energy versus  $\alpha$  energy for  $\alpha$ -proton coincidence events. The plots correspond to events where the  $\alpha$ -particle was detected in ring 1 of the WALL array and the proton was detected in rings 1 through 12. Events where the  $\alpha$ -particle was detected in the outer rings 2,3, and 4 did not have appreciable statistics.

One prominent feature of the spectra shown in figure 6.6 is that for the higher end of the  $\alpha$  energy spectrum, irrespective of the angles, the counts are predominantly in a region which corresponds to the kinematic limit where the outgoing  $\alpha$  and the proton share all the available energy. These events do not leave the residual target nucleus in excited states and therefore do not contribute to the coincident  $\gamma$ -ray spectra. At the lower  $\alpha$  energy end of the spectra, contributions from pre-equilibrium processes are seen. These are discussed further in section 6.4.

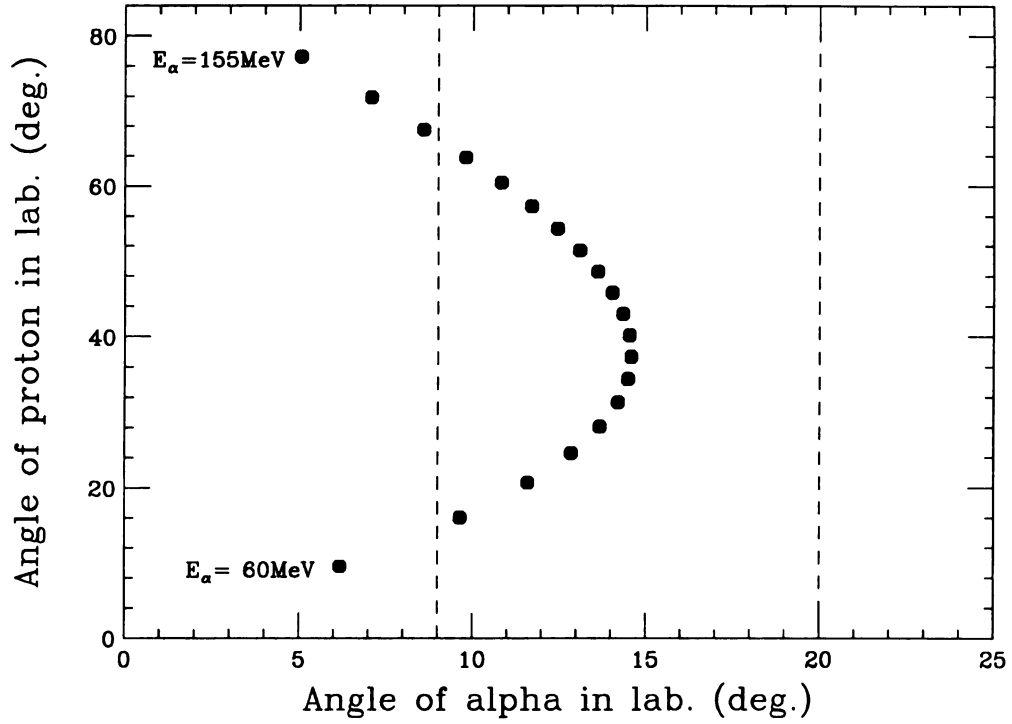
The prominent bands seen in the spectra for protons detected in rings 5 through 9 correspond to knockout events. These events seem to arise as a result of free proton knockout from hydrogen contaminants in the target.

A kinematic calculation was performed to study the process of free proton knockout by the  $\alpha$ -particles of the beam. Results of the calculation are shown in figure 6.8 where the angle of the outgoing proton is plotted against the angle of the outgoing  $\alpha$ -particle for different energies of the outgoing  $\alpha$ -particle.





**Figure 6.6:** Two dimensional plots of proton energy versus  $\alpha$  energy for  $\alpha$ -proton coincidence events in the DWARF array. The plots shown here correspond to events where the  $\alpha$  particle was detected in ring 1 and the proton was detected in rings 1 through 12 of the WALL/BALL array.



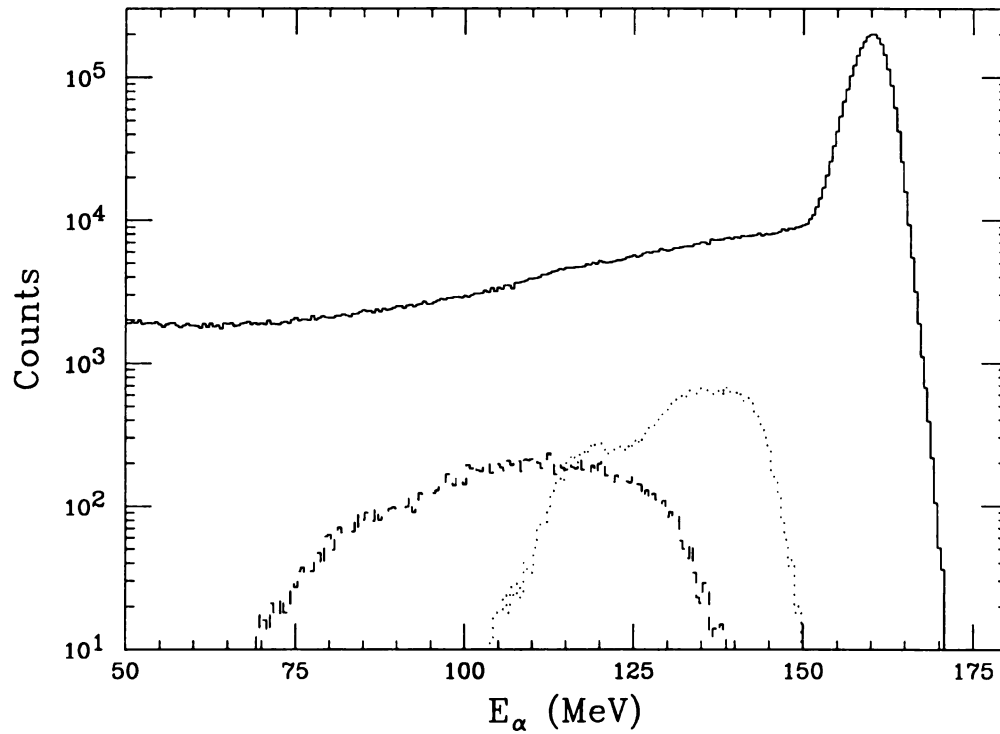
**Figure 6.7:** Results of kinematic calculation for free proton knockout events. The angle of the outgoing proton is plotted against the angle of the outgoing  $\alpha$  for outgoing  $\alpha$  energies of 155 MeV to 60 MeV in steps of 5 MeV. The dashed lines mark the angular acceptance limit of ring 1 of the WALL array.

Figure 6.7 shows that the events in which the  $\alpha$ -particle is detected in ring 1 of the WALL will correspond to protons emerging at angles of  $\sim 16^\circ$  to  $\sim 70^\circ$ . Thus free protons that are knocked out should be observed in the angular range covered by ring 1 through ring 9. The energy of the protons emerging in the angular range covered by rings 1 through 4 is too large ( $E_\alpha \geq 90$  MeV). These protons therefore punch through the detector volume and thus cannot be identified. The above angular dependence is seen in figure 6.6. The knockout band is present from the fifth plot onwards. Further, ring 9 is the last ring in which the knockout band is seen. The data that fall in the knockout bands were also analysed for angular correlation. It was observed that in these events the  $\alpha$  and the proton were measured in detectors that were diametrically opposite to each other in a plane perpendicular to the beam axis. This angular correlation is consistent with the knockout process.

The bands observed in the first four spectra in figure 6.6 where the proton is detected in rings 1 through 4 of the WALL correspond to pickup-decay events. No angular correlation is seen for these events thus ruling out knockout type reactions. Again the counts are dominant at the kinematic limit corresponding to the total energy being shared by the  $\alpha$ -particle and the proton. Contributions to the coincident  $\gamma$ -ray spectra are therefore minimal.

Figure 6.8 displays the knockout and pickup-decay contributions to the  $\alpha$  spectrum from the events around the kinematic limit, in comparison to the  $\alpha$  singles spectrum in ring 1.

The pickup-decay spectrum was obtained by summing events where the  $\alpha$ -particle was detected in ring 1 and the proton was detected in rings 1 through 4. The knockout spectrum corresponds to events where the  $\alpha$  was detected in ring 1 and the proton in rings 5 through 9. From the figure, the knockout contribution can be estimated to be at most  $\sim 8\%$ . The pickup-decay contribution is at most  $\sim 5\%$ . This corresponds



**Figure 6.8:** Pickup-decay and knockout contributions compared to the singles  $\alpha$  spectrum. The solid histogram is singles cross section. The dotted histogram shows contributions from free proton knockout and the dashes histogram shows contribution from proton pickup-decay events.

to events in which the incoming  $\alpha$  picks up a proton. Since events where a neutron is picked up were not detected, the contribution estimated from proton pickup should be scaled to account for neutron pickup. There are about 1.5 times as many neutrons as there are protons in  $^{208}\text{Pb}$ . The total contribution from pickup-decay and knockout can thus be approximated to  $\sim 20\%$ .

## 6.2 Coincidence $\gamma$ -ray Spectra

### 6.2.1 $\gamma$ -ray Spectra as a Function of Target Excitation

In this section the  $\gamma$ -ray spectra measured in coincidence with  $\alpha$ -particles in the WALL array are presented. The data were sorted to create  $\gamma$ -ray spectra as a function of  $\alpha$  energy, ring number of the coincidence WALL detector, and pack number of the  $\text{BaF}_2$  detectors.

To obtain the  $\gamma$ -ray spectra as a function of target excitation, the  $\alpha$  spectra were binned in 10 MeV wide cuts in  $\alpha$  energy as explained earlier in chapter 4.

The  $\gamma$ -ray spectra were measured in  $\text{BaF}_2$  detectors placed at three different measurement angles of  $60^\circ$ ,  $72^\circ$  and  $112^\circ$  in the laboratory. The left panel in figure 6.9 displays the  $\gamma$ -ray spectra for detection angles of  $60^\circ$  and  $112^\circ$  for a target excitation energy range of 80–100 MeV. There is no appreciable difference in the spectra from the two angles.

The  $\gamma$ -ray spectra as a function of the  $\alpha$  detection angle are displayed in the right panel of figure 6.9, for the same target excitation energy. Again the spectra exhibit no shape differences.

Since no appreciable angular dependence was seen in the spectra as a function of  $\gamma$ -ray detection angle or as a function of  $\alpha$  detection angle, the data from the different detection angles were summed together to yield the final  $\gamma$ -ray spectra.

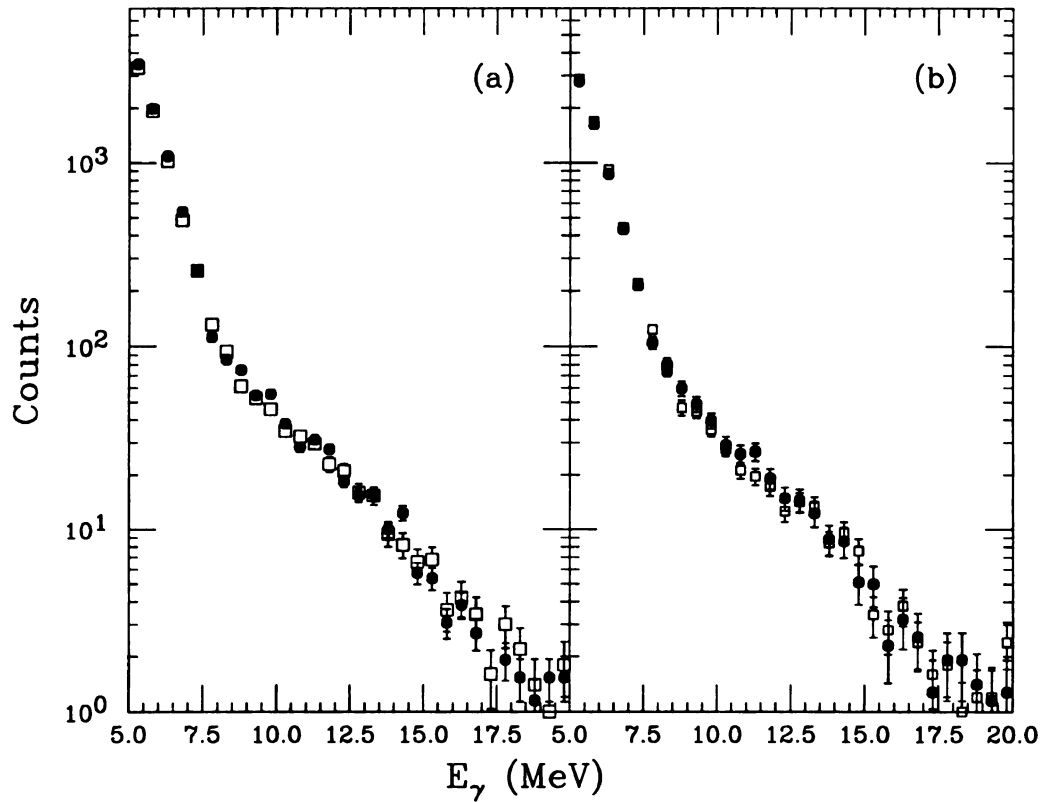


Figure 6.9:  $\gamma$ -ray spectra corresponding to different  $\gamma$ -ray and  $\alpha$  particle detection angles for a target excitation energy range of 80–100 MeV. (a) The open squares are the spectra from the two  $\text{BaF}_2$  packs at laboratory angle of  $60^\circ$  and the closed circles are data from the pack at detection angle of  $112^\circ$ . The spectra were normalized in the range of 7–10 MeV. (b) The open squares are spectra in coincidence with  $\alpha$  particles detected in ring 1 of the WALL array and the closed circles are spectra in coincidence with rings 2 and 3. The spectra were normalized in the range of 7–10 MeV.

Figure 6.10 shows the  $\gamma$ -ray spectra for  $\alpha$  energy ranges of 111–120 MeV and 61–70 MeV. These correspond to target excitation energies of 40–49 MeV and 90–99 MeV respectively. The enhancement in the giant dipole resonance energy region is clearly seen in both spectra. Furthermore the spectrum from the higher excitation energy range has significantly more counts in the GDR region compared to that from the lower excitation cut. This is a clear evidence for increase in target excitation with increase in the energy loss of the projectile.

Figure 6.11 shows the  $\gamma$ -ray spectra for various target excitation energy ranges corresponding to  $\alpha$  energies from 111 MeV to 61 MeV. Below an  $\alpha$  energy of  $\sim 50$  MeV, the singles cross section rises significantly with energy loss. The target excitation in this region can be influenced by pre-equilibrium type processes.

### 6.2.2 Statistical Model Calculations with CASCADE

The  $\gamma$ -ray spectra were compared to statistical model calculations performed with the modified version of the CASCADE code.

The contribution to the total  $\gamma$ -ray spectrum for all excitation ranges arises predominantly from the neutron channels in the decay of the excited target nucleus. Figure 6.12 shows the calculated spectra for target excitation energy range of 80–89 MeV. The open circles represent the total calculated  $\gamma$ -ray spectrum. The filled diamonds are the contribution from neutron evaporation in  $Z = 82$  isotopes. It can be seen from the figure that the contribution from the neutron channels accounts for almost all of the cross section. The summed contributions from other decay channels are shown as open diamonds in the figure. This contribution is at least 2 to 3 orders of magnitude smaller.

The dominant contribution to the  $\gamma$ -ray spectrum in the GDR energy range results

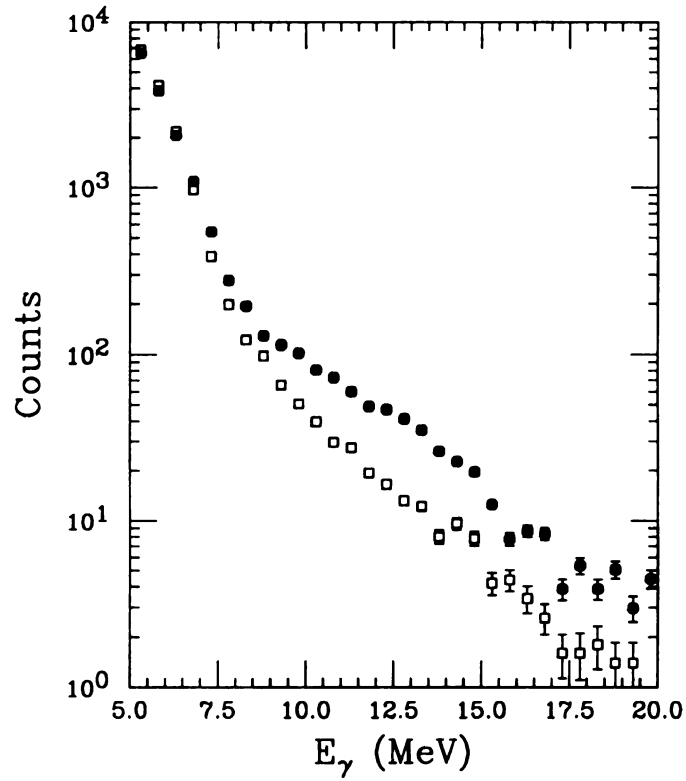


Figure 6.10:  $\gamma$ -ray spectra from two different target excitation cuts of 40–49 MeV (open squares) and 90–99 MeV (filled circles). Data have been normalized in the range of 6–7 MeV. Figure shows the enhancement of counts in the GDR energy region in the spectrum from the higher excitation energy over the spectrum from the lower excitation energy.



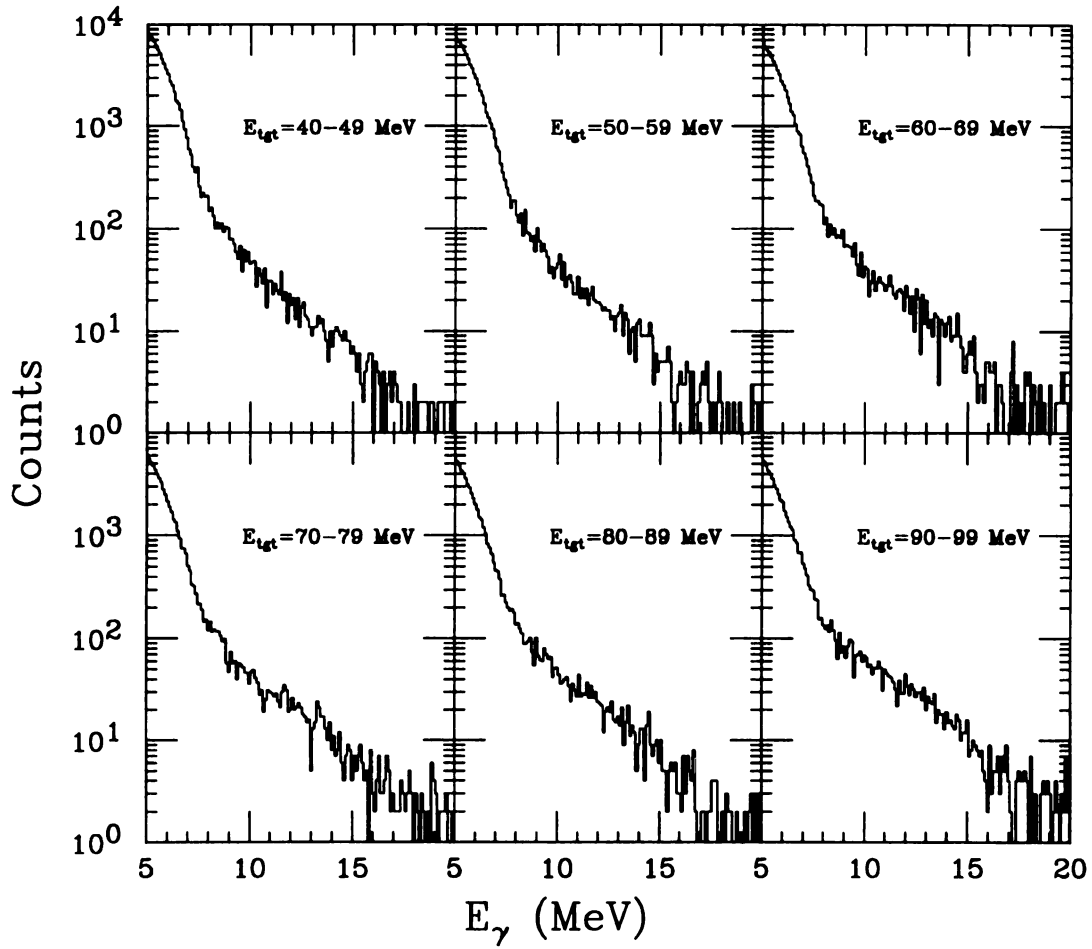


Figure 6.11: Coincidence  $\gamma$ -ray spectra for various target excitation energies from 40–49 MeV to 90–99 MeV.

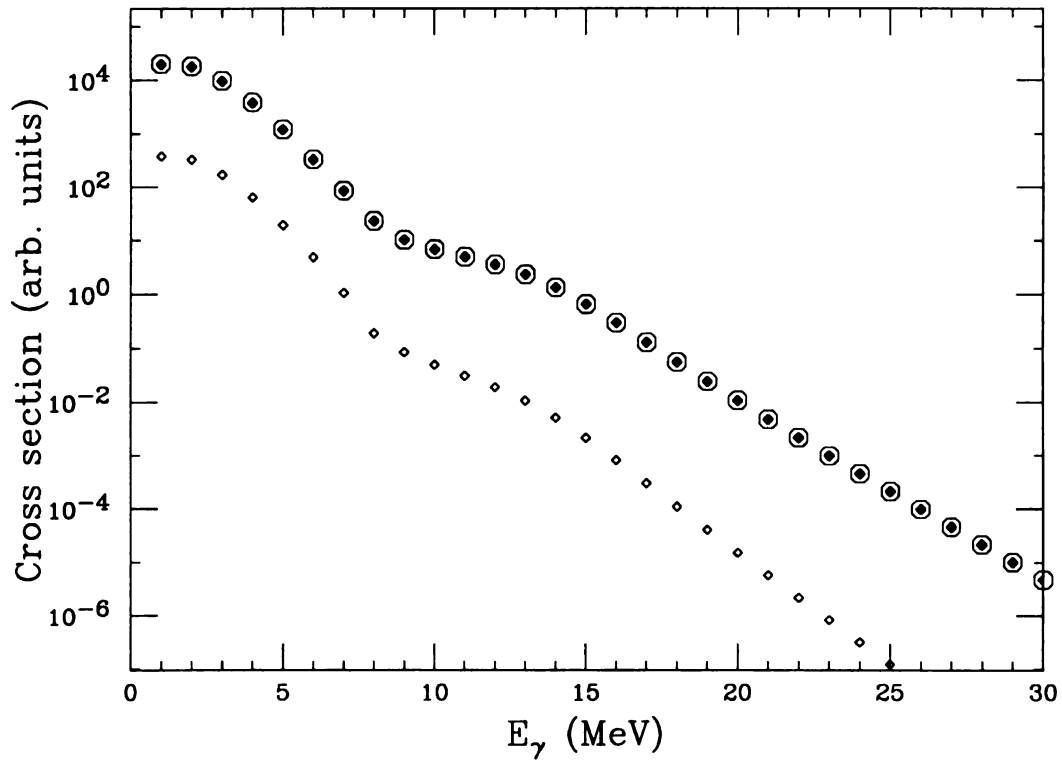


Figure 6.12: Contributions to the  $\gamma$ -ray spectra from neutron evaporation channels compared to contribution from other channels for a typical target excitation range of 80-89 MeV. The open circles are the contribution from all channels. The closed diamonds are the sum contribution from just neutron evaporation channels. The open diamonds are the sum contribution from all other decay channels.

n channel	Percentage
1n	21
2n	19
3n	17
4n	15
5n	12
6n	9
7n	6
8n	1
9n	0

Table 6.3: Percentage contributions to the  $\gamma$ -ray spectrum at 13 MeV from individual neutron decay channels calculated using CASCADE. The target excitation energy was 80–89 MeV.

from the first few steps in the decay of the target nucleus. The contributions to a typical calculated  $\gamma$ -ray spectrum from the different decay channels are displayed in figure 6.13 for a typical target excitation energy of 80–89 MeV.

The contribution to the GDR region is mainly from the neutron evaporation channels 0n through 5n. Table 6.3 lists the percentage contribution to the  $\gamma$ -ray spectrum at 13 MeV from the individual channels. The low energy slope of the spectrum is dominated by the contributions from the last few steps of the decay.

The non-statistical background in the data was accounted for by a simple exponential fit to the high energy region of the measured  $\gamma$ -ray spectrum. An exponential of the form  $\exp(-E_\gamma/E_0)$  was used with a slope parameter of  $E_0=14$  MeV obtained from bremsstrahlung systematics for the experimental beam energy of 40 MeV/nucleon [Nif90]. This exponential was normalized to the data points in the energy range of 20–30 MeV where the contributions from GDR are negligible. The statistical calculations performed with CASCADE were first folded with the detector response function and then normalized to the measured spectra in the low energy range of 7–8 MeV. The normalized non-statistical contribution was then added be-

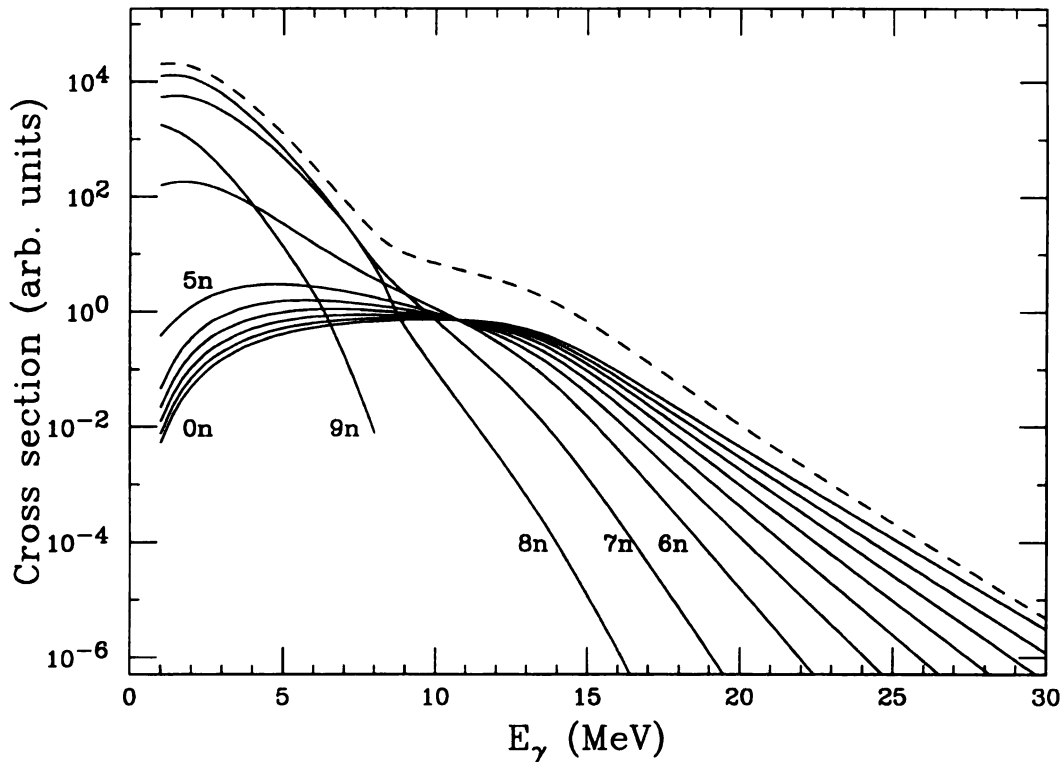


Figure 6.13: Contributions to the calculated  $\gamma$ -ray spectrum from individual neutron decay channels in  $Z=82$  nuclei. The dashed line is the calculated total  $\gamma$ -ray spectrum. The solid lines are from the nuclei  $^{208}\text{Pb}$  to  $^{199}\text{Pb}$ . The calculation was done for target excitation range of 80–89 MeV. Contributions to the GDR region arise mainly from the first few decay steps. The low energy slope is decided by the contributions from the last few nuclei in the decay chain.

fore comparing to the measured spectra. The GDR strength function influences the region of statistical  $\gamma$ -rays below 8 MeV. It is thus important to obtain a good fit to the data over the entire  $\gamma$ -ray energy range of  $\sim 5$  MeV to  $\sim 25$  MeV. A least squares fit approach is not sensitive to the GDR energy region due to the exponential nature of the  $\gamma$ -ray spectrum. The best fits were therefore obtained by varying the resonance parameters and by choosing the final fit by visual inspection.

Figure 6.14 shows the  $\gamma$ -ray spectrum for a target excitation energy range of 70–79 MeV and the calculations for the statistical and non-statistical contributions. The filled circles are the data points plotted in 1 MeV wide bins. The dashed line is the output of the statistical model calculation performed with CASCADE. The dotted line is the exponential  $\exp(-E_\gamma/E_0)$ . The solid line in the figure is the sum of the statistical and the non-statistical contributions and is in good agreement with the data. The contribution from bremsstrahlung at 13 MeV is  $\sim 15\%$ .

The above mentioned procedure was applied to the  $\gamma$ -ray spectra from all excitation energy ranges. Figure 6.15 shows the  $\gamma$ -ray spectra compared to the calculations for the excitation energy ranges of 50–59 MeV to 90–99 MeV. The calculations are in good agreement with the data in the GDR energy region and at lower  $\gamma$ -ray energies.

The data and calculations were compared on a linear scale by dividing them by an additional statistical model calculation performed with a constant dipole strength function. The strength was chosen arbitrarily to be 0.2 Weisskopf units. The division results in a strength function given by

$$f_{ave}(E_\gamma) = \frac{\Gamma^\gamma(E_\gamma)}{\Gamma_{const}(E_\gamma)} \sim \frac{f_{GDR}(E_\gamma)}{f_{const}(E_\gamma)} = \frac{E_\gamma \Gamma}{(E_0^2 - E_\gamma^2)^2 + E_\gamma^2 \Gamma^2} \quad (6.3)$$

The statistical calculation with the constant strength function was normalized first to the data in the energy range of 7–8 MeV and the bremsstrahlung contribution

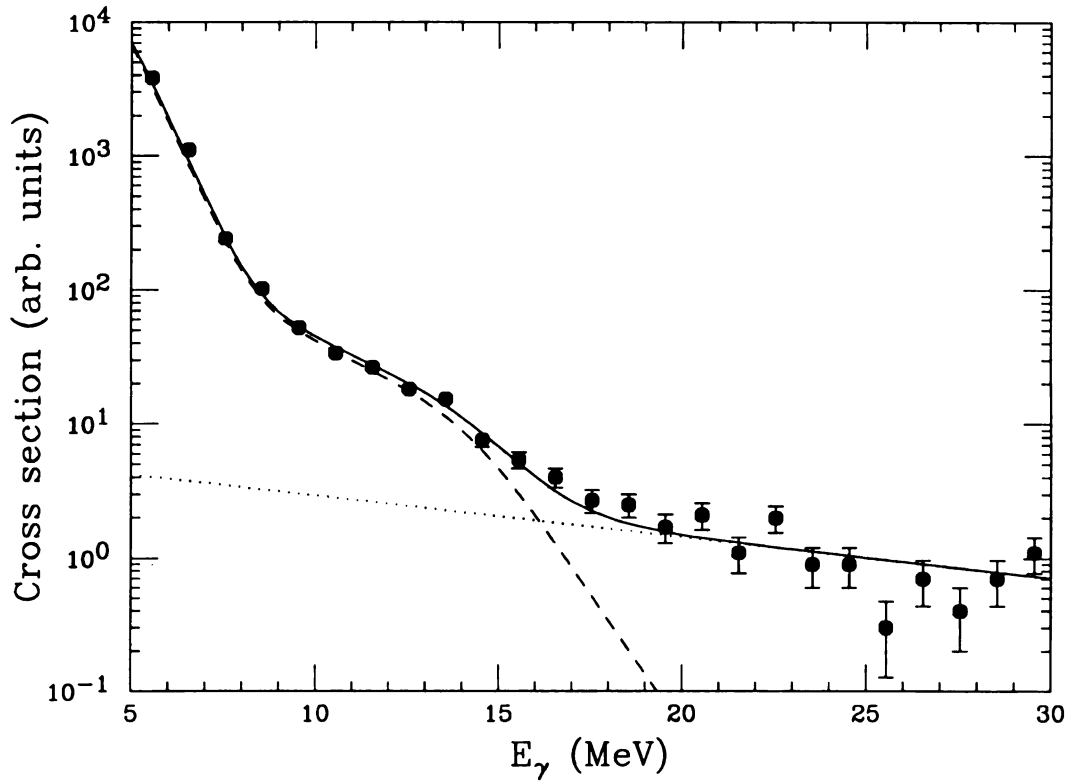


Figure 6.14: The  $\gamma$ -ray spectrum for target excitation energy of 70–79 MeV is compared to calculations. The dashed line is the result of a calculation performed with CASCADE. The dotted line is the non-statistical contribution from nuclear bremsstrahlung. The solid line is the sum of the statistical and non-statistical contributions.

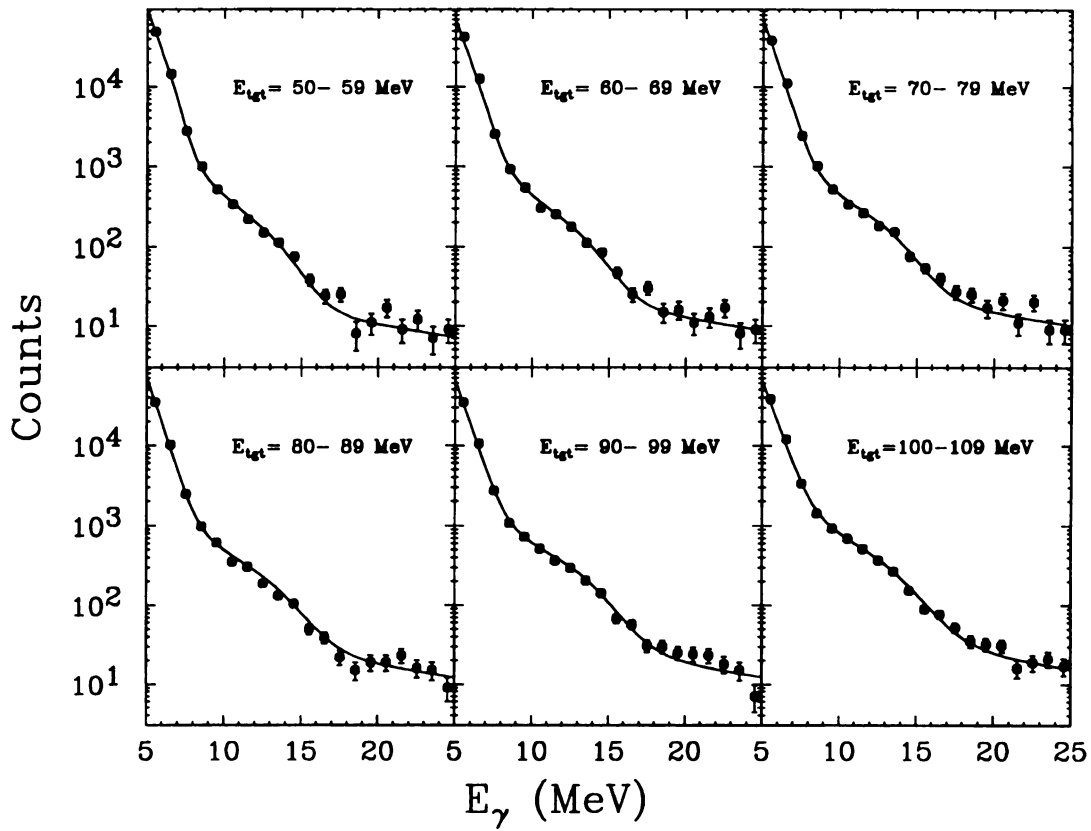


Figure 6.15: The  $\gamma$ -ray spectra for various target excitation energy ranges are compared to the model calculations. The filled circles are the measured  $\gamma$ -ray spectra and the solid line is a sum of the statistical model calculation and the bremsstrahlung component as explained in text.

was added to it. The resulting spectrum was used to divide the measured data and the model calculation including the GDR strength to yield the linearized plots. The linearized plots for various target excitation energy ranges are displayed in figure 6.16.

The resonance parameters extracted from the fits to the  $\gamma$ -ray spectra are listed in table 6.4. The error bars quoted in the table were estimated by varying one parameter at a time and visually inspecting the quality of the fit.

A dipole resonance energy value of 15.0 MeV was used in the statistical calculations for all the target excitation energy ranges. This value is 1.5 MeV above the ground state resonance value of 13.5 MeV. The quality of the fits did not vary appreciably for resonance energies in the range of 14.5 to 15.5 MeV. No systematic dependence is observed in the resonance energy as a function of target excitation energy. The resonance energy parameter input to the statistical calculations can be influenced by uncertainties in the level density parametrization. For the range of resonance energies considered in the fitting procedure, the extracted resonance width stayed within the estimated error range listed in table 6.4.

The resonance energy extracted from measurements of excited state GDR in fusion reactions have exhibited deviations from the ground state value. For instance, measurements in excited  $S_n$  isotopes yielded a resonance energy parameter 1 MeV lower than the energy of the ground state resonance [Cha87]. No systematic dependence is observed over the mass range. The deviations observed in fusion-evaporation measurements have not been studied in detail.

The parameter  $S_{GDR}$  is the fraction of the classical E1 sum rule strength input to the statistical calculation. This parameter is seen to decrease from a value of 1.0 at low excitation energies to  $\sim 0.5$  at higher energies. This decrease in the sum rule strength may be due to processes in the inelastic scattering that do not induce



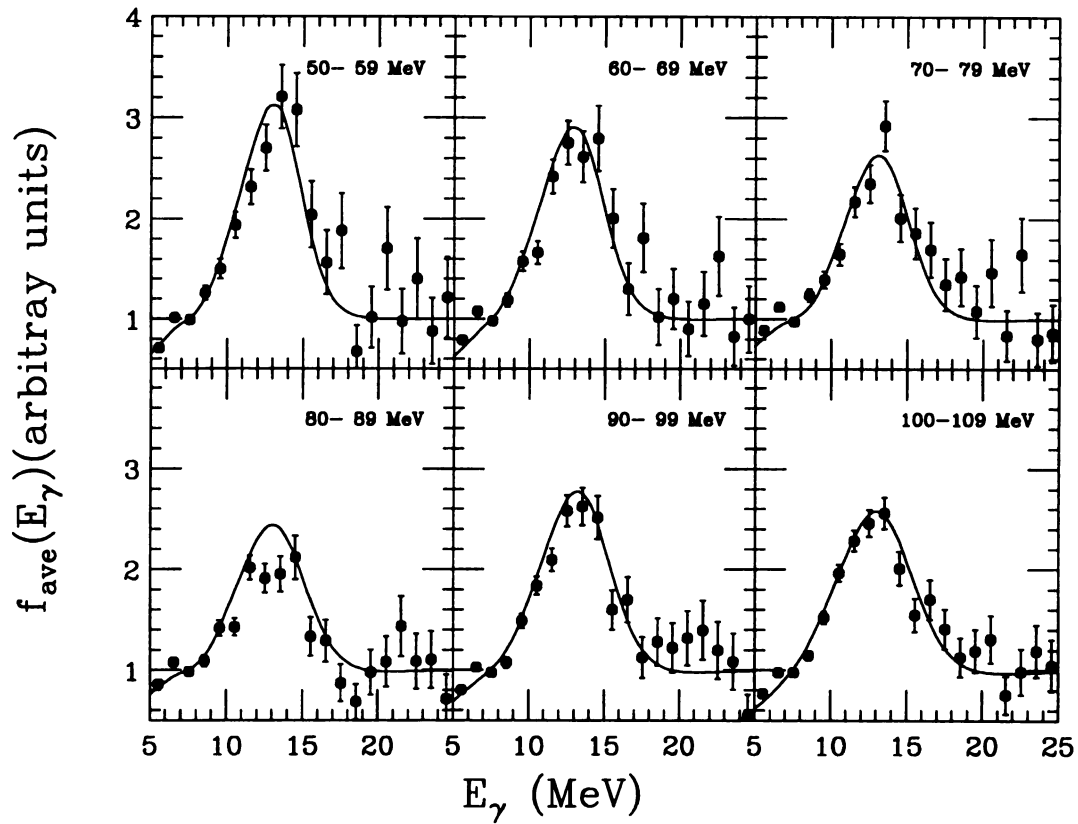


Figure 6.16: The  $\gamma$ -ray spectra for various target excitation energy ranges are compared to the calculations on a linear scale. The linearized plots were obtained on dividing the data and the calculations by a second model calculation employing an energy independent dipole strength.

Excitation Range (MeV)	$\Gamma_{GDR}$ (MeV)	$S_{GDR}$
40–49	$5.7 \pm 0.5$	$1.00 \pm 0.1$
50–59	$6.0 \pm 0.5$	$0.80 \pm 0.1$
60–69	$6.5 \pm 0.5$	$0.80 \pm 0.1$
70–79	$6.5 \pm 0.5$	$0.55 \pm 0.1$
80–89	$7.2 \pm 0.5$	$0.45 \pm 0.1$
90–99	$7.0 \pm 0.5$	$0.55 \pm 0.1$
100–109	$8.0 \pm 0.5$	$0.70 \pm 0.1$

Table 6.4: GDR parameters extracted for various target excitation energy ranges.

collective excitations in the target, but however contribute to the  $\gamma$ -ray spectra in the energy region below  $\sim 8$  MeV. A lower sum rule strength is therefore required to obtain a good fit to the  $\gamma$ -ray spectra in the range of 5–30 MeV.

The resonance width extracted from the fitting procedure is seen to increase systematically with increasing target excitation energy. The excitation energy is given by

$$E_{ex} = E_{mean} - E_{rot} \quad (6.4)$$

where  $E_{mean}$  is the mean energy of the input population derived from the particle singles spectrum and  $E_{rot}$  is the rotational energy corresponding to the mean angular momentum of nuclei in the input population. Table 6.5 lists the above mentioned quantities for the different target excitation energy ranges.

Figure 6.17 displays the resonance width as a function of excitation energy  $E_{ex}$ . The data points are shown as filled circles. The filled square is the width of the resonance built on the ground state [Die88]. The width values are well described by a linear dependence on the excitation energy. The solid line in the figure is a linear fit to the data points including the ground state point and is given by the expression

$$\Gamma_{GDR}(E_{ex}) = (3.42 \pm 0.13) + (0.044 \pm 0.003) \times E_{ex}. \quad (6.5)$$

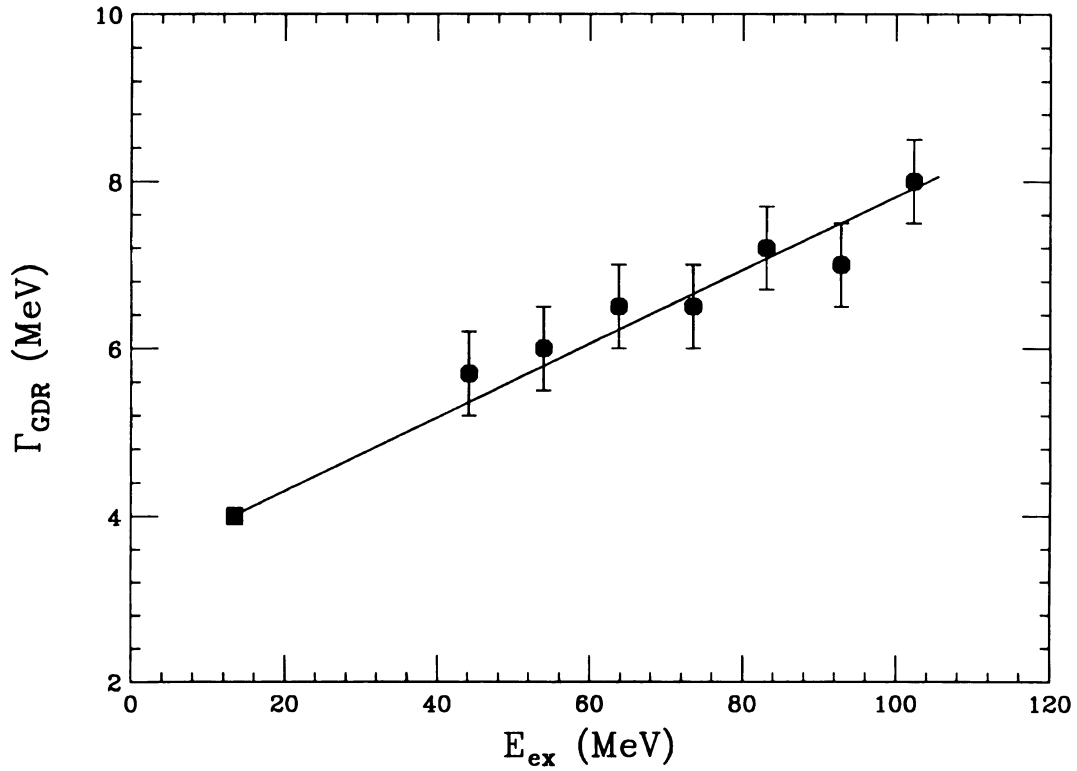


Figure 6.17: The resonance width as a function of excitation energy in  $^{208}\text{Pb}$ . The excitation energy was obtained by subtracting the rotational energy from the mean energy of the input population derived from the  $\alpha$  singles spectra. The solid circles are the widths obtained from fitting the calculations to the data and the solid square is the width of the resonance built on the ground state. The line is the result of a linear fit to the data set including the ground state point.

Excitation Range (MeV)	$E_{mean}$ (MeV)	$L_{mean}$ ( $\hbar$ )	$E_{rot}$ (MeV)	$a(E_{eff})$ (MeV $^{-1}$ )	T (MeV)
40–49	44.38	8	0.28	16.27	1.34
50–59	54.35	10	0.45	17.54	1.49
60–69	64.42	12	0.66	18.54	1.62
70–79	74.42	14	0.91	19.31	1.74
80–89	84.47	17	1.36	19.93	1.85
90–99	94.55	19	1.71	20.44	1.95
100–109	104.64	21	2.31	20.84	2.05

Table 6.5: Calculation of nuclear temperature from the effective excitation energy. The rotational energy and the GDR energy were subtracted from the mean excitation energy and the temperature was calculated with an energy dependent level density parameter.

The nuclear temperature in  $^{208}\text{Pb}$  for the different excitation energies was computed using the expression

$$T = \sqrt{\frac{E_{eff}}{a(E_{eff})}} \quad (6.6)$$

where  $E_{eff}$  is the effective excitation energy given by

$$E_{eff} = E_{mean} - E_{rot} - E_{GDR}. \quad (6.7)$$

The quantity  $a(E_{eff})$  is the energy dependent level density parameter that was obtained using the parametrization described in chapter 5. The temperature  $T$  corresponding to each target excitation energy range is listed in table 6.5.

The width as a function of the temperature in  $^{208}\text{Pb}$  is plotted in figure 6.18. The solid line in the figure is a second order fit to the data points including the ground state width, and is given by the expression

$$\Gamma_{GDR}(T) = (4.0 \pm 0.1) + (0.89 \pm 0.07) \times T^2. \quad (6.8)$$

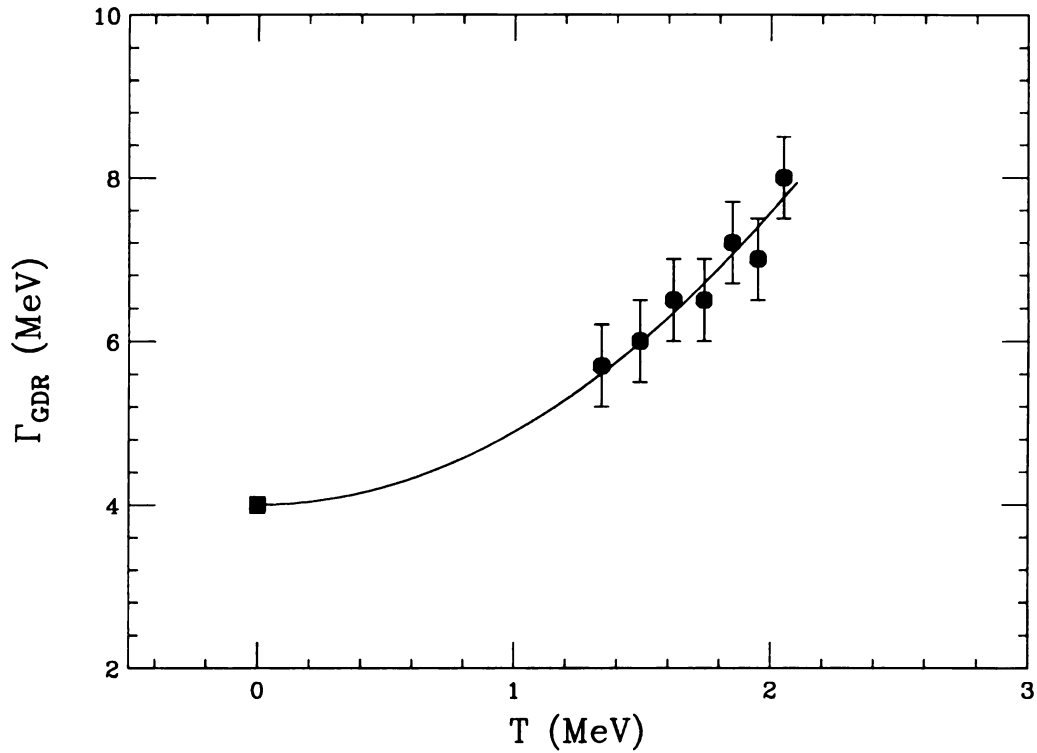


Figure 6.18: The resonance width as a function of temperature in  $^{208}\text{Pb}$ . The temperature was obtained from the effective excitation energy by using an energy dependent level density parameter as explained in text. The solid circles are the widths obtained from fitting the calculations to the data and the solid square is the width of the resonance built on the ground state. The line is the result of a second order fit to the data set including the ground state point.

### 6.3 Resonance Width

The measured resonance widths can be compared to model calculations that describe the evolution of the giant dipole resonance with increasing excitation energy and angular momentum.

One such model attributes the evolution of the resonance width as due to the coupling of the collective degrees of freedom to the nuclear potential landscape [Bro92]. At low excitation energies the contribution to the width arises from small amplitude quantal fluctuations in the potential surface. These fluctuations in shape are induced by the zero point motion of a harmonic vibrator in the deformation degrees of freedom. The resonance width from quantal fluctuations accounts for the majority of the ground state width in heavy nuclei. In excited nuclei, other than the quantal fluctuations of the surface, there are also large amplitude thermal fluctuations where nuclear shapes over the entire  $(\beta, \gamma)$  deformation plane are sampled. These thermal fluctuations result in a broadening of the width of the GDR [Pac88, Bor89].

Ormand *et al.* have performed detailed calculations of the evolution of the resonance in excited  $^{208}\text{Pb}$  nuclei by considering the coupling of the collective excitation to the nuclear free energy surface [Orm95]. The coupling was assumed to be adiabatic in nature such that the time scale of the shape fluctuations are large compared to the damping time of the GDR.

In their model, the probability that a given deformation  $\alpha$  in the  $(\beta, \gamma)$  plane is experienced by the nucleus at a temperature  $T$ , is given by the Boltzmann factor

$$p(\alpha) \propto \exp[-F(T, \alpha)], \quad (6.9)$$

where

$$F(T, \alpha) = E - T S - \vec{I} \cdot \vec{\omega} \quad (6.10)$$

is the nuclear free energy. Here,  $E$  is the excitation energy,  $S$  is the entropy,  $\vec{I}$  is the angular momentum and  $\vec{\omega}$  is the rotational frequency [Gar92].

The observed GDR cross section is then written as a weighted average over the deformation parameter as

$$\sigma(E_\gamma) = \frac{1}{Z} \int D[\alpha] \sigma(\alpha, E_\gamma) \exp[-F(T, \alpha)], \quad (6.11)$$

where  $E_\gamma$  is the photon energy and

$$Z = \int D[\alpha] \exp[-F(T, \alpha)] \quad (6.12)$$

is the partition function. The quantity  $D[\alpha]$  is the volume element for the integration in the five dimensional space formed by the deformation parameters  $\beta, \gamma$  and the three Euler angles that define the orientation of the nucleus with respect to  $\vec{\omega}$  [Gal85, Pac88, Alh90]. The deformation dependent cross section  $\sigma(\alpha, E_\gamma)$  for the GDR was computed using a harmonic oscillator model that considers vibrations along the three principal axes of the deformed nucleus, with frequencies corresponding to the inverse of the radius for each axis. The intrinsic resonance width for each resonance energy component  $E_j$  was parametrized by a power law [Alh90]

$$\Gamma_j = \Gamma_0 \left( \frac{E_j}{E_0} \right)^{1.6}, \quad (6.13)$$

where  $\Gamma_0$  is the ground state width and  $E_0$  is the ground state resonance energy. Such a parametrization is necessary because no fundamental microscopic description of the dipole resonance widths that reproduce the experimental data is currently available.

The nuclear free energy plays an important role in the determination of the GDR cross section in hot nuclei. The free energy as a function of temperature  $T$  and deformation  $\beta$  was evaluated using the Nilsson-Strutinsky procedure [Str68]. This procedure assumes that the global bulk properties of the nucleus are well described

by the liquid drop model, while local shell effects are accounted for by the Strutinsky shell correction applied to the Nilsson hamiltonian. The free energy was parametrized by functions that mimic the behaviour of the Nilsson-Strutinsky calculations as close as possible. A simple and accurate evaluation of the free energy for a wide range of deformations and temperatures was thus achieved without having to explicitly perform a Nilsson-Strutinsky calculation at each deformation point.

Figure 6.19 displays the width of the GDR obtained from the calculated cross sections, in comparison to the measured data. The angular momentum of the nucleus was assumed to be zero. The calculated width does not change appreciably up to a temperature of  $\sim 1$  MeV due to the persistence of shell effects in  $^{208}\text{Pb}$ . Beyond 1 MeV, the shell effects vanish and the width increases with increasing temperature. The surface energy plots in figure 2.2 displayed this feature. There the free energy surface was seen to broaden rather rapidly between 1 and 2 MeV.

The main goal of this measurement was to study the evolution of the width as a function of excitation energy with very little influence from angular momentum. In fusion-evaporation reactions large angular momenta are populated in the nucleus over a broad range of values. The width increase observed in fusion measurements have been attributed mainly to angular momentum, with a less significant contribution from excitation energy [Bro92]. Inelastic scattering populates low angular momentum states and thus the properties of nuclei in a narrow range of excitation energy and spin can be studied. In the absence of large spins the width of the resonance should increase rather slowly with increasing excitation energy. The calculated widths exhibit a dependence on the nuclear temperature given by  $\Gamma_{GDR} \sim \sqrt{T}$ .

The calculation is in good agreement with the data over the range of temperatures observed in the measurement. Clearly more data is needed at temperatures beyond 2 MeV to compare the behaviour of the resonance with calculations at higher excitation



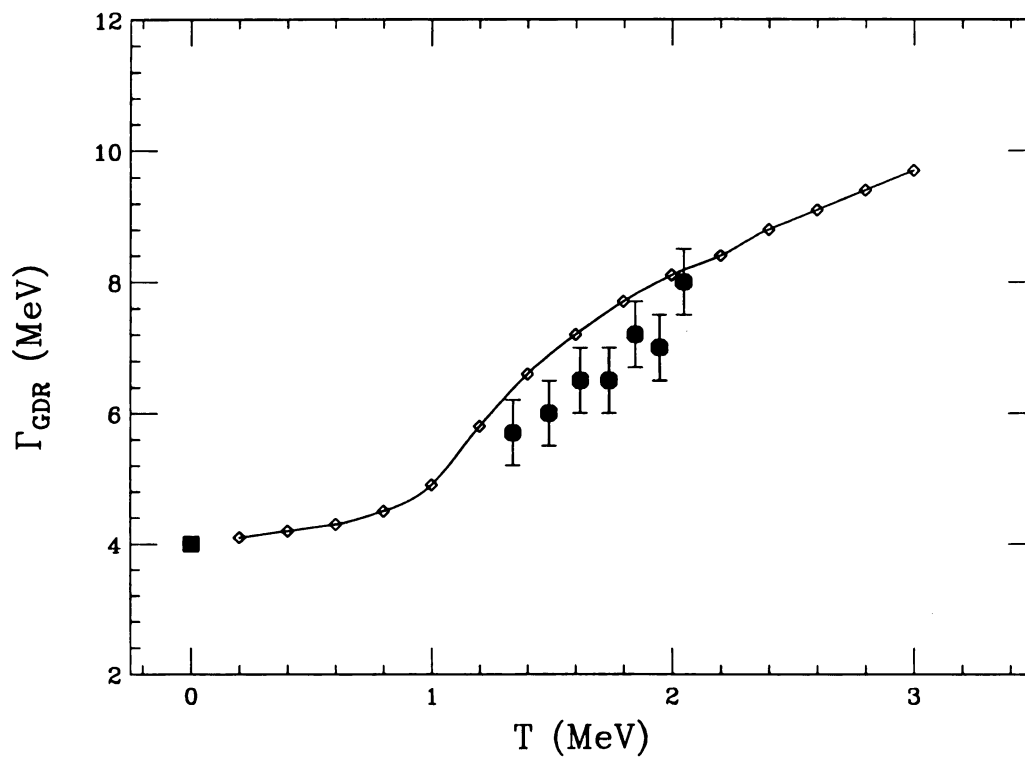


Figure 6.19: Measured resonance width compared to calculations that consider the coupling of the GDR to the nuclear free energy surface. The filled circles are the widths obtained from fitting the  $\gamma$ -ray spectra. The open diamonds are the model calculations performed by Ormand *et al.* The filled square is the ground state resonance point. The calculation is in good qualitative agreement with the data.

energies. Temperatures below 1 MeV are not accessible for study using giant dipole resonance measurements.

Smerzi *et al.* have proposed an alternate theoretical description for the evolution of the resonance width with excitation [Sme91]. In their model the damping of the resonance is treated purely in terms of nucleon-nucleon collisional dynamics. The effect of one- and two-body dissipation is studied by solving a semiclassical Vlasov equation including a collisional relaxation time. The relaxation time is the time required for the perturbed system to reach a new equilibrium under the effect of two-body collisions.

The relaxation width as a function of temperature is expressed in their model as

$$\Gamma_{R(T)} = \Gamma_{R(T=0)} \left[ 1 + \frac{\epsilon_T}{\epsilon_D} \right], \quad (6.14)$$

where

$$\epsilon_T = \frac{\pi^2 T^2}{4\epsilon_F} \quad (6.15)$$

is the thermal energy density, and

$$\epsilon_D = \frac{E_{GDR}}{A} \quad (6.16)$$

is the collective energy density. The quantity  $\epsilon_F$  is the Fermi energy.

Such finite temperature relaxation widths are employed in solving the collisional dynamics. The results of their calculation for  $^{208}\text{Pb}$  is displayed in figure 6.20 in comparison to the data. A rapid increase in the width is seen at lower temperatures. The calculated resonance widths are rather large compared to the data. For temperatures above 2 MeV, the calculated widths display a saturation effect. They attribute the saturation to the slow disappearance of the GDR strength with increasing excitation energy. The observed dipole strength at high excitation energies in their model thus corresponds to cooler nuclei that are populated subsequent to particle evaporation.

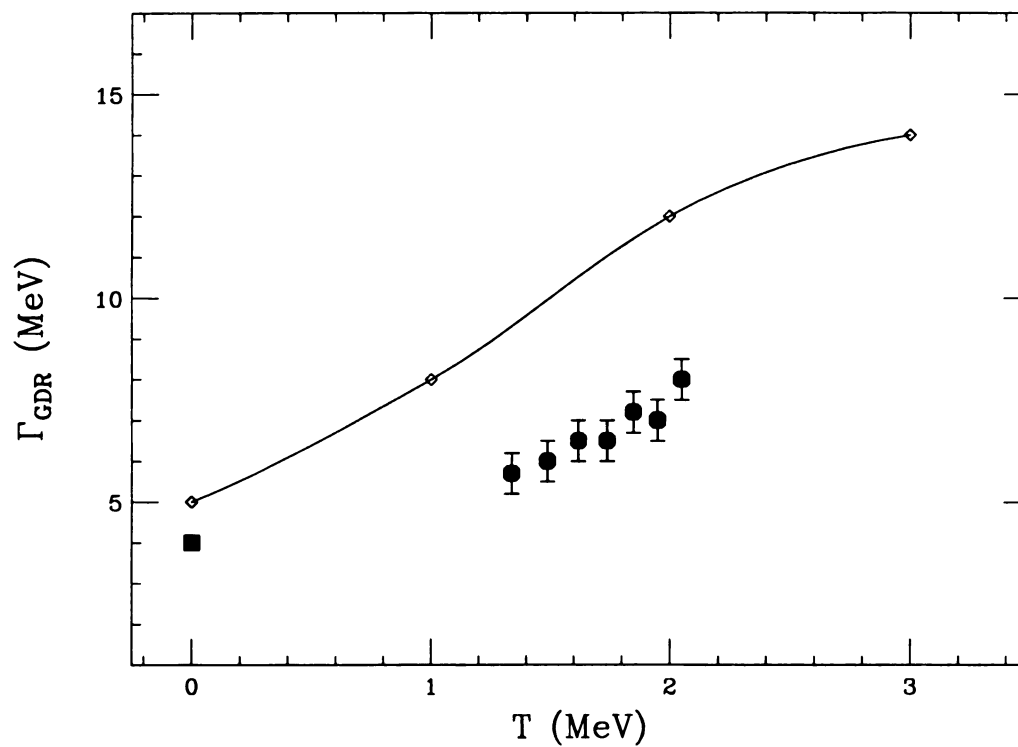


Figure 6.20: Measured resonance width compared to calculations performed using collisional dynamics model. The filled circles are the data points from the experiment. The filled square is the ground state width. The open diamonds are results of the model calculation by Smerzi *et al.* The calculations predict resonance widths that are much larger than those obtained from experiment.

## 6.4 Pre-equilibrium Emission

At the lower energy end of the particle spectra processes other than inelastic scattering contribute to the measured cross section. The cross section is seen to rise with increasing projectile energy loss for  $\alpha$  energies below  $\sim 50$  MeV. The target excitation energy in this region cannot be deduced purely from the energy loss of the projectile.

Figure 6.21 shows the  $\alpha$  singles spectra from the four WALL rings in the low energy range. The cross section rises with decreasing  $\alpha$  energy in this range in all four rings.

Previous measurements of inelastic  $\alpha$  scattering on  $^{208}\text{Pb}$  did not observe this behaviour due to higher thresholds on the particle detectors [You76, Ber80].

The slope of the cross section at lower energies is too shallow to be accounted for by the statistical emission of  $\alpha$ -particles in the decay of the excited target nucleus. Figure 6.22 shows the cross section of  $\alpha$ -particles from the decay of equilibrated  $^{212}\text{Po}$  formed by the fusion of 40 MeV/nucleon  $\alpha$ -particles on  $^{208}\text{Pb}$  in comparison to the measured inelastic spectrum from ring 1. The evaporation calculation was performed with CASCADE. The angular distribution of evaporated emission is isotropic. The calculation was scaled to account for the solid angle acceptance of the detectors. It is clear from the figure that though the cross section for the evaporation process is comparable to the measured cross section, the evaporation spectrum has a much steeper slope than that of the measured  $\alpha$  spectrum.

The shape of the  $\alpha$  spectrum at low energies is due to pre-equilibrium processes occurring in the scattering. For sufficiently low impact parameters the incoming  $\alpha$ -particle could undergo multiple interactions with the nucleons of the target. As a result of these interactions one or more particles could be emitted from the target before equilibration of the energy is achieved. It is possible that a proton or a deuteron

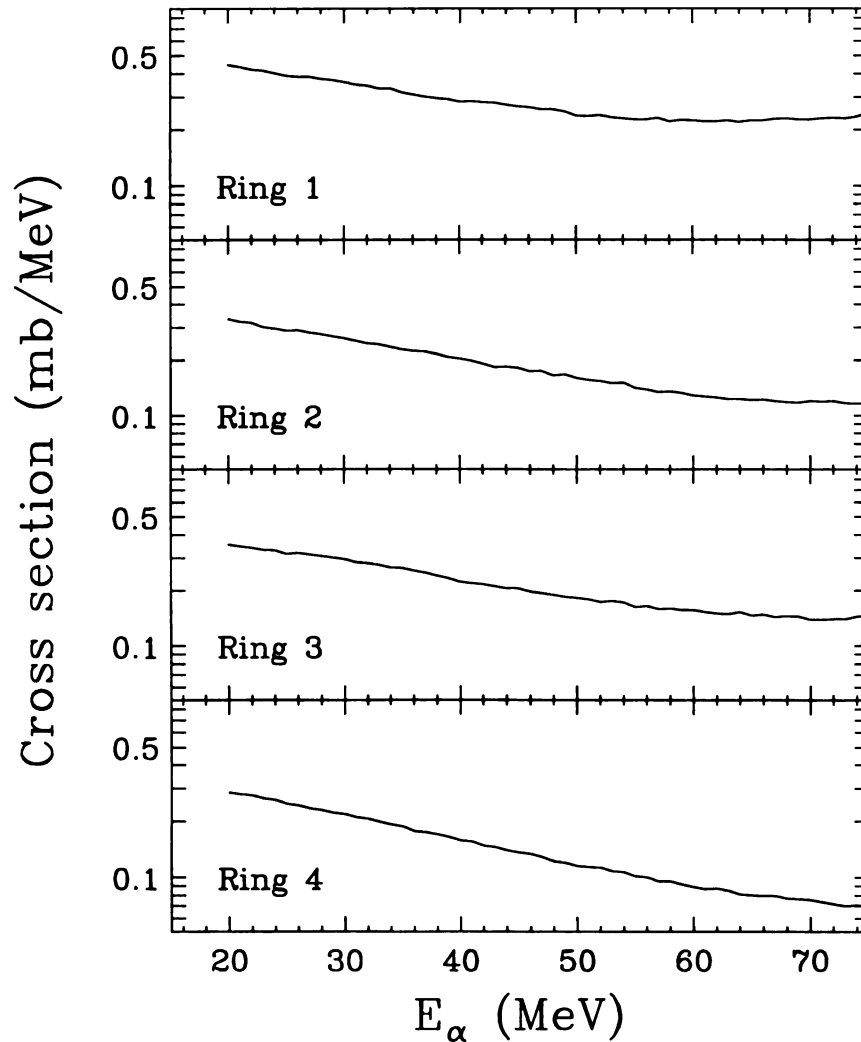


Figure 6.21:  $\alpha$  singles spectra in the four rings of the WALL array at the low energy end is displayed. The spectrum from ring 1 was converted to absolute cross section scale as described in section 6.1.1. The spectra from rings 2 to 4 were scaled to absolute cross section by normalizing the solid angles of these rings to the solid angle of ring 1. The cross section is seen to rise with decreasing  $\alpha$  energy in all four spectra.

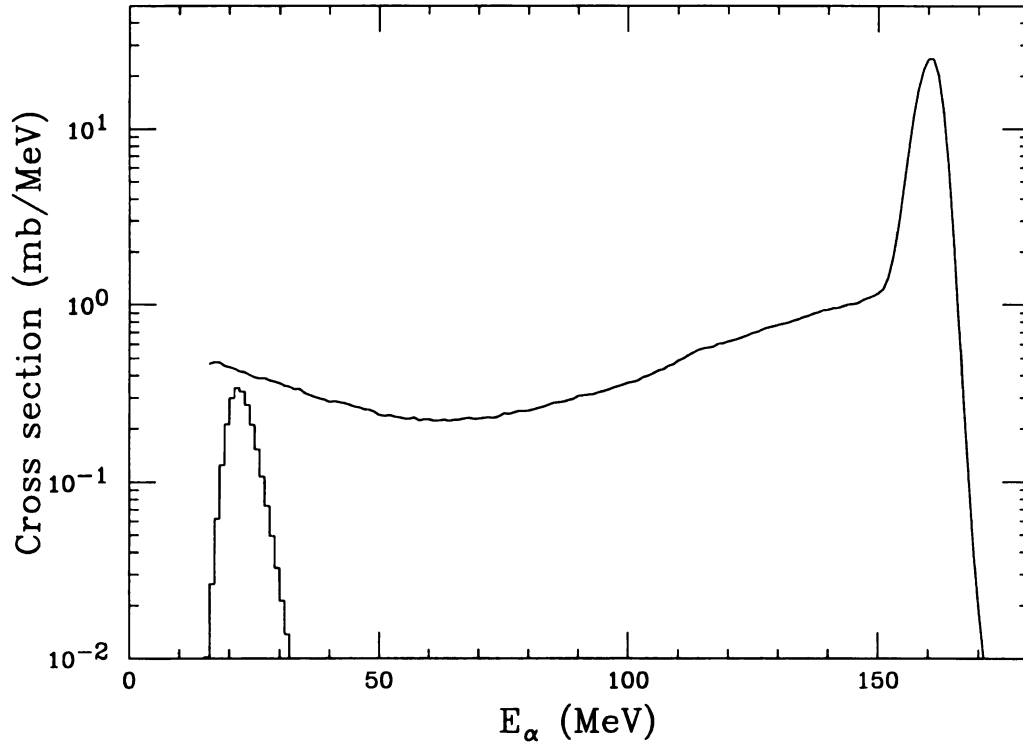


Figure 6.22: The calculated  $\alpha$  evaporation spectrum from the decay of  $^{212}\text{Po}$  formed by the fusion of 40 MeV/nucleon  $\alpha$  on  $^{208}\text{Pb}$  (histogram) is shown in comparison to the  $\alpha$  spectrum measured in ring 1 of the WALL array from the inelastic scattering (solid line). The evaporation calculation was done with CASCADE. Evaporated  $\alpha$  particles have an isotropic distribution. The calculation was scaled to correspond to the solid angle acceptance of ring 1. Though the evaporation cross section is comparable in magnitude to the measured cross section, the slope of the evaporated  $\alpha$  particles is much steeper compared to the slope of the measured spectrum at low energies.

or another  $\alpha$ -particle is emitted from the pre-equilibrium stage.

Emission from the pre-equilibrium stage should be forward focussed. Figure 6.23 shows that this feature is observed in the data. The figure displays the  $\alpha$  spectra from various rings of the BALL array which were measured in coincidence with an  $\alpha$ -particle in the WALL array. The pre-equilibrium signature is seen in the forward rings of the BALL. As the measurement angle becomes more backward, the spectral shape approaches that of evaporated  $\alpha$ -particles from an excited target nucleus.

Another signature for pre-equilibrium processes can be seen in the high energy region of the coincidence  $\gamma$ -ray spectra. For  $\gamma$ -ray energies above  $\sim 20$  MeV, there is no significant contribution to the spectra from the GDR. This region is therefore indicative of processes like nuclear bremsstrahlung that generate high energy  $\gamma$  rays. If the incoming  $\alpha$ -particle interacts strongly with the target nucleus, the nuclear bremsstrahlung contribution should increase. Figure 6.24 displays the integrated counts in the  $\gamma$ -ray spectra in the 20–30 MeV energy range in comparison to the singles cross section. The figure shows that as the measured  $\alpha$  energy decreases the high energy  $\gamma$ -ray contribution increases, and reaches a maximum in the pre-equilibrium energy range. This indicates that at lower  $\alpha$  energies the interaction of the projectile with the nucleons of the target increases, and this could result in enhanced pre-equilibrium emission.

Statistical model calculations can be performed to fit the  $\gamma$ -ray spectra in coincidence with the  $\alpha$ -particles from the pre-equilibrium region. Figure 6.25 displays the  $\gamma$ -ray spectra in coincidence with  $\alpha$  energies of 21–30 MeV, 31–40 MeV and 41–50 MeV. The apparent target excitation energies are 130–139 MeV, 120–129 MeV and 110–119 MeV respectively. Statistical model calculations assuming these excitation energies are shown in the figure along with the linearized plots. The width of the resonance as extracted from these fits does not increase with excitation energy, and

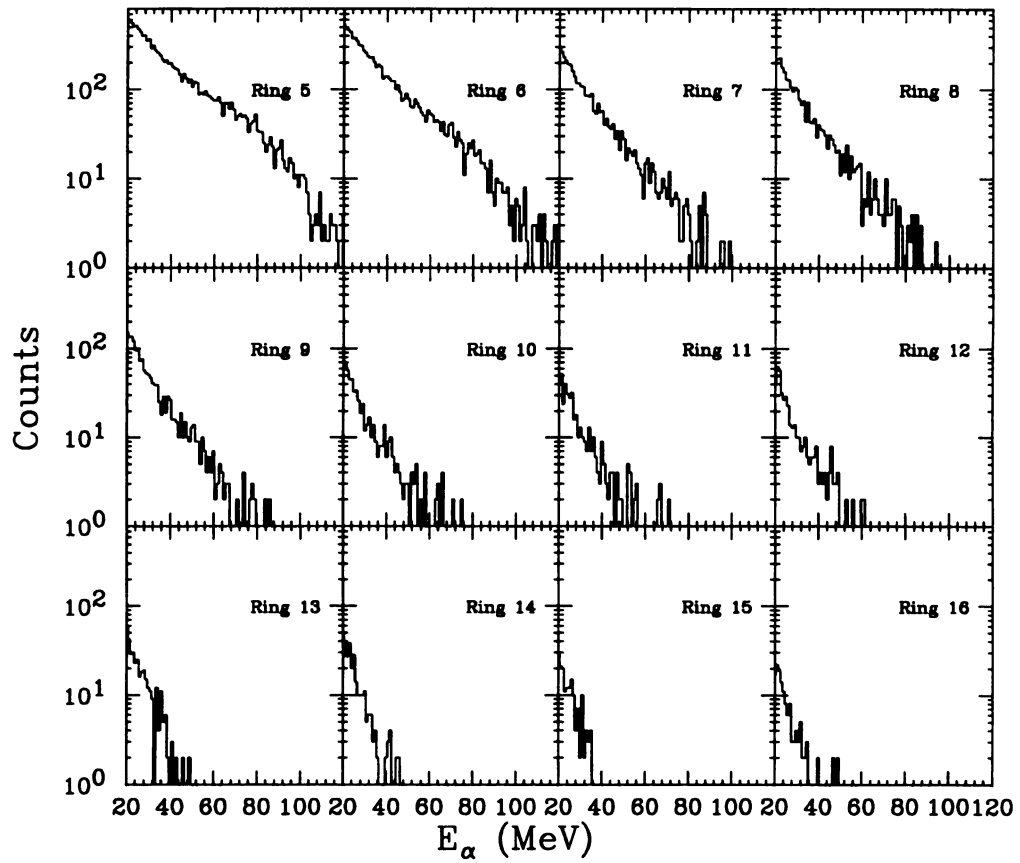


Figure 6.23:  $\alpha$  spectra from various rings in the BALL array. These spectra were measured in coincidence with an  $\alpha$  particle detected in one of the WALL rings. The pre-equilibrium feature of the spectra disappears as the detection angle becomes more and more backward. At the most backward angles the spectra are similar to that obtained from evaporation calculations.



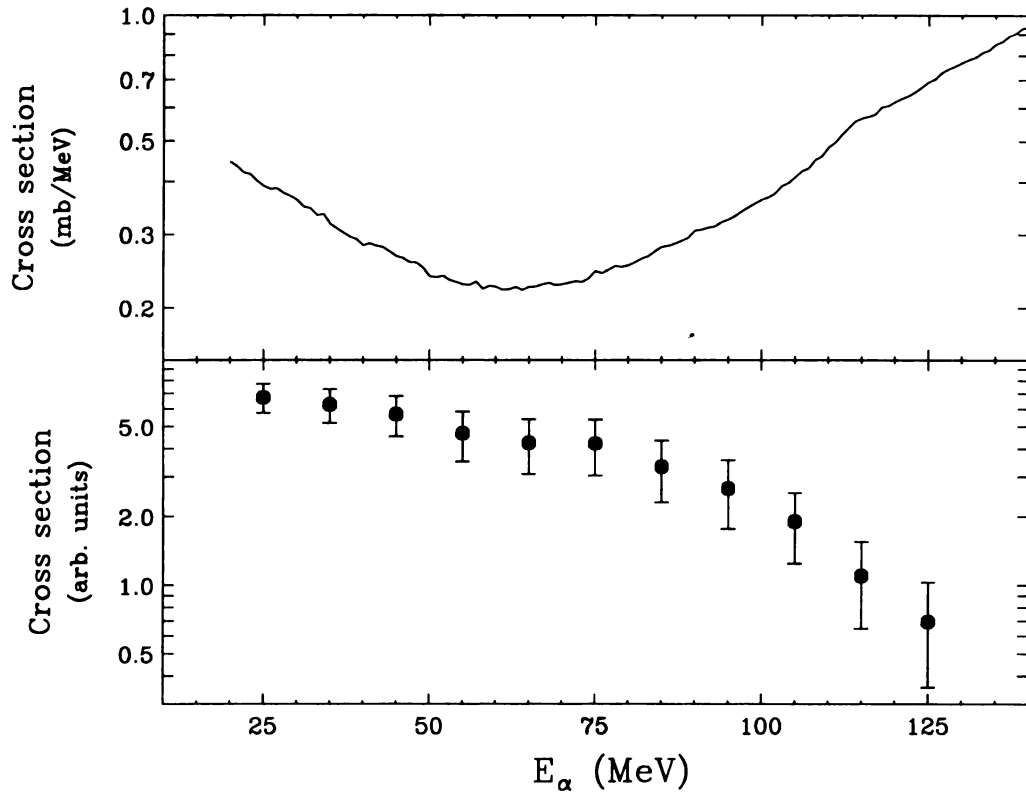


Figure 6.24: The high energy background in the  $\gamma$ -ray spectra are compared to the singles cross section. The top panel shows the singles spectrum from ring 1 of the WALL array. The bottom panel displays the integrated counts from the 20–30 MeV region of the  $\gamma$ -ray spectra, for each 10 MeV wide target excitation energy cut. The summed counts were normalized by dividing with the singles cross section. The normalized high energy  $\gamma$ -ray background increases with increasing projectile energy loss, and is strongest in the pre-equilibrium region.

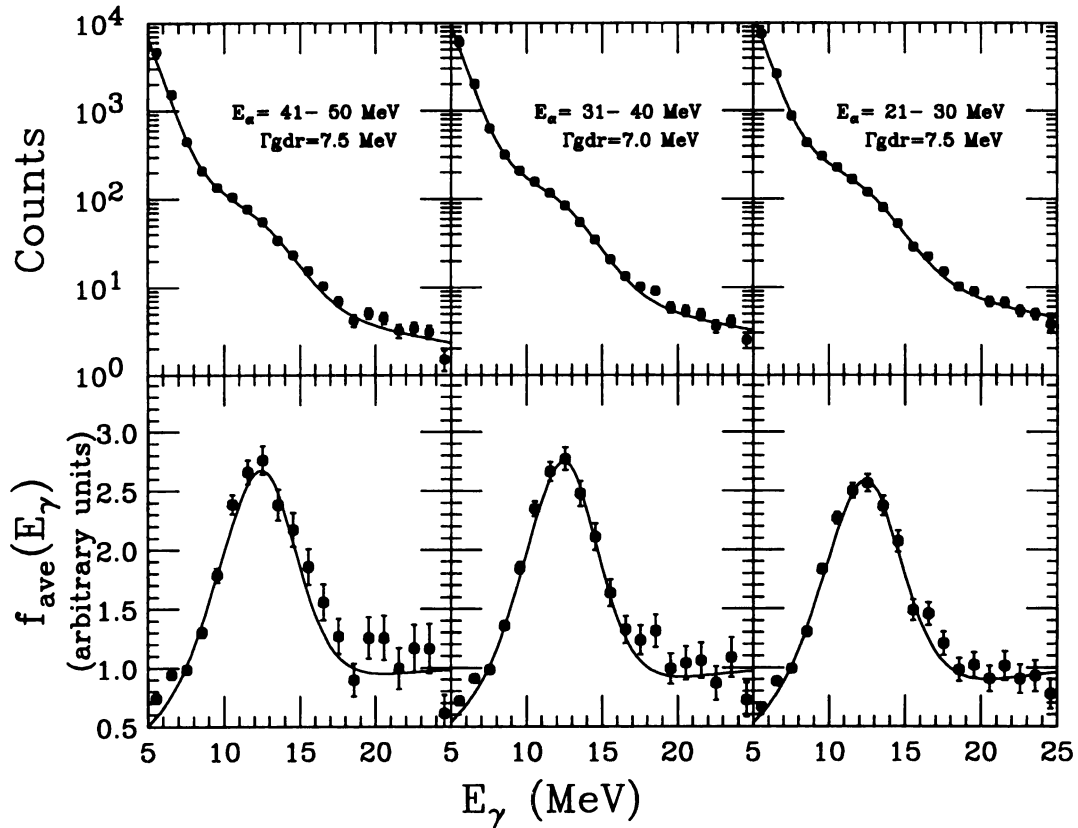


Figure 6.25: The  $\gamma$ -ray spectra in coincidence with  $\alpha$  particles of energies 21–30 MeV, 31–40 MeV and 41–50 MeV. Apparent target excitation energies as 130–139 MeV, 120–129 MeV and 110–119 MeV respectively. The statistical model calculations performed assuming these excitation energies are shown as solid lines in the upper panels. The lower panels display the corresponding linearized plots. The resonance width stays at a value of  $\sim 7.5$  MeV indicating that the  $\gamma$ -rays are emitted by cooler nuclei that are populated after pre-equilibrium emission.

stays at a value of  $\sim 7.5$  MeV. These widths are compared in figure 6.26 to the resonance widths extracted for excitation energies where pre-equilibrium contributions are negligible. The saturation in the width at apparent high excitation energies indicates that the  $\gamma$ -rays arise perhaps from cooler nuclei that are populated subsequent to particle emission in the pre-equilibrium stage.

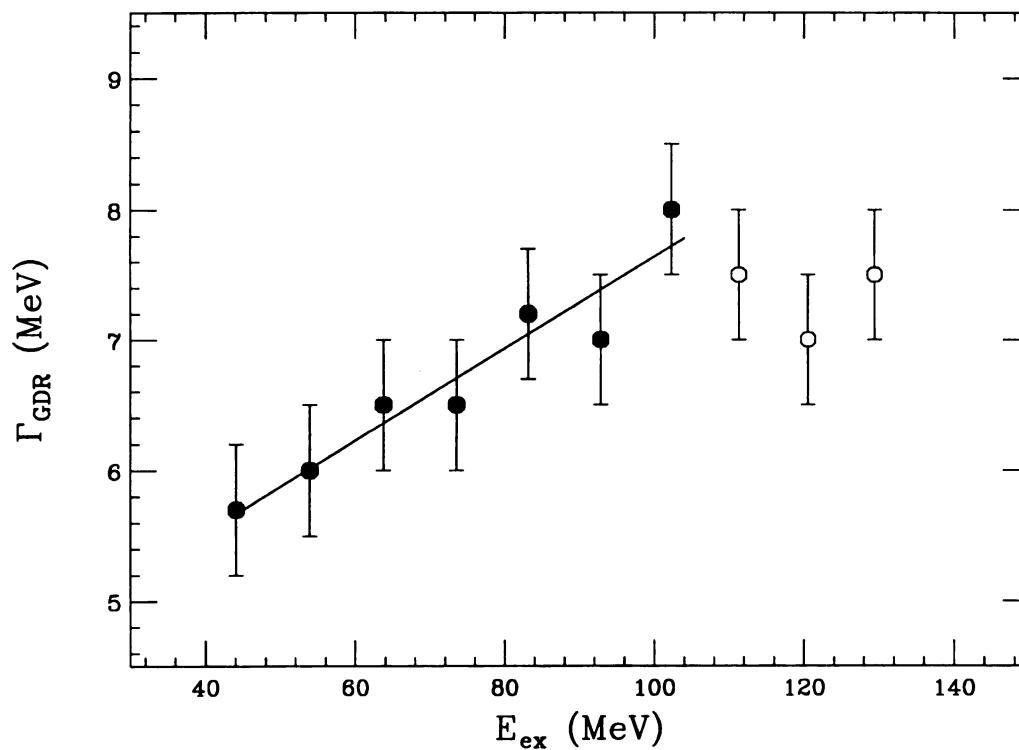


Figure 6.26: The resonance widths at large projectile energy losses are compared to the widths at lower excitation energies. The open circles are the widths extracted from  $\gamma$ -ray spectra for  $\alpha$  energies in the range of 21–50 MeV. The apparent target excitation energies are 110–139 MeV. The filled circles are the widths for excitation energies from 40–109 MeV where the pre-equilibrium contributions are negligible. The widths at apparent high excitation energies exhibit a saturation effect since they correspond to the GDR in nuclei populated subsequent to particle emission in the pre-equilibrium stage.

# Chapter 7

## Summary and Conclusions

In this measurement, the evolution of the giant dipole resonance in  $^{208}\text{Pb}$  was studied as a function of excitation energy with very little influence from angular momentum. This was achieved by exciting the nucleus with inelastic scattering of  $\alpha$ -particles. The GDR built on highly excited states of the nucleus was observed by measuring the high energy  $\gamma$  rays from the decay of the resonance in coincidence with the inelastically scattered projectiles.

The enhancement due to the GDR was observed in the coincidence  $\gamma$ -ray spectra at all measured excitation energies. Furthermore, the  $\alpha$  spectra measured in coincidence with the high energy  $\gamma$  rays exhibited structures that corresponded to individual neutron evaporation channels in the decay of the excited target nucleus. These observations were evidence for equilibrated emission from a highly excited target nucleus.

The  $\gamma$ -ray spectra were compared to statistical model calculations performed using the CASCADE code and resonance parameters were extracted as a function of excitation energy. The width of the GDR was observed to increase with increasing excitation energy from a value of 4 MeV at the ground state to  $\sim 8$  MeV at the highest measured energy.

The measured widths were compared to the results of an adiabatic model calculation for the resonance energy cross section that took into account the coupling of the resonance to the nuclear free energy surface. The calculation predicted an increase in the resonance width with excitation energy for temperatures beyond  $\sim 1$  MeV, subsequent to the disappearance of shell effects in  $^{208}\text{Pb}$ . The calculated widths were in good agreement with the data over the range of temperatures observed in the measurement.

This was a first measurement of the GDR built on excited states of a stable nucleus studied by means of inelastic light ion scattering. The observation of width evolution in this study was strongly influenced by the presence of shell effects in  $^{208}\text{Pb}$  at lower excitation energies. It would therefore be interesting to measure the resonance width in other nuclei where shell effects are not prominent. Nuclei with deformed shapes in the ground state form an interesting choice since the shape evolution can be studied independent of spin.

Recently angular distribution measurements have yielded additional information for the determination of nuclear shapes. A larger solid angle coverage for the  $\gamma$ -ray detectors can yield sufficient statistics to perform angular distribution analysis of the data which is valuable in the study of shape evolution in excited nuclei.

Presently the use of discrete particle detector arrays limits the choice of projectile nuclei to those that could be isotopically identified. Measurements at very small scattering angles where the inelastic cross section is larger are also not possible due to significantly large elastic scattering cross sections. These limitations can be overcome in the future by the use of magnetic spectrographs.

The choice of  $\alpha$ -particles as the inelastic probe in this study ensured that there is no contamination to the  $\gamma$ -ray spectra from projectile excitation since there are

no bound excited states in the projectile. However, pre-equilibrium effects at large projectile energy losses posed a problem. The cross section for pre-equilibrium emission may be much suppressed for the less bound system of  $^3\text{He}$ , thereby making this nucleus a better choice for the inelastic probe. Calculations that consider emission from the pre-equilibrium stage could confirm this speculation. Other light ion probes such as  $^7\text{Li}$  that have low particle separation energies could also be chosen.

More systematics on the evolution of the GDR width as a function of excitation energy in nuclei over a wide mass range are required to perform comparisons with model calculations. Coincidence measurement of  $\gamma$  rays with inelastic light ion scattering can serve as an important tool towards achieving this goal.

# Bibliography

- [Alh90] Y. Alhassid and B. Bush, *Nuc. Phys. A* **509**, 461 (1990).
- [Ber80] F. E. Bertrand, G. R. Satchler, D. J. Horen, J. R. Wu, A. D. Bacher, G. T. Ewery, W. P. Jones, D. W. Miller and A. van der Woude, *Phys. Rev. C* **22**, 1832 (1980).
- [Ber83] G. F. Bertsch, P. F. Bortignon and R. A. Broglia, *Rev. Mod. Phys.* **55**, 287 (1983).
- [Bee89] J. R. Beene, F. E. Bertrand, M. L. Halbert, R. L. Auble, D. C. Hensley, D. J. Horen, R. L. Robinson, R. O. Sawyer, and T. P. Sjoreen, *Phys. Rev. C* **39**, 1307 (1989).
- [Bee94] J. R. Beene, *Nuc. Phys. A* **569**, 163c (1994).
- [Blu88] Y. Blumenfeld and Ph. Chomaz, *Phys. Rev. C* **38**, 2157 (1988).
- [Boh39] N. Bohr and J. A. Wheeler, *Phys. Rev.* **56**, 426 (1939).
- [Boh75] A. Bohr and B. R. Mottelson, *Nuclear Structure* Vol. 2, (Benjamin, New York, 1975).
- [Bor89] P. F. Bortignon, R. A. Broglia, A. Bracco, W. Cassing, T. Døssing and W. E. Ormand, *Nucl. Phys. A* **495**, 155c (1989).
- [Bra89] A. Bracco, J. J. Gaardhøje, A. M. Bruce, J. D. Garrett, B. Herskind, M. Pginanelli, D. Barnéoud, H. Nifenecker, J. A. Pinston, C. Ristori, F. Schussler, J. Bacelar, and H. Hofmann, *Phys. Rev. Lett.* **62**, 2080 (1989).
- [Bri55] D. M. Brink, PhD. Thesis, Oxford Univ., unpublished, (1955).
- [Bro92] R. A. Broglia, P. F. Bortignon and A. Bracco, *Prog. Part. Nucl. Phys.* **28**, 517 (1992).
- [Bru86] R. Brun, F. Bruyant, M. Maire, A. C. McPherson, and P. Zanrini, *GEANT3 Users Guide*, Data Handling Division DD/EE/84-1, CERN 1986.
- [But90] R. Butsch, M. Thoennesen, D. R. Chakrabarty, M. G. Herman and P. Paul, *Phys. Rev. C* **41**, 1530 (1990).



- [Cha87] D. R. Chakrabarty, S. Sen, M. Thoennessen, N. Alamos, P. Paul, R. Schicker, J. Stachel, and J. J. Gaardhøje, *Phys. Rev. C* **36**, 1886 (1987).
- [Die74] F. S. Dietrich, J. C. Browne, W. J. O'Connell, M. J. Kay, *Phys. Rev. C* **10**, 795 (1974).
- [Die88] S. S. Dietrich and B. L. Berman, *At. Data Nucl. Data Tables* **38**, 199 (1988).
- [Dil73] W. Dilg, W. Schantl, H. Vonach and M. Uhl, *Nucl. Phys.* **A217**, 269 (1973).
- [Fes92] H. Feshbach, *Theoretical Nuclear Physics : Nuclear Reactions*, (J. Wiley and Sons, 1992).
- [Fra88] N. Frascaria, *Nucl. Phys. A* **482**, 245c (1988).
- [Gal85] M. Gallardo, M. Diebel, T. Døssing, and R. A. Broglia, *Nucl. Phys.* **A443**, 415 (1985).
- [Gar86] J. J. Gaardhøje, C. Ellegaard, B. Herskind, R. M. Diamond, M. A. Delaplanque, G. Dines, A. O. Macchiavelli, and F. S. Stephens, *Phys. Rev. Lett.* **56**, 1783 (1986).
- [Gar87] J. J. Gaardhøje, *et al.*, *Phys. Rev. Lett.* **59**, 1409 (1987).
- [Gar92] J. J. Gaardhøje, *Ann. Rev. Nucl. Part. Sci.* **42**, 483 (1992).
- [Gol48] M. Goldhaber and E. Teller, *Phys. Rev.* **74**, 1046 (1948).
- [Goo88] A. L. Goodman, *Phys. Rev. C* **37**, 2162 (1988).
- [Gos85] C. A. Gossett, K. A. Snover, J. A. Behr, G. Feldman, and J. L. Osborne, *Phys. Rev. Lett.* **54**, 1486 (1985).
- [Jac75] J. D. Jackson, *Classical Electrodynamics, Second Edition*, (J. Wiley and Sons, 1975).
- [Jan86] R. V. F. Janssens, R. Holzmann, W. Henning, T. L. Khoo, K. T. Lesko, G. S. F. Stephans, D. C. Radford, A. M. van den Berg, W. Kühn, and R. M. Ronningen, *Phys. Rev. Lett.* **181B**, 16 (1986).
- [Kat78] S. K. Kataria, V. S. Ramamurthy, and S. S. Kapoor, *Phys. Rev. C* **18**, 549 (1978).
- [Kic87] M. Kicińska-Habior, K. A. Snover, C. A. Gossett, J. A. Behr, G. Geldman, H. K. Glatzel, and J. H. Gundlach, *Phys. Rev.* **C36**, 612 (1987).
- [Kno89] G. F. Knoll *Radiation Detection and Measurement, Second Edition*, (J. Wiley and Sons, 1989).
- [Las82] M. Lassaut and J. van de Wiele, *Nucl. Phys.* **A386**, 29 (1982).
- [Mye77] W. D. Myers, W. J. Swiatecki, T. Kodama, L. J. El-Jaick, and E. R. Hilf, *Phys. Rev. C* **15**, 2032 (1977).

- [New81] J. O. Newton, B. Herskind, R. M. Diamond, E. L. Dines, J. E. Draper, K. H. Lindenberg, C. Schück, S. Shih, and F. S. Stephens, *Phys. Rev. Lett.* **46**, 1383 (1981).
- [Nif90] H. Nifenecker & J. A. Pinston, *Ann. Rev. of Nuc. & Part. Sci.*, V40 pp113 (1990).
- [Nov87] R. Novotny, R. Riess, R. Hingmann, H. Ströher, R. D. Fisher, G. Koch, W. Köhn, V. Metag, R. Mühlhans, U. Kneissl, W. Wilke, B. Haas, J. P. Viven, R. Beck, B. Schoch and Y. Schutz, *Nucl. Instr. and Meth. A* **262**, 340 (1987).
- [Orm90] W. E. Ormand, P. F. Bortignon, R. A. Broglia, T. Døssing and B. Lauritzen, *Phys. Rev. Lett.* **64**, 2254 (1990).
- [Orm95] W. E. Ormand, private communications.
- [Pac88] J. M. Pacheco, C. Yannouleas and R. A. Broglia, *Phys. Rev. Lett.*, **61**, 294 (1988).
- [Pau94] P. Paul and M. Thoennessen, *Ann. Rev. Nucl. Part. Sci.* **44**, 65 (1994).
- [Pul77] F. Pühlhofer, *Nucl. Phys.* **A280**, 276 (1977).
- [Rei81] W. Reisdorf, *Z. Phys. A* **300**, 227(1981).
- [Ruc86] A. Ruckelshausen *et al.*, *Phys. Rev. Lett.* **56**, 2356 (1986).
- [Sch82] K. H. Schmidt, H. Delagrange, J. P. Dufour, N. Carjan, and A. Fleury, *Z. Phys. A* **308**, 215 (1982).
- [She92] B. M. Sherrill *et al.*, *Nucl. Instrum. Meth.* **B70**, 298 (1992).
- [Shl94] S. Shlomo and D. H. Youngblood, *Nucl. Phys. A* **569**, 303c (1994).
- [Sin65] P. P. Singh, R. E. Segel, L. Meyer-Schutzmeister, S. S. Hanna, R. G. Allas, *Nucl. Phys.* **65**, 577 (1965).
- [Sme91] A. Smerzi, A. Bonasera and M. DiToro, *Phys. Rev. C* **44**, 1713 (1991).
- [Sno86] K. A. Snover, *Ann. Rev. Nucl. Part. Sci.* **36**, 545 (1986).
- [Sto85] R. G. Stokstad in *Treatise on Heavy Ion Science* Vol. 3, edited by D. A. Bromley, (Plenum, New York and London, 1985).
- [Suo94] T. Suomijärvi *et al.*, *Nucl. Phys.* **A569**, 225c (1994).
- [Ste50] H. Steinwedel and J. H. D. Jensen, *Z. Naturforschung a*, 413 (1950).
- [Str90] D. W. Stracener, D. G. Sarantites, L. G. Sobotka, J. Elson, J. T. Hood, Z. Majka, V. Abenante, A. Chbihi, and D. C. Hensley, *Nucl. Instr. and Meth. A* **294**, 485 (1990).
- [Str68] V. M. Strutinsky, *Nucl. Phys.* **A122**, 1 (1968).

- [Tho87] M. Thoennesen, D. R. Chakrabarty, M. G. Herman, R. Butsch, and P. Paul, *Phys. Rev. Lett.* **59**, 2860 (1987).
- [Tho91] M. Thoennesen, J. R. Beene, F. E. Bertrand, D. J. Horen, M. L. Halbert, D. C. Hensley, J. E. Lisantti, W. Mittig, Y. Schutz, N. Alamanos, F. Auger, J. Barrette, B. Fernandez, A. Gillibert, B. Haas, J. P. Vivien and A. M. Nathan, *Phys. Rev. C* **43**, R12 (1991).
- [Tho93] M. Thoennesen, J. R. Beene, F. E. Bertrand, C. Baktash, M. L. Halbert, D. J. Horen, D. G. Sarantities, W. Spang, and D. W. Stracener, *Phys. Rev. Lett.* **70**, 4055 (1993).
- [Tho94] M. Thoennesen, E. Ramakrishnan, J. R. Beene, F. E. Bertrand, M. L. Halbert, D. J. Horen, P. E. Mueller, and R. L. Varner, accepted for publication in *Phys. Rev. C*.
- [Tsa75] S. F. Tsai and G. F. Bertsch, *Phys. Rev. C* **11**, 1634 (1975).
- [Wer94] T. R. Werner, private communication.
- [Wil80] W. W. Wilke, J. R. Birkelund, H. J. Wollersheim, A. D. Hoover, J. R. Huizenga, W. U. Schröder, L. E. Tubbs, *Atomic and Nuclear Data Tables* **25**, 389 (1980).
- [Won90] S. S. M. Wong, *Introductory Nuclear Physics*, (Prentice Hall, 1990).
- [Wou88] A. van der Woude, *Nucl. Phys. A* **482**, 453c (1988).
- [You76] D. H. Youngblood, J. M. Moss, C. M. Rosza, J. D. Brown, *Phys. Rev. C* **13**, 994 (1976)

MICHIGAN STATE UNIV. LIBRARIES



31293014005353